Assessing an Orientation Model and Stress Tensor for Semi-Flexible Glass Fibers in Polypropylene Using a Sliding Plate Rheometer: for the Use of Simulating Processes

Kevin C. Ortman Jr.

Dissertation submitted to the faculty of

Virginia Polytechnic Institute and State University

In partial fulfillment of the requirements for the degree of

DOCTOR OF PHILOSOPHY

in

Chemical Engineering

Donald G. Baird, Chairman

Peter Wapperom

Stephen Martin

Luke Achenie

August 5, 2011

Blacksburg, Virginia

Keywords: Injection Molding, Long Fiber Orientation, Sliding Plate Rheometer

Assessing an Orientation Model and Stress Tensor for Semi-Flexible Glass Fibers in Polypropylene Using a Sliding Plate Rheometer: for the Use of Simulating Processes

Kevin C. Ortman Jr.

ABSTRACT

Great interest exists in adding long fibers into polymeric fluids due to the increase in properties associated with the composite, as compared to the neat resin. These properties, however, are dependent on the fiber orientations generated during processing, such as injection molding. In an effort to optimize industrial processing, optimize mold design, and maximize desired properties of the final part, it is highly desirable to predict long fiber orientation as a function of processing conditions.

The purpose of this research is to use rheology as a fundamental means of understanding the transient orientation behavior of concentrated long glass (> 1mm) fiber suspensions. Specifically, this research explores the method of using rheology as a means of obtaining stress tensor and orientation model parameters needed to accurately predict the transient fiber orientation of long glass fiber reinforced polypropylene, in a well-defined simple shear flow, with the hopes of extending the knowledge gained from these fundamental experiments for the use of simulating processing flows, such as injection molding. Two fiber orientation models were investigated to predict the transient orientation of the long glass fiber systems explored. One model, the Folgar-Tucker model, has been particularly useful for predicting fiber orientation in short glass fiber systems and was used in this paper to assess its performance with long glass fibers. A second orientation model, one that accounts for the semi-flexibility of fibers, was extended to describe non-dilute suspension and coupled with an augmented stress tensor that accounts for fiber bending. Stress tensor and orientation model parameters were determined (in all cases) by best fitting these coupled equations to measured stress data obtained using a sliding plate rheometer. Results showed the semi-flexible orientation model and stress tensor combination, overall, provided improved rheological results as compared to the Folgar-Tucker model when coupled with the stress tensor of Lipscomb (1988). Furthermore, it was found that both stress tensors required empirical modification to accurately fit the measured data. Both orientation models provided encouraging results when predicting the transient fiber orientation in a sliding plate rheometer, for all initial fiber orientations explored. Additionally, both orientation models provided encouraging results when the model parameters, determined from the rheological study, were used for the purpose of predicting fiber orientation in an injection molded center-gated disk.

Acknowledgments

The author wishes to express his thanks to both Professors Donald G. Baird and Peter Wapperom for their support and guidance that resulted in the completion of this work. In addition, the author would like to thank Dr. Stephen Martin and Dr. Luke Achenie for their insightful comments and suggestions during the progression of his work.

The author would also like to acknowledge the following people:

- His brother, Keith Ortman, for his support, encouragement, and admiration for as long as the author can remember.
- His father, Kevin Ortman Sr., for demonstrating and imparting an intuitive approach to problem solving and for having instilled the sense of responsibility and discipline the author possesses today.
- His mother, Diana Ortman, for her inspiration, passion, and unyielding love whose compassion and faith have molded the author into the person he is today.
- His companion and best friend, Christa Marlowe, for sharing a love, energy, and charisma that has both motivated and captivated the author since day one.
- His dear friend and brother, Christopher Karickhoff, for his years of wisdom, pickin', and, no doubt, gallons of homemade ice cream.
- His dear friends and accomplices, Eli Strah and Ibrahime Abraham, for their undying humor, satire, and contagious passion for life (especially Ibrahime's).
- His lab mates, Mike Heinzer, Chen Chen, Kevin Meyer, Syed Mazahir, John Hoffman, John Quigley, Mark Cieslinski, Geoff Widdison, and Kevin Harrington.
- His lab mate Gregorio Vélez-García for demonstrating an intuition, dedication, and an optimism that the author greatly admires.
- Professor Stephanie T. Lopina for demonstrating a passion that has truly moved and impacted the author's life.
- Professor Lois Hansen-Polcar for providing the initial spark that founded the author's passion for Chemical Engineering.

Original Contributions

The following are considered to be significant original contributions of this research:

- Experimentally linked the deformation to stress response and the associated fiber microstructure, of a concentrated long glass fiber filled suspension, at the startup of simple shear flow using a sliding plate rheometer.

- Extended an orientation model, based on semi-flexible fibers, for the purpose of exploring non-dilute long fiber suspensions by including isotropic rotary diffusion.

- Augmented suspension stress theory to account for stresses caused by semi-flexible fiber bending.

- Provided empirical modifications to the Lipscomb stress tensor that resulted in more accurate stress predictions when applied to a concentrated long glass fiber suspension.

- Experimentally assessed an orientation model, based on semi-flexibility, in its ability to predict concentrated long fiber orientation in an injection molded center-gated disk, when using model parameters determined from a rheological study.

Format of Dissertation

This dissertation is written in journal format. Chapters 3, 4, and 5 are self contained papers that are to be submitted for journal publication. Each paper separately describes the experiments, results and discussion, and conclusions relative to each chapter. With the exception of Chapter 2, the review of literature, the figures and tables are presented after the reference section of each chapter.

Attribution

Chapter 3: Transient Shear Flow Behavior of Concentrated Long Glass Fiber Suspensions in a Sliding Plate Rheometer

Dr. Baird, currently a Chemical Engineering professor at Virginia Tech, is a co-author on this paper, principal investigator, and contributed editorial comments.

Neeraj Agarwal, previously a Masters of Science student at Virginia Tech, is a co-author on this paper and initiated the research of long fiber suspensions using a sliding plate rheometer.

Dr. Wapperom, currently a Mathematics professor at Virginia Tech, is a co-author on this paper and provided editorial comments.

Chapter 4: Using Startup of Steady Shear Flow in a Sliding Plate Rheometer to Determine Material Parameters for the Purpose of Predicting Long Fiber Orientation

Dr. Baird, currently a Chemical Engineering professor at Virginia Tech, is a co-author on this paper, principal investigator, and contributed editorial comments.

Dr. Wapperom, currently a Mathematics professor at Virginia Tech, is a co-author on this paper and provided fruitful discussion that lead to the derivation of the stress terms used within this research.

Chapter 5: Predicting the Orientation of Long Glass Fibers in a Center-Gated Disk Using Model Parameters Determined From Simple Shear Rheology

Dr. Baird, currently a Chemical Engineering professor at Virginia Tech, is a co-author on this paper, principal investigator, and contributed editorial comments.

Dr. Alex Aning, currently a Material Science and Engineering professor at Virginia Tech, is a co-author on this paper, and provided expertise and equipment use for the microscopy used in this research.

Table of Contents

List of Figures

List of Tables

Chapter 1

Introduction

Chapter 1 Introduction

Polymer composites have been used for decades as a light weight, high performance material that can offer many advantages over other competitive materials[1]. For example, incorporating glass fibers into a polymer can lead to property improvements, which include increased stiffness, strength, modulus, toughness and decreased thermal expansion, thermal conductivity and electrical conductivity[2]. Of this class of fiber, long glass fibers provide superior mechanical strength and toughness as compared to their short fiber counterpart. The incorporation of long glass fibers into a polymeric matrix represents a lucrative yet complex class of composites where the properties and rheological behavior is highly dependant on the processing conditions and resulting fiber orientation within the part. To optimize industrial processing, mold design, and the desired properties of the final part, it is highly desirable to be able to predict long fiber orientation as a function of processing conditions. For this reason, it is desirable to understand the link between the deformation response of a long fiber reinforced thermoplastic and the effect it has on its underlying microstructure.

1.1 Orientation Theory

Theoretical work related to fiber modeling may be broken into two classifications: continuum based and direct simulation based models. Direct simulations[3,4,5,6] involve creating the equations of motion for a single fiber and then computationally tracking how that fiber behaves in the presence of a flow field and/or other fibers. This approach often enables very unique and complex fiber dynamics to be considered, including fiber-fiber interactions (long range and short range) and flexibility. However, the amount of computational time usually required to solve the dynamics of a meaningful population of fibers is extremely high, and thus presently provide very limited industrial significance. On the other hand, continuum based models inherently describe a population of fibers and can usually be solved much more quickly, even when complex geometries are used. Most continuum based orientation models stemmed from the work of Jeffery[7] (1922) who was able to solve the dynamics of a high aspect ratio particle subject to a flow field. This model, however, represents the very special case in which no fibers may interact. Realistically, high concentrations of fiber suspensions are used and present the situation where many fibers may interact, touch, bend, and greatly affect each other. Since then, authors[8,9,10,11] have expounded on its results and have slowly begun adding terms that enable the model to begin to account for more realistic behavior, such as isotropic rotary diffusion, anisotropic rotary diffusion, and delayed orientation kinetics. However, even these considerations do not consider flexible fibers, which are of interest within this research. In 2007, a continuum based orientation model[12] refereed to here as the Bead-Rod model, was published that considered semi-flexible fibers. Although derived for non-interacting fibers, commonly used interaction terms may be analogously added to this model. As of yet this model has not been reviewed, and is believed to present what could be the first step at understanding flexible fiber orientation in processing flows.

1.2 Stress Theory

To provide a complete description of the fiber reinforced fluid, a stress equation that accounts for fiber orientation is also needed. Some authors have looked at kinetic

theory of polymer liquids and thermodynamics[13] as a fundamental basis for describing fiber orientation and their corresponding stress contributions, but most commonly used models stem from molecular theory[14,15,16,17,18]. In the latter, the theory considers different concentration régimes[15] in which the particle motion and extra stress contributions change based on the fiber orientation and physical properties of the suspensions, such as the excluded volume of particles. The theory was originally derived for high aspect ratio rigid rods, such as liquid crystalline polymers, but we believe the theory in its original (or slightly modified) form should be explored in predicting the rheology and orientation distribution of long glass fiber suspensions.

1.3 Long Fiber Rheology

Measuring the rheology of long glass fiber suspensions is a much sought after accomplishment, but as the review of literature will show, relatively little work has been done yet to understand the rheology of long fiber suspensions. Of the work reported, issues concerning bias may exist with the rheological measurements made using conventional rheometry techniques. This is highly believed because it has been shown that conventional rheometry techniques, such as the ones used in those publications, provide biased results when measuring short glass fiber suspensions[19]. For this reason, a thrust exists to study long fiber rheology from a rheometric method that may be first confirmed with short glass fibers. Using this method, the associated fiber orientation may also be studied, and provides a unique opportunity to make meaningful contributions in this area of study.

1.4 Research Objectives

The primary goal of this research is to use rheology as method of obtaining unbiased modeling parameters, that when used to simulate complex processing flows, are able to accurately predict long fiber orientation. With regard to this goal three objectives have been formulated:

1. Characterize the transient rheology and measure the corresponding transient fiber orientation of concentrated long glass fiber reinforced polypropylene, using a sliding plate.

2. Use an orientation model that accounts for fiber flexibility (the Bead-Rod model) in combination with the use (or modified use as described below) of the Lipscomb stress tensor to determine unambiguous modeling parameters from rheology experiments, and then assess their accuracy in fitting the rheology and predicting the transient fiber orientation for the case of simple shear flow. *Note*: *We may modify the Lipscomb stress tensor empirically and/or also by adding a term that attempts to account for stresses due to fiber bending.*

3. Use the semi-flexible orientation model, with model parameters determined from rheological experiments, to simulate the filling stage of a center-gated disk, and evaluate the accuracy of the orientation predictions in this complex flow.

1.5 References

1. S.G. Advani, E.M. Sozer, Process Modeling in Composites Manufacturing, 2003.
2. R. Guo, J. Azaiez, C. Bellehumeur, Rheology of fiber filled polymer melts: Role of fiber-fiber interactions and polymer-fiber coupling. Polymer Engineering and Science 385-399, 2005.
3. L.H. Switzer III, D.J. Klingenberg, Rheology of sheared flexible fiber suspensions via fiber-level simulations, Journal of Rheology, 47(3), 759-778, 2003.
4. P. Skjetne, R. Ross, D.J. Klingenberg, Simulation of single fiber dynamics, Journal of Chemistry Physics, 107(6), 2108-2121, 1997.
5. J.D. Goddard, Y.-H. Huang, On the motion of flexible threads in a Stokes shear field. Journal of Non-Newtonian Fluid Mechanics
6. E.J. Hinch, L.G. Leal, The effect of Brownian motion on the rheological properties of a suspension of non-spherical particles. Journal of Fluid Mechanics, 52, 683-712, 1972.
7. G.B. Jeffery, The motion of ellipsoidal particles immersed in a viscous fluid. Proceedings of the Royal Society A, 102, 161-179, 1922.
8. B. Nguyen, S. Bapanapalli, J. Holbery, M. Smith, V. Kunc, B. Frame, J. Phelps, C. Tucker III, Fiber Length and Orientation in Long-Fiber Injection-Molded Thermoplastics-- Part I: Modeling of Microstructure and Elastic Properties, J. Thermoplastic Composite Materials, 42, 1003-1029, 2008.
9. J. Phelps, C. Tucker III, An anisotropic rotary diffusion model for fiber orientation in short- and long-fiber thermoplastics, Journal of Non-Newtonian Fluid Mechanics 156 165-176, 2009.
10. J. Wang, J. O'Gara, C.L. Tucker III, An objective model for slow orientation kinetics in concentrated fiber suspensions: Theory and rheological evidence. Journal of Rheology, 52(5), 1179-1200, 2008.
11. S.G. Advani, C.L. Tucker, Closure approximations for three-dimensional structure tensors. Journal of Rheology, 34(3), 367-386, 1990.
12. U. Strautins, A. Latz, Flow-driven orientation dynamics of semiflexible fiber systems. Rheologica Acta, 46 (1057-1064, 2007.
13. M. Rajabian, C. Dubois, M. Grmela, Suspensions of semiflexible fibers in polymer fluids: rheology and thermodynamics. Rehologica Acta. 44, 521-535, 2005.
14. G.K. Batchelor, The stress generated in a non-dilute suspension of elongated particles by pure straining motion. Journal of Fluid Mechanics, 46, 813-829, 1971.
15. M. Doi, S.F. Edwards, The Theory of Polymer Dynamics, Oxford University Press: New York, 1988.
16. G.G. Lipscomb, M.M. Denn, D.U. Hur, D.V.Boger, The flow of fiber suspensions in complex geometries. Journal of Non-Newtonian Fluid Mechanics, 26, 197-325, 1988.
17. M.A. Bibbo and R.C. Armstrong, "Rheology of Semi-Concentrated Fiber Suspensions in Newtonian and Non-Newtonian Fluids", Manufacturing Science of Composites, T.G. Gutowski (Ed.), ASME Publication, New York 1988.
18. S.M. Dinh, R.C. Armstrong, A rheological equation of state for semiconcentrated fiber suspensions. Journal of Rheology, 28, 207-227, 1984.
19. A.P.R. Eberle, D.G. Baird, P. Wapperom, and G.M. Vélez-García, Obtaining reliable transient rheological data on concentrated short fiber suspensions using a rotational

rheometer, Journal of Rheology, 53, 1049-1069, 2009.

Chapter 2

Review of the Literature

Chapter 2 Review of the Literature

2.1 Glass Fiber Composites

The use of glass fiber within industrial applications has many competitive advantages. Examples of such applications that routinely use glass fiber reinforced composites consist of structural, automotive, aeronautical, and many other applications [11]. Parts manufactured from glass fiber reinforced thermoplastics are often capable of having a high strength to weight ratio, high stiffness, and high flexural modulus. Furthermore, parts made from long glass fibers show enhanced properties compared to their short glass fiber counterpart. Specifically, long fiber reinforced thermoplastics have enhanced stiffness, overall strength, and creep endurance [10]. These enhanced properties are primarily due to the load-supporting network that is obtained with long fibers [10]. As with all fiber composites, however, the success of these desired properties are highly dependent on the materials used, processing conditions, and final fiber orientation. Another advantage of parts made from glass fiber composites is that they offer effective cost benefits because of the relatively low cost for glass fibers [7]. In fact, glass fiber parts offer competitive cost effectiveness when compared to metallic materials constructed for the same purposes [4]. Glass fibers are also readily adaptable into common processes such as injection molding and compression molding (or both) applications [4].

Long glass fiber reinforced resin is generally manufactured from a method known as pultrusion. In this method, spools of glass fibers (with a typical fiber diameter that ranges from 8-14 μm) are joined together and pulled through a resin bath, are quenched, and then cut to desired lengths. In many instances, the surface of these glass fibers is usually chemically treated with a coupling agent before entering the resin bath. Such coupling agents aid the adhesion between the inorganic glass and the organic resin, and usually consist of molecules containing silane groups such as methacryloxypropyltrimethoxysilane (MPS) or phenyltriethoxysilate (PTS) [19]. During the pultrusion process, many fibers are not fully "wetted," and some processes coat the fiber strands individually before reuniting them, and then quenching and cutting the strands. Strands are usually cut to form discontinuous pellets of length 0.5 cm to 12 cm, depending on the desired application. Typical pellet fiber fractions used industrially range from 10-40 wt. % [1,7]. Other processes form long strands into glass mats that are considered to be continuous. Such materials are popular with compression molding applications, due to their highly random fiber orientation and good strength in all directions of mechanical load.

2.1.1 Classification by Concentration

Two different theoretical considerations have been given within literature to help classify fiber suspensions. Specifically, fibers are usually classified by both their concentration and their length. The classical method of classifying a fiber suspension's concentration regime was given by Doi and Edwards (1988) [20]. They considered a suspension of fibers with n equal to the number fibers per unit volume, each of given length L and diameter d. The aspect ratio (a_r) of the fiber is often convenient to use and

is defined as $a_r = L/d$. Following this, the volume fraction (ϕ) of fibers in a suspension may be described as,

$$\phi = \frac{\pi n L^3}{4 a_r^2} \qquad 2.1$$

Consequently, Doi and Edwards contemplated three concentration regimes that could be described in terms of the ϕ and the a_r of the fibers. Specifically, these regimes are called the *dilute* regime, *semi-dilute* regime, and *concentrated* regime.

2.1.1(a) Dilute Regime. A fiber suspension is said to be within the dilute regime when the existence of a single fiber is not affected by the presence of any other fibers. More specifically, a single fiber within the dilute regime is never able to "see" or be affected by another fiber by any conceivable interactions, such as by fiber-fiber contacts or inter-particle hydrodynamic effects. This theoretically exists when the average distance between adjacent fibers is greater than L, and hence for a population of fibers in a specific volume, the restriction on n is $n < 1/L^3$. In terms of the aspect ratio, the restriction for ϕ *is* $\phi < \pi a_r^{-2}/4$, or more conveniently, the order of magnitude of ϕ must be $< a_r^{-2}$ to be considered dilute.

2.1.1(b) Semi-dilute Regime. In semi-dilute regime, fibers begin to feel the presence of their nearest neighbors mostly through hydrodynamic interactions, but only through very limited fiber-fiber contacts. Such interactions become possible when $n > 1/L^3$. The semi-dilute regime also has an upper limit of n that is still considered semi-dilute. This is achieved as the average distance between adjacent fibers becomes smaller, but is still $>> d$. Because the average distance between adjacent fibers is a function of the orientation state of the system, this upper limit for the semi-dilute regime has two restrictions on n, based on the cases of a perfectly random system and a perfectly aligned system of fibers. For a perfectly random system of fibers, the upper limit of the semi-dilute regime restricts $n << 1/(dL^2)$, and for a perfectly aligned system $n << 1/(d^2L)$. When this information is constructed in terms of the ϕ, the order of magnitude of $\phi << a_r^{-1}$ and $\phi << \pi/4$ results for the random and aligned systems, respectively.

2.1.1(c) Concentrated Regime. In accordance with the upper limit of the semi-dilute regime, the concentrated regime is reached when either $n \geq 1/(dL^2)$ or $\phi \geq a_r^{-1}$. In the concentrated regime, fiber-fiber interactions are highly present and individual fibers collide as they move. In highly concentrated systems, fibers will often physically cluster together, and possess a type of nematic potential to preferentially align [20]. Indeed, the concentrated fiber regime contains a wide variety of complex phenomena that are yet to be fully understood, and is inherently the most complicated of all the fiber regimes discussed.

2.1.2 Classification by Length

Fibers are also classified by their length and are said to be either "short" or "long." The term "short" refers to a fiber that is said to remain rigid and straight during processing, and has been the subject of much past research [25,28,30,58,62].

Experimentally, glass fibers are usually said to be short when their average L is < 1 mm, and are said to be long when their average L is > 1 mm [2]. If a fiber is said to be "long," then the fiber does not necessarily remain rigid and straight during flow and it may exhibit flexibility. A more useful method of describing the flexibility (or its reciprocal being stiffness) of a fiber has been proposed by Switzer and Klingenberg [16]. In their assessment, flexibility (f) is defined as,

$$f \equiv \frac{64\eta_m \dot{\gamma} a_r^4}{E_Y \pi} \qquad 2.2$$

In this equation, η_m is the matrix viscosity, $\dot{\gamma}$ is the shear rate, and E_Y is the Young's modulus of the fiber. From this expression, the flexibility of a fiber can be seen to increase with aspect ratio for a material with a given Young's modulus. For example, a fiber of L = 1 mm, d = 13 μm and E_Y = 7810 MPa, is processed at 1 s^{-1} in a matrix with viscosity of η_m = 560 Pa*s, it would have a f = 51. Although this is a rough approximation, it would thus follow that glass fibers whose flexibility is f < 51 are said to be "short" and remain rigid during processing at $\dot{\gamma}$ = 1 s^{-1}, whereas glass fibers whose f > 51 are said to be "long" and flexible. For comparison, if the same fiber was 3 mm long, it would have a f = 4143, or a value 81 times more flexible than the 1mm fiber at the same shear rate.

At this point, comments concerning the effects of Brownian motion are presented. If one compares the relative advection magnitude to the Brownian motion magnitude, this results in a Peclet number (Pe) for fibers,

$$Pe = \frac{\dot{\gamma}}{D_r} \qquad 2.3$$

where D_r is the isotropic rotational diffusivity [27]. When the order of magnitude of Pe is $\leq$ 1, Brownian motion is non-negligible, but for Pe >> 1, Brownian motion is negligible. Even for a population of short fibers, it is very common for the Pe to be sufficiently large that Brownian motion is negligible. In fact, a fiber with a L of at least 10 μm is usually considered to be non-Brownian [19]. Hence, Brownian motion does not affect long glass fibers.

Experimentally, fibers may have a population of fiber lengths and this population must be measured to determine its fiber length distribution (FLD). Once the FLD has been measured, the average fiber length is commonly calculated by taking the first and second moments of the fiber length distribution to form the number average length (L_n) and the weight average length (L_w), respectively,

$$L_n = \frac{\sum_i n_i L_i}{\sum_i n_i} \qquad 2.4$$

$$L_w = \frac{\sum_i n_i L_i^2}{\sum_i n_i L_i} \qquad 2.5$$

Then, average lengths determined from Eqs. 2.4 and 2.5 are often used to assess whether the fiber population is considered to be rigid (short) or flexible (long), in accordance with Eq. 2.2 (and the 1 mm distinction for glass fibers).

2.1.3 Fiber Orientation Analysis

As mentioned previously, fiber orientation is an important factor that impacts the quality and overall properties of a fiber reinforced part. In this sense, the phrase *fiber orientation* (or *fiber configuration*) represents the precise spatial positioning of a fiber in a 3-dimensional part. Examples of such properties affected by fiber orientation are final part stiffness, strength, impact toughness, and resistance to creep. Hence, in an effort to optimize design, there exists an incentive to link fiber microstructure to processing conditions [4,7,3]. In this subsection, a description of common ways of theoretically describing and experimentally measuring fiber orientation and configuration will be reviewed.

2.1.3(a) Short Fibers. Short fibers are considered to be rigid rods, each with an orientation that can be describe by a unit vector aligned along its backbone, Fig. 2.1.

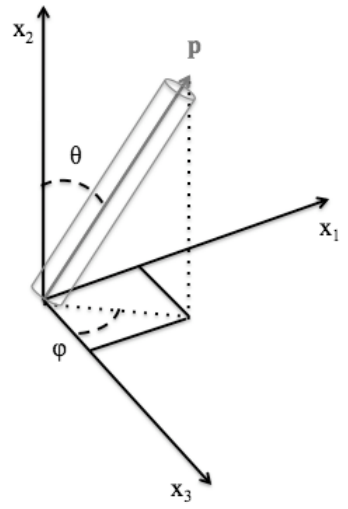

Figure 2.1: Rigid fiber with orientation vector **p** in a general coordinate system.

This unit vector **p** in Fig. 2.1 is the orientation vector associated with the rigid fiber, and contains all information desired about the orientation of this fiber. For a population of fibers, it is convenient to describe the orientation vectors in terms of an orientation tensor **A**,

$$\mathbf{A} = \int_0^{2\pi}\int_0^{\pi} \mathbf{pp}\ \psi(\mathbf{p},t)\,d\theta\,d\varphi = \int \mathbf{pp}\ \psi(\mathbf{p},t)\,d\mathbf{p} \qquad 2.6$$

where **A** is the second moment of the orientation distribution function ψ, and θ and φ are the spherical coordinate angles of orientation space. The orientation tensor of a purely random system would be one represented by **A** whose trace components are all equal to 1/3. Furthermore, for a fully aligned system, say in the x_1 direction of Fig. 2.1, the A_{11} component of **A** is equal to 1, and 0 for all other components. The sum of the trace components of **A** is always equal to 1. Experimentally, the orientation tensor may be measured by examining a cross-section of a desired sample and analyzing the resulting ellipses that become visible, as described by Hine et al. [21]. More specifically, the geometric ratio of an ellipses' major to minor axes and the degree of tilt of an ellipse may be used determine the orientation tensor components of each fiber. These values are then averaged over the population of fibers to construct the orientation tensor **A**. The reader is referred to the literature for more details [21].

2.1.3(b) Long Fibers. Long fibers present an inherent difficulty in both theoretically describing and measuring their configuration. Until now, the terms *orientation* and *configuration* have been used fairly interchangeably to refer to the spatial positioning of fibers. It is more appropriate, however, to speak of *configuration* when referring to long fibers, because long fibers by definition may exhibit flexibility and are not sufficiently described by a single orientation vector. This flexibility allows the long fiber to possess contours throughout space, as opposed to a straight rigid fiber. Such an example of this may be visualized in Fig. 2.2.

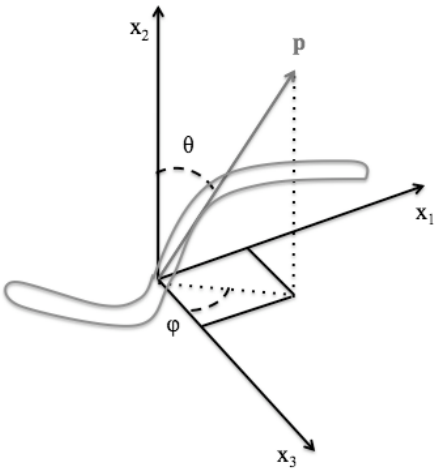

Figure 2.2: Flexible fiber with an arbitrary configuration. As can be seen, a single orientation vector **p** is not sufficient to describe the spatial positioning of the long fiber.

Currently, there is no agreed upon way of describing the configuration of a population of long fibers, either theoretically or experimentally, and is a subject of much debate. Some authors have experimentally analyzed long fibers using the identical method used for short fibers, but the orientation measured is usually redefined to describe only the *tangential* orientation of the population of long fibers [22,23]. Other authors have chosen a much more mechanical method of characterizing long fiber configuration, by analyzing cross-sections at very small incremental depths, and recreating the 3-dimensional structure by systematically connecting the analyzed data at the varying depths. A radically different method, which has been increasingly gaining popularity, involves the

use of high-resolution X-ray tomography. X-ray's are used to penetrate the sample at various angles and depths to reveal the glass fibers within the thermoplastic material. These X-ray images are then reassembled digitally to construct a 3-dimensional model of the sample's fibers. A method of mathematically representing long fiber orientation (configuration) is also not yet agreed on, and presents difficulty when trying to use experimental measurements to evaluate the accuracy of fiber orientation models. As a note, some authors have chosen to use an end-to-end vector to concisely represent information about the fiber's configuration [15].

2.2 Rheology of Long Fiber Suspensions

2.2.1 Background

The importance of understanding the rheology of fiber composite behavior has been well expressed in literature [25]. In this sense, rheology may be used as a tool to understand fiber dynamics and suspension response to deformation, and to ultimately apply its findings to industrial processes. The use of rheology is of particular interest because it provides an unbiased method of measuring suspension properties and determining unique material parameters (independent of processing conditions). Additionally, rheology experiments may be used to track fiber orientation and aid in providing a link between orientation and suspension stress. Conversely, it also provides a method of testing the validity of orientation and stress models in rheological flow fields. Although many advantages come from understanding the rheology of fiber filled composites, several challenges exist within the realm of conventional rheometry, and must first be overcome in order to obtain accurate and reliable measurements. The following describes the advantages and disadvantages of commonly encountered rheometers used in the field of long fiber rheology.

2.2.1(a) Rotational Rheometers. Rotational rheometers are often used to study various polymeric melts, including those made from fiber composites. The benefits of such rheometers exist in their ability to use different geometries (the most common being parallel-disk and cone-and-plate). Additionally, rotational rheometers are able to explore virtually limitless strain values, because the sample may physically rotate indefinitely. Adversely, rotational rheometers can be very sensitive to fiber length due to wall effects. With regards to this, authors usually recommend a minimal sample thickness above which the gap distance does not affect the transient rheology. In accordance with this, it is usually suggested that the gap-to-fiber length be at least 2-3:1, or at least a gap-to-fiber diameter of 80-100, in order limit these undesirable interactions of the fibers with the rheometer walls [4,26,27,28,29]. Overcoming this restriction may be plausible for parallel-disk samples, but the inhomogeneous shear field has been shown to disrupt fiber orientation [30]. If a cone-and-plate geometry is used, the center portion of the sample may be greatly less than the gap-to-fiber length ratio criteria, and cause significant wall interactions. To avoid this, Eberle et al. has recently suggested that the center of the cone-and-plate samples be removed to form cone-and-disk samples [19]. Additionally, loading cone-and-plate samples by squeezing to a desired gap may contribute to fiber packing [1], and is usually undesired. However, even in the case of these rheometric geometries, long fibers often cannot be used because fibers of sufficient length do not always follow the fluid streamlines and cause the suspension to migrate out of the

sample, causing unreliable results. Additionally, edge phenomena must also be controlled. Specifically, thermal-oxidative degradation occurs at the sample's border with the atmosphere, and may effect measurements [1]. Flow instabilities have also been reported with rotational rheometers at high shear rates ($> 10\ s^{-1}$) [1]. Lastly, conventional rotational rheometers often cannot even supply the required force needed to rotate highly concentrated long glass fiber samples and measure their rheology. Rotational rheometers possess many limitations in their ability to study such fiber systems.

2.2.1(b) Capillary Rheometers. Capillary rheometers have been used to study fiber melt viscosity, especially at high shear rates. Using this device, the pressure drop of the melt is measured by pushing the suspension melt through a capillary, and is used to determine the suspension viscosity. Using this technique melt viscosities may be determined for both long and short fibers. One of the biggest disadvantages of this method remains in the large fiber breakage that occurs. Long fibers are greatly reduced in length due to the high shear rates and breakage in the capillary contraction; hence fiber length effects are difficult to study. Additionally, this method involves inhomogeneous shear, and may contribute to fiber migration [31]. Also, transient fiber orientation is difficult (if not impossible) to study using this method.

2.2.1(c) Rectilinear Rheometers. Rectilinear rheometers consist of devices that deform the material in a rectilinear fashion. An important example of these rheometers is the sliding plate. Sliding plate rheometers work by subjecting a sample to a simple shear flow in which one plate moves and the other plate stays stationary. This method offers many advantages. First, a sample may be virtually of any thickness (provided the rheometer is designed to accommodate it), the fluid streamlines are linear and do not facilitate suspension escape, the shear field is homogeneous, the rheometer is able to provide large stresses (compared to rotational rheometers) to study highly concentrated long fibers, easily allows for samples to be prepared with varying initial fiber orientation, and can be used to study transient fiber orientation. Additionally, the sliding plate has been reported as being able to help prevent unreliable measurements due to thermal-oxidative degradation due to its localized area of measurement in the center of the sample [1]. Theoretically, the sliding plate can also be used to study oscillatory shear flow [1]. One of the biggest disadvantages of the sliding plate is that it is limited in the amount of strain that can be explored in a single experiment.

2.2.1(d) Squeeze Rheometry. Squeeze flow rheometry provides a method of studying the transient rheology of a wide range of materials, ranging from asphalts to thermoplastics (ie. reinforced with long fibers) [12]. Squeeze flow rheometry is usually conducted under constant rheometer area, or constant sample volume. In the first case, an area of plates is constantly "wetted" with sample, but the sample is able to squeeze out of the rheometer as the plates move together. Under constant sample volume, the sample is placed between the plates and is squeezed. In this case, however, the sample is not squeezed sufficiently far that the melt exits out of the rheometer, and hence the total volume of the sample remains constant. This may be done in a lubricated sense, where biaxial or unidirectional extension may be studied. Of course, difficulty may exist in sufficiently lubricating the sample to eliminate shear between the squeezing plates. Conversely, non-lubricated plates may be used to study the squeezing response of a fiber

melt. Such a process may be of great industrial importance, but this type of flow is complex and possesses varying velocity gradients [12]. This can create obvious difficulties in determining reliable rheological results.

2.2.2 Steady Shear Flow

Concerning rheometric flows, steady shear flow is a simple flow in which the fluid velocity is unidirectional ($v_1 = \dot{\gamma}\, x_2$, $v_2 = v_3 = 0$) and the shear rate is assumed uniform through the rheometer gap. The shear viscosity η of a fluid is defined in terms of the measured shear stress component of the total stress tensor ($\boldsymbol{\sigma}$) in the following manner,

$$\eta = \sigma_{12} / \dot{\gamma} \tag{2. 7}$$

Additionally, the first and secondary normal stress difference functions N_1 and N_2, respectively, are defined as

$$N_1 = \sigma_{11} - \sigma_{22} \tag{2. 8}$$

$$N_2 = \sigma_{22} - \sigma_{33} \tag{2. 9}$$

In this section, a literature discussion of these rheological material functions will be discussed for long fiber reinforced fluids.

2.2.2(a) Shear Viscosity. In general, the viscosity of a polymeric fluid increases with the addition of fibers, but the precise manner in which this occurs depends on properties belonging to both the matrix and the fibers. The effects of fiber concentration on the shear viscosity will first be discussed, followed by shear rate behavior, fiber aspect ratio effects, and finally fiber flexibility.

Increased fiber loadings increase melt viscosities [4,32,33,34,7]. Fiber concentration is usually described in terms of weight percent fiber or volume percent fiber. Becraft and Metzner (1992) [32] studied concentrated E-glass (~ 1.0 mm) in polypropylene and polyethylene matrices at different concentrations and aspect ratios over a range of shear rates using both a parallel-disk rheometer and a capillary rheometer. They found shear viscosity always increased as fiber weight percent increased, but noticed this increase was more prominent at lower shear rates, and at high shear rates only small viscosity increase existed. However, fiber breakage was reported to be significant at the higher shear rates. This viscosity behavior has also been reported for short fiber systems [33,34,7].

Significant shear thinning behavior has been reported for fiber suspensions, especially at high fiber concentration, as shear rate is increased [32,4]. For example, Becraft and Metzner [32] found that for high concentration samples (ϕ_w ~ 40 wt. %, where ϕ_w is the weight fraction of fiber in the suspension) the Newtonian plateau of the viscosity versus shear rate plot (at low shear rates) disappeared [32]. For long fibers, being able to exhibit flexibility, an explanation for such behavior has been suggested [4,35,36]. Long fibers are able to bend and create elastic interlocking [35,36] mechanisms that cause the fibers to form networks or "flocs." Flocculation is known to

exist due to cohesive forces imparted by fibers through inter-fiber friction and contact normal forces [5]. Pronounced shear thinning usually occurs in long fiber systems because flocculation forces are usually strong compared to shear stresses at low shear rates [4]. As shear rates are increased (and consequently shear stresses are increased), it becomes easier to break up flocculated fiber networks and thus lead to a reduced steady viscosity (shear thinning) [4]. At high shear rates, such as those accomplished in a capillary rheometer, the composite viscosity has been reported to approach the matrix viscosity [2].

In another study Ericsson et al. [1] explored the effects of fiber concentration and shear rate. In their study of concentrated polypropylene glass mats, they found at low shear rates an increase in viscosity of 2-3 orders of magnitude over that of the neat matrix was not uncommon. At high shear rates ($> 10\ s^{-1}$), an increase of only one order of magnitude was found. They reported that the power-law region shifted to lower shear rates at higher fiber loadings. With this information, they proposed that at low shear rates Coulombic interactions dominated, while at highs shear rates hydrodynamic forces dominated. Consequently, they surmised using theory of Toll and Manson (1995) [37], that at low shear rates the viscosity should go as $\eta \sim \phi^5$, while at high shear rates $\eta \sim \phi^2$. Experiments conducted by Ericsson [1], confirm their hypothesis to be plausible.

Fiber aspect ratio and fiber flexibility are also important subjects of research. Of particular importance in the literature is the work of Keshtkar et al. [4], who studied the effects of fiber aspect ratio and flexibility for long fiber suspensions. In this study, fibers of two different aspect ratios and 3 different moduli were explored within both the semi-dilute and semi-concentrated regimes. Different moduli were chosen in their experiments to vary the effective flexibility of the fiber, as opposed to greatly varying a_r, see Eq. 2.2. In their experiments, a parallel-disk rheometer was used to determine the steady viscosity of these suspensions. In general, they found the shear-thinning behavior of fiber suspensions increased with both aspect ratio and/or flexibility. Ganani and Powell [34], reported similar behavior for short fiber (with aspect ratio). In particular, Keshtkar et al. [4] found that suspensions consisting of flexible fibers had enhanced viscosity measurements when aspect ratio was increased, especially at low shear rates and increased concentration. At high shear rates ($\sim 10\ s^{-1}$) viscosity became independent of aspect ratio in the semi-concentrated regime. They attributed this behavior to the additional fiber-fiber contacts that are naturally more prevalent at higher fiber concentrations and also proposed flocculation at low shear rates to dominate, as explained by Chaouch and Koch (2001) who suggested fibers have the ability to network by adhesive contact forces [38]. Less significant increase in the effects of aspect ratio have also been reported in the literature by both Gibson and Thomasset [40,2], who have found only modest increases in viscosity with increased aspect ratio, especially at higher shear rates. Again, however, fiber breakage could not be neglected in the experiments of Thomasset [2].

Indeed, in all concentration regimes studied, increases in viscosity resulted from increased fiber flexibility, especially at high aspect ratio [4,39]. Again, flexibility enables stronger fiber-fiber networks to form [4], especially at low shear rates. Joung et al. [14], also found flexibility to enhance viscosity predictions by at least 7-10% while conducting their numerical simulations of semi-flexible fibers in the semi-dilute regime. Some other simulation efforts of long fiber rheology, however, have predicted reductions in viscosity

with increased flexibility [5]. In this particular numerical experiment, direct simulations were conducted that focused on fiber shape, flexibility, and friction forces. Flocculation was also simulated and was said to increase viscosity, but was not found on systems that were sufficiently stiff [5]. Shear thinning was also reported to be more significant with increased flexibility and may be due to a competition between hydrodynamic forces that deform the fibers, and fiber elasticity, which tries to retain their equilibrium shape [5]. As an aside, relatively large changes in rheological properties have been predicted by relatively small changes in fiber equilibrium shape [4].

2.2.2(b) Normal Forces. Values of N_1 have been found to be much greater than the values of N_2, and are more commonly reported in the literature [4,27,29]. In long fiber suspensions, N_1 has been reported to increase with volume fraction over all concentration regimes [4]. In the semi-dilute fiber regime, the dimensionless normal stress difference function ($N_1/\eta\dot{\gamma}$) was found to be linear with shear rate. Additionally, this term was found to be nearly independent of fiber stiffness at low aspect ratio, but increased with flexibility at high aspect ratio and is more pronounced at lower shear rates [4].

2.2.3 Small Amplitude Oscillatory Shear Flow

Linear viscoelastic properties of long fiber filled materials will now be discussed. Such experiments are concerned with material responses to sinusoidal deformations, usually at low strains. The complex viscosity η^* and complex G^* modulus are defined as,

$$\eta^*(\omega) = \eta' - i\eta'' \qquad 2.10$$

$$G^*(\omega) = G' - iG'' \qquad 2.11$$

respectively.

2.2.3(a) Complex Viscosity. Regarding oscillatory flow, the applicability of the Cox-Merz Rule to fiber suspensions has been studied by Guo et al. [7]. In general, it was found that deviations between the complex viscosity at a given frequency and the shear viscosity at the corresponding shear rate differed. Particularly, it was found that the complex viscosity was consistently lower than the shear viscosity at low shear rates. Additionally, complex viscosity measurements were found to be larger at larger shear rates. Deviations between the two measurements of viscosity were determined to be most affected by changes in volume fraction rather than aspect ratio.

Complex viscosity is usually seen to increase with aspect ratio and fiber flexibility. Keshtkar et al. [4] explored linear viscoelastic properties of pre-sheared long glass samples. These samples were pre-sheared at a low and high shear rates, for comparison. For the low rate pre-sheared samples, the complex viscosity increased with fiber flexibility, but was found to be larger than the high rate pre-sheared samples. This was attributed to network like structures (flocs) that could exist at the low shear rates and stronger networks that exist with increased flexibility [4]. High rate pre-sheared samples were not dependent on fiber stiffness, but were dependent only on aspect ratio. Increased aspect ratio was found to increase the complex viscosity, especially at low frequencies. Kotsilkova (1992) [41] also found complex viscosity to be sensitive to aspect ratio, when

measuring dynamic rheological properties of glass fibers and beads in silicone oil. In this study, materials made with glass fibers showed enhanced dynamic properties over all frequencies, compared to those made with glass beads (whose aspect ratio were much less). Pre-shearing these samples resulted in decreased complex viscosity measurements. Contrary to these findings, Ericsson et al. [1] found little or no dependency of the viscosity on aspect ratio. In a similar fashion, Kitano [44,53] found aspect ratio dependency at low frequencies, but not at high rates.

Complex viscosity was also found to be dependent on shear rate and fiber volume fraction. In particular, the complex viscosity was found to shear thin with increased frequency, much like pure liquids, and may even possess the same power law exponent as the suspending medium [42,43]. The power law region was also reported to shift towards lower shear rates, due to higher local deformation [34,43,44]. Additionally, at higher shear rates (~10 s^{-1}) the complex viscosity began to approach a Newtonian plateau [2,4,27]. As volume fraction is increased, the complex viscosity increases as well [4]. In the case of samples pre-sheared to steady state, Mobuchon (2005) [25] notes that fibers in a Newtonian matrix show little or no change with increased frequency, and thus one is lead to conjecture that viscoelastic properties are really those of the matrix themselves.

2.2.3(b) Dynamic Moduli. The storage and loss moduli have also been explored in literature [7,4]. Increased fiber flexibility, or likewise decreased stiffness, has been shown to increase the storage modulus *G'* [4] in semi-dilute concentrations. Increases in *G'* have also been found to be due to aspect ratio, especially at low frequencies [7,4]. For semi-concentrated suspensions, *G'* increased with aspect ratio, but was found to be independent of fiber stiffness [4,41]. This was suggested to be an artifact of entangled fibers at increased aspect ratio. Likewise, others have showed both *G'* and *G"* increased with aspect ratio [2,19,27].

2.2.4 Transient Shear Flow

Very few authors have experimentally explored the transient shear rheology of long fiber systems. In this section, values of the transient viscosity and normal stress difference functions at the startup of shear flow will first be discussed, followed by flow reversal experiments.

2.2.4(a) Transient Shear Viscosity. In experiments conducted with long fibers, large transient overshoots were often reported [4]. Such experiments were conducted by Keshtkar [4], wherein samples were prepared by squeezing and trimming fiber samples between parallel-disk fixtures. Large error was reported due to this process [4]. Viscosity overshoot magnitude was reported to increase with fiber aspect ratio, but was not found in experiments by Bibbo and Armstrong [4,56,57]. Additionally, for low aspect ratio fiber, variable stiffness was not seen to influence viscosity peak magnitude or the strain at which steady state is reached [4]. With high aspect ratio, on the other hand, decreased stiffness increases the magnitude of the peak viscosity, and steady state is not reached until larger strain values [4]. The authors stated this might indicate that fiber orientation (ie. in the flow direction) becomes less important as fiber flexibility increases [4]. This delay in reaching steady state was also seen with increased fiber loading. Such findings are in agreement with simulations of Rajabian [27], which showed overshoot magnitude and time to reach steady state to increase with increased flexibility. Upon

cessation and startup of flow again (ie. after a time delay), stresses quickly reached the same value as obtained before cessation and suggested fibers did not undergo randomization in absence of flow [4,58].

Qualitative behavior of fiber flexibility was first explored by Arlov (1958) [59] who classified the mechanical motions of fibers as being combinations of flexible spins, flexible spin-rotations, springy rotations, snake turns, or S-turns. Flexibility has been reported to cause considerable enhancement of both the viscosity overshoot magnitude and width, especially at high aspect ratio, and may also affect the degree of final non-straight equilibrium shape [4]. This behavior was much more significant in the semi-concentrated regimes as compared to the semi-dilute regime, especially at low shear rates [4,5,14]. Likewise, Kitano [44,45] found viscosity measurements with fibers of increased flexibility to be more sensitive to volume fraction, as opposed to fibers of lower flexibility. The literature of Goto [39] too reports properties to be strongly affected by flexibility. However, it was reported that viscosity measurements decreased with increased fiber flexibility [39], contrary to findings of Keshtkar [4], but skepticism regarding the interpretation of this exists because fibers of equal length were not used [4]. Similarly, direct simulations of Switzer and Klingenberg [5] found viscosity to decrease with flexibility, contrary to Keshtkar [4]. Simulations of Rajabian [45], on the other hand, agreed with experiments discussed by Keshktar and suggest that viscosity increases with increased flexibility, but have a larger effect at increased volume fraction and aspect ratio. Also with increased flexibility, an increase in flocculation has been reported [4,35,36,54]. Strength of the floc is said to increase due to fiber flexibility causing more fiber-fiber contacts.

2.2.4(b) Transient Normal Stresses. Again, transient normal stress differences exist when fibers undergo hydrodynamic and Coulombic solid-body interactions, and are significantly affected by the addition of fibers within all concentration regimes [4,27]. Keshtkar [4] found N_1 values to increase with increased flexibility, and in general, were in good agreement with simulations of Petrich [27]. In the semi-dilute range, a rather low sensitivity of $N_1/\eta\dot{\gamma}$ was found with shear rate, and appeared linear with shear rate [4], in agreement with theoretical considerations of Carter (1967) [55]. In the semi-concentrated regime, $N_1/\eta\dot{\gamma}$ is no longer linear with shear rate and increases drastically with fiber aspect ratio [4], and is in agreement with findings of Sundararajakumar and Koch (1997) [17]. For low aspect ratio fibers, the transient measurements of $N_1/\eta\dot{\gamma}$ were found to be independent of the fiber Young's modulus and increased with fiber flexibility, especially at high aspect ratio [4]. Flexibility enhanced the magnitude of the transient N_1 measurements, and these effects were more pronounced at low shear rates. This fact further suggests that fiber-fiber interactions are very important to understanding the rheology of concentrated fiber suspensions [4,45]. The simulations of Rajabian et al. (2005) [45], which were based heavily in thermodynamic considerations, also found transient N_1 values to increase with flexibility, especially at larger aspect ratio and fiber volume fraction. Keshtkar found N_1 values measured with low aspect ratio fibers reach a plateau and then a large overshoot [4]. This value was found to be independent of fiber stiffness. For large aspect ratio fibers, no plateau exists and instead have a large broad overshoot before reaching steady state. A positive N_1 can often still be measured even

after the shear viscosity has reach steady state, indicating that not all fibers are fully oriented [4]. Increased fiber flexibility increases both the width and magnitude of the N_1 overshoot.

2.2.4(c) Flow Reversal. Flow reversal experiments have been accomplished as well for long fiber suspensions [4]. In general, the transient behavior of the viscosity under flow reversal, plateaus followed by a large delayed overshoot. As flexibility and or aspect ratio increases, the first transition plateau ends sooner and the overshoot begins sooner. This was surmised to be an artifact of the fibers tilting in the reverse direction to form a new structure, thus producing the measured stresses [4,28,29]. Tilting of the fibers occurs at lower deformations for flexible systems [4].

N_1 values have also been measured under flow reversal. During flow reversal, negative N_1 values have been reported for short fiber suspensions and also for long fiber suspensions [28,29,46,47]. N_1 values of materials containing fibers are directly proportional to the shear rate, unlike polymer solutions where they are proportional to the square of the shear rate ($N_1 \sim \dot{\gamma}^2$), with the assumption that all orientation moments are not dependent on shear rate [27]. This is suspected to be the cause of the negative undershoots. Undershoot magnitude increases with fiber flexibility. Interestingly, after the transient N_1 undershoot is passed, the value of the N_1 consistently approaches the steady state measurement obtained before flow reversal. This was also observed for short glass fiber reinforced polybutene [29].

2.2.5 Extensional Rheology

Extensional behavior is often encountered in industrial processes, such as compression molding and drawing processes. Hence, the extensional rheology of long fiber systems is also of significance. Such experiments are commonly achieved by squeeze flow experiments or uniaxial elongation tests. In this section the extensional rheology for long fiber reinforced materials are discussed.

$$\eta_1(t) = \frac{\sigma_{11} - \sigma_{33}}{2(2+m)\dot{\varepsilon}}; \quad \eta_2(t) = \frac{\sigma_{22} - \sigma_{33}}{2(1+2m)\dot{\varepsilon}} \qquad 2.12$$

In Eq. 2.12, two general extensional viscosities exist, wherein any extensional flow may be obtained by varying m from -0.5 to 1, and $\dot{\varepsilon}$ is the elongational rate of strain. For the special case of uniaxial extension, m = 0.5 and $\eta_1 = \eta_E$ and is referred to as the elongational viscosity.

A much less formal approach to understanding the effects of long fiber properties on the extensional rheology of fiber reinforced materials exists in the literature. In general, η_E is seen to increase considerably with increased fiber loadings, fiber length, and aspect ratio [2,3,11]. This is consistent with elongational experiments of Kamal (1984) [48] who looked at elongational behavior of short glass polypropylene. The Trouton ratio, defined as the elongational viscosity divided by the shear viscosity ($Tr = \eta_E/\eta$), is found to be much greater than the expected value of 3 for Newtonian fluids [2,11]. Controlled uniaxial strain experiments were done by Creasy and Advani [3]. In their experiments, a uniaxial elongational viscometer was used to explore the η_E of highly

aligned 60% fiber volume fraction long graphite fiber in a polyether-ketone-ketone (PEKK) suspension. They found the η_E to decrease with increasing strain rate. Additionally, they reported that the presence of the fibers prevents strain hardening from occurring, for which strain hardening occurs within the neat PEKK polymer. In other experiments, conducted by Mewis and Metzner (1974) [50], the η_E of the long fiber reinforced materials was reported to be independent of strain rate, but showed much enhancement over the neat matrix viscosity. Strain thinning has also been reported in uniaxial extension [11,51]. This occurs when η_E decrease with increased strain rate. Strain thinning becomes more prevalent with increased volume fraction and aspect ratio [11]. This effect is often attributed to relative shear rates between local fibers [3,11]. In fact, it is sometimes believed that the η_E of concentrated fiber composites is predominately a measure of the shear response of the melt [3,11,13]. For example, in the uniaxial extensional experiments of Creasy and Advani [3], they estimated the effective shear rate magnification of their extensional rate to be a factor of 23,000 using the theory of Batchelor [52]. Thus, they concluded that the extensional properties of concentrated fiber composites were dominated by their shear response [3].

Very little work involving the squeeze flow of fiber suspensions has been published [12,13]. Of those that exist, very little have been concerned with obtaining rheological data. In one experiment, Shuler and Advani [13] used squeeze flow to explore the effect of fiber volume fraction on the shear viscosity of carbon fibers in a PEEK suspension [90]. Viscosity was found to increase with increased volume fraction [13]. To our knowledge, no other types of extensional flows were explored concerning long fiber suspensions.

2.2.6 Yield Stress

Some debate exists concerning the existence of yield stress behavior in fiber composites. A yield stress is a shear stress that must be first overcome before the suspension can flow. In the case of long fiber suspensions, this has been suggested to be the force required to overcome fiber frictional contact forces (at rest) before the suspension can flow [5, 53]. Bennington [9] studied yield stresses in fiber suspensions, and suggested that the yield stress of a fluid scales with the volume fraction of the suspension in the following manner,

$$\sigma_0 = \alpha\phi^{\beta} \qquad 2.13$$

where σ_0 is the yield stress, and α and β are fit parameters. According to Bennington [9], values for β are typically between 2.5-3.5. Simulations of Switzer and Klingenberg [5] corroborate this model and its consistency with simple fiber network theory of Meyer and Wahren [54], but reported differing values for α compared to Bennington [9], and suggest that different fiber shapes and frictional values could be the cause of this. Yield stress magnitude has also been found to be very dependent on fiber properties, such as elastic modulus and aspect ratio [9,5]. Creasy and Advani [3], and Servais [6] too found evidence of yield like behavior in their long fiber systems, but authors such as Ericsson [1] and Guo [7] could not conclusively report the existence of a yield stress.

2.2.7 Summary of Rheology

In summary, only a limited number attempts have been made to understand the rheology of long (flexible) fiber composites. Among the few that exist in the literature, questions must be asked about those that used rheometers with known disadvantages. Such rheometers with known disadvantages are rotational rheometers with inhomogeneous shear fields (ie. parallel-disk rheometers), and rheometers that may significantly break fibers during measurements (ie. capillary rheometers) [19,39]. Nevertheless, it is apparent that fiber concentration, shear rate, fiber flexibility, and fiber orientation have pronounced effects on suspension rheology. Increased fiber concentration, and in most cases increased fiber flexibility, was seen to increase the magnitudes of η, N_1, η^*, and G'. Additionally, shear thinning was seen to increase with fiber flexibility, especially at low shear rates, and has been postulated to provide evidence of fiber flocculation in both steady state and dynamic oscillatory experiments. Lastly, transient flow and flow reversal experiments have been done using a parallel-disk rheometer and showed the transient η and N_1 functions to be dependent on fiber properties and its orientation. Despite these efforts, very little has been accomplished to provide a link between the rheology of long fiber reinforced plastics and its underlying fiber microstructure. A research effort that systematically tries to provide this link is greatly desired.

2.3 Orientation and Stress Equations

2.3.1 Continuum Simulations

The search for a correct and accurate mathematical description of fiber filled suspensions has and continues to be a much sought after accomplishment. Composite modeling often consists of two linked, however, often separated dynamics. First, modeling of the transient fiber orientation is of importance due to the effect that final composite microstructure has on its resulting properties. Second, linking this fiber orientation/configuration to the suspension's stress is often of equal importance because the two phenomena are coupled. In this section, a review of continuum based orientation and stress models used within the literature will be given. Finally, a review of direct simulations will be given, and their theoretical importance highlighted.

2.3.1(a) Orientation Models. Continuum based models inherently have many advantages. By far, the greatest advantage continuum models have over direct simulation models remain in their computational efficiency. Continuum models describe everything known about fiber suspensions in a statistical manner, and in practice allow much more complex geometries and fluid flows to be investigated, as compared to direct simulation methods. Consequently, such models usually require a very sound understanding of fiber dynamics, which few will agree actually exists in the literature, and thus may possess what seems to be a disadvantage. In this section, commonly used orientation models will be discussed, followed by stress models that are usually used in combination with them during complex simulations.

Jeffery [89] derived an expression for an ellipsoid particle in a flow field and described its motion with time. He found that such particles never fully oriented with the

flow, but often exhibited periodic orbit like dynamics now called Jeffery orbits. In a continuum sense, Jeffery's model is,

$$\frac{D\mathbf{A}}{Dt} = \mathbf{W}\cdot\mathbf{A} - \mathbf{A}\cdot\mathbf{W} + \xi(\mathbf{D}\cdot\mathbf{A} + \mathbf{A}\cdot\mathbf{D} - 2\mathbf{D}:\mathbf{A}_4) \qquad 2.14$$

wherein **A** is the orientation tensor as defined in Section 2.1.3, $\mathbf{W} = [(\nabla \mathrm{v})^t - \nabla \mathrm{v}]/2$ is the vorticity tensor, $\mathbf{D} = [(\nabla \mathrm{v})^t + \nabla \mathrm{v}]/2$ is the rate of strain tensor, and ξ is a shape factor defined in terms of the particles aspect ratio as $\xi = (a_r^2 - 1)/(a_r^2 + 1)$. In this context, the velocity gradient is defined as $\nabla v = \partial \mathrm{v_j}/\partial \mathrm{x_i}$. The fourth order orientation tensor is defined as the fourth moment of the orientation distribution function, Eq. 2.15.

$$\mathbf{A}_4(t) = \int \mathbf{pppp}\,\psi(\mathbf{p},t)\,d\mathbf{p} \qquad 2.15$$

$\mathbf{A_4}$ is almost always requires a closure approximation to decouple this fourth order tensor in terms of the second order orientation tensor **A**. Common forms of this closure approximation are expressed through linear, quadratic, hybrid, and higher order polynomial closures such as the invariant-based orthotropic fitted (IBOF) approximation [20,60,61]. A review of closure relationships has been reported in the previously referenced literature and will not be reproduced here. It was also realized that as the aspect ratio of the ellipsoid became larger, the period of orbital dynamics became much longer. If the aspect ratio was forced to be infinitely large, as has been used to approximate the aspect ratio of long fibers, ξ approached unity and the period of rotation became infinite and allowed this particle to, within all practical purposes, fully orient with the flow field. In retrospect, it can be seen that Jeffery's model provides a way of describing the motion of a rigid, mass-less, fiber in an infinitely dilute suspension. All dynamics are simply hydrodynamic, and in no way begin to even fathom effects due to inter-particle distances or contacts. However, this model provided a starting point for exploring more complex dynamics.

One of the most popular applications of Jeffery's model has been achieved through the work of Folgar and Tucker [62]. Folgar and Tucker [62] hypothesized that in non-dilute suspensions, that fiber interactions might be captured by an isotropic rotary diffusion term, as seen as an addition to Jeffery's model,

$$\frac{D\mathbf{A}}{Dt} = \mathbf{W}\cdot\mathbf{A} - \mathbf{A}\cdot\mathbf{W} + \xi(\mathbf{D}\cdot\mathbf{A} + \mathbf{A}\cdot\mathbf{D} - 2\mathbf{D}:\mathbf{A}_4) + 2C_I\,\dot{\gamma}\left(\mathbf{I} - 3\mathbf{A}\right) \qquad 2.16$$

wherein C_I is the rotary diffusion coefficient and **I** is the identity tensor. Much work has gone into analytically and experimentally determining values of the rotary diffusion coefficient, but this model in many cases over predicts the rate of fiber orientation and, in general, was said to describe the orientation of short fibers only qualitatively well [63,65,58].

In a later paper, Phelps and Tucker [62] presented a model that was suggested to more accurately capture orientation dynamics of both short and long fibers. The first modification to be made to Eq. 2.16 was intended to incorporate a method that allowed for the slowing of the orientation dynamics. Such efforts have been attempted in the past

[28,19]. In this case, a so-called "slip" coefficient can be multiplied by the right hand side of Eq. 2.16 to form,

$$\frac{D\mathbf{A}}{Dt} = \alpha\left(\mathbf{W}\cdot\mathbf{A} - \mathbf{A}\cdot\mathbf{W} + \xi(\mathbf{D}\cdot\mathbf{A} + \mathbf{A}\cdot\mathbf{D} - 2\mathbf{D}:\mathbf{A}_4) + 2C_I\dot{\gamma}(\mathbf{I} - 3\mathbf{A})\right) \qquad 2.17$$

in which α is a number between 0 and 1, and attempts to retard the rate of fiber orientation. The model in Eq. 2.17 has shown benefits [28,30] over its former counterpart, but some authors have suggested that this model violates objectivity [24]. To modify this equation to accommodate experimentally observed changes in orientation, and to not violate objectivity, Wang et al. [24,23] incorporated the use of a "reduced strain closure" model. As the name suggest, the term containing the fourth order orientation tensor is modified to allow slowing of the orientation kinetics.

$$\frac{D\mathbf{A}}{Dt} = \mathbf{W}\cdot\mathbf{A} - \mathbf{A}\cdot\mathbf{W} + \xi\left\{\mathbf{D}\cdot\mathbf{A} + \mathbf{A}\cdot\mathbf{D} - 2\left[\mathbf{A}_4 + (1-\kappa)(\mathbf{L}_4 - \mathbf{M}_4:\mathbf{A}_4)\right]:\mathbf{D}\right\} \qquad 2.18$$
$$\ldots + 2\kappa C_I\dot{\gamma}(\mathbf{I} - 3\mathbf{A})$$

$$\mathbf{L}_4 = \sum_{i=1}^{3}\lambda_i(\mathbf{e}_i\mathbf{e}_i\mathbf{e}_i\mathbf{e}_i) \qquad 2.19$$

$$M_4 = \sum_{i=1}^{3}\mathbf{e}_i\mathbf{e}_i\mathbf{e}_i\mathbf{e}_i \qquad 2.20$$

In Eqs. 2.18- 2.20, λ_i and $\mathbf{e}_i$ are the eigenvalues and eigenvectors of **A**, respectively**,** κ is the reduced strain closure coefficient and is responsible for slowing the eigenvalue kinetics, and $\mathbf{L}_4$ and $\mathbf{M}_4$ are fourth order tensors constructed from the eigenvalues and vectors as indicated. Another addition was made to this model that enables fibers to "diffuse" in a non-isotropic manner [23]. This addition, suggested by Wang et al. [23], uses an anisotropic rotary diffusion term and tries to represent a more realistic view of fiber-fiber interactions. This form of the model is not shown here for brevity, but the avid reader is referred to the paper of interest [24,23]. This model was applied to the injection molding of a long fibers in a center-gated disk [22]. According to Nguyen et al. [22], the model still does not predict long fiber orientation well enough for accurate property prediction. The application of this model with rheological experiments has not yet been accomplished to our knowledge.

The first true continuum based model, known to us, which accounts for semi-flexible fibers is one proposed by Strautins and Latz (2007) [65] and is referred to here as the Bead-Rod model. In this model, a semi-flexible fiber is modeled as two connected "rods" of orientation **p** and **q** and length l_B that may rotate, or flex, about a pivot point as in Figure 3.

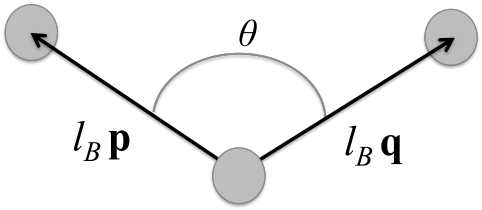

Figure 2.3: Semi-flexible fiber of Strautins and Latz, 2007. Fiber is constructed by two connected orientation vectors **p** and **q**. A bending force is provided by a restorative potential.

The semi-flexible fiber has a resistance to bending, and is accounted for by a restorative potential that is attached to both rods. When the fiber is perfectly straight, the potential is at equilibrium and subjects no restorative force on the fiber. However, if the fiber is placed in a flow that may induce fiber curvature, the fiber may bend in response to the drag flow on the "beads".

To model the orientation changes of such fibers, the authors develop the kinematic equations for the bead and rod fiber in Figure 3. Several assumptions are made along the way. First, this model applies for fibers that are only semi-flexible for which **p** ≈ **-q**. The exact extent to this restriction is not fully described, but an emphasis on its importance is stated. Secondly, the model fiber is to be in an infinitely dilute suspension where only hydrodynamic effects may exist, and does not allow for interactions between different fibers. Other assumptions made are more of a mathematical nature. For example, it was assumed that at any given time, the first and second moments of each orientation vector **p** and **q** were equal. Assumptions about the closure approximations needed were also made. Specifically, the moments of the orientation vectors needed to construct the closure were assumed and arguments concerning the symmetry of these moments were made. In this model, the authors make use of a form of the quadratic closure, and choose this mostly for simplicity. In the end, a model is formed that contained 3 moments of the **p** and **q** vectors in the following manner,

$$\mathbf{A} = \int\int \mathbf{pp}\ \psi(\mathbf{p},\mathbf{q},t)d\mathbf{p}d\mathbf{q} \qquad 2.21$$

$$\mathbf{B} = \int\int \mathbf{pq}\ \psi(\mathbf{p},\mathbf{q},t)d\mathbf{p}d\mathbf{q} \qquad 2.22$$

$$\mathbf{C} = \int\int \mathbf{p}\psi(\mathbf{p},\mathbf{q},t)d\mathbf{p}d\mathbf{q} \qquad 2.23$$

Eq. 2.21 is similar to what exists in rigid rod theory and describes the second moment of any one of the rods with respect to the orientation distribution function. Another orientation tensor describes the mixed product of both rod vectors with the orientation distribution function, Eq. 2.22. Lastly, the first moment of the distribution function, using either rod's orientation vector, Eq. 2.23 is also formed. It is important to note that this vector does not vanish in the case of the Bead-Rod model as it does for purely rigid rod model. The equations that describe how a given flow field affects the orientation functions are given in the following equations:

$$\frac{D\mathbf{A}}{Dt} = \left(\mathbf{W}\cdot\mathbf{A} - \mathbf{A}\cdot\mathbf{W}\right) + \left(\mathbf{D}\cdot\mathbf{A} + \mathbf{A}\cdot\mathbf{D} - \left(2\mathbf{D}:\mathbf{A}\right)\mathbf{A}\right) + \ldots\frac{l_B}{2}[\mathbf{Cm} + \mathbf{mC} - 2(\mathbf{m}\cdot\mathbf{C})\mathbf{A}] - 2k[\mathbf{B} - \mathbf{A}\ \mathrm{tr}(\mathbf{B})] \quad 2.24$$

$$\frac{D\mathbf{B}}{Dt} = \left(\mathbf{W}\cdot\mathbf{B} - \mathbf{B}\cdot\mathbf{W}\right) + \left(\mathbf{D}\cdot\mathbf{B} + \mathbf{B}\cdot\mathbf{D} - \left(2\mathbf{D}:\mathbf{A}\right)\mathbf{B}\right) + \ldots\frac{l_B}{2}[\mathbf{Cm} + \mathbf{mC} - 2(\mathbf{m}\cdot\mathbf{C})\mathbf{B}] - 2k[\mathbf{A} - \mathbf{B}\ \mathrm{tr}(\mathbf{B})] \quad 2.25$$

$$\frac{D\mathbf{C}}{Dt} = \nabla\boldsymbol{v}^t\cdot\mathbf{C} - (\mathbf{A}:\nabla\boldsymbol{v}^t)\mathbf{C} + \frac{l_B}{2}[\mathbf{m} - \mathbf{C}\left(\mathbf{m}\cdot\mathbf{C}\right)] - k\,\mathbf{C}[1 - \mathrm{tr}(\mathbf{B})] \quad 2.26$$

$$\mathbf{m} = \frac{\partial^2 v_{\mathrm{i}}}{\partial x_{\mathrm{j}}\partial x_{\mathrm{k}}} A_{\mathrm{jk}}\,\mathbf{e}_{\mathrm{i}} \quad 2.27$$

Within these equations, *tr*() represents the trace of a specified tensor and *k* is the restorative potential. Because this model only accounts for viscous flow effects, flexibility caused by flow will only occur when second order spatial derivatives of the velocity term exist in Eq. 2.27. Within Eq. 2.27, **m** is a vector formed by the summation over the indicies *ijk*, and $\boldsymbol{e}_{\mathrm{i}}$ are the vector component dyads. Hence, in simple flows (ie. simple shear, simple elongation), the model does not predict flow induced flexibility. The authors show an example of channel flow for fibers initially straight but randomly oriented. Their simulation showed that the orientation components of the **A** tensor, when plotted versus the dimensionless channel height, provided a profile that exhibits larger flow induced orientation when compared to that of the Folgar-Tucker model. This was said to be a direct cause of the flexibility of the fiber because the flexibility forced the fiber to bend (and hence orient) more in the center of the channel flow. Other than this example, the Bead-Rod model has gone unexamined to our knowledge.

Another model that attempts to account for flexibility, among many other effects, is made through an application of the GENERIC framework [45] and is applicable for non-dilute suspensions. The application of this framework was constructed to supply a mesoscopic level of information pertaining to the microstructural fiber evolution and the resulting stresses within the suspension. The advantages of such a model remain in its guaranteed consistency with hydrodynamic evolution and thermodynamics [45]. The disadvantages of this model exist in the indirect relation between fiber dynamics and the meaning of the model parameters that determine them. More specifically, this means that suspension characteristics must be captured through phenomenological terms such as free energy parameters and dissipation potential parameters, which are not direct measurable functions of fiber or material properties. The authors stress, however, the importance of understanding phenomena, such as complex fiber dynamics, in terms of a framework created from classical theories.

The model developed from this framework provides a description of the fluid flow kinematics with a set of self-consistent stress, polymer configuration, and fiber orientation equations. In terms of fiber orientation, the dynamics of this model stems from that of Jeffery's model, but is quite unique in the form of dissipation term that is

used. The dissipation term is a function of free energy, and consists of both an energy and an entropy term. Likewise, the stress equation also makes extensive use of these terms and proposes a link between fiber orientation dynamics and flow kinematics.

The model, in all, contains 6 parameters that in turn control fiber flexibility, fiber-fiber coupling and fiber-polymer coupling, fiber mobility, polymer mobility, and fiber-polymer mobility. It was found that an increase in fiber-fiber mobility decreases the values of the steady state shear viscosity, the first normal stress difference function, and their transient overshoots. Likewise, a decrease in the polymer mobility causes a similar effect, but the magnitudes of the viscosity and first normal stress difference overshoots are more pronounced. This model also suggests that an increase in fiber-polymer mobility decreases the steady state viscosity and the values of the first normal stress difference function. Additionally, the viscosity overshoot magnitudes are less. Flexibility was found to increase viscosity, and has experimental evidence found in literature that validates this [4,5,15]. These effects are more pronounced at high aspect ratio. Additionally, it is predicted that rigid fibers tend to orient more than flexible fibers, and is more apparent at high concentration and aspect ratio. This behavior has been reported both numerically and experimentally, and is sometimes believed to be caused by flocculation [16,4]. Lastly, increased fiber-fiber coupling is seen to enhance viscosity and values of the first normal stress function, and decreased fiber-polymer coupling is seen to increase both material functions as well. Additionally, these results are fairly sensitive to changes in these parameters.

Fortunately, this model has had some evaluation both in terms of its ability to fit transient long fiber rheology, and in its ability to predict long fiber orientation (using parameters fit from the rheology) [15]. In this experiment, Keshtkar et al. [15] determined model parameters for long fiber suspensions (ϕ = 0.03, semi-dilute) of different flexibilities to fit the transient shear rheology at 1 s^{-1}. From this, the authors captured the transient viscosity measurements well, both in overshoot magnitude, overshoot peak width, and strain at which steady state is reached. Parameters found from the transient viscosity, however, does not result in accurate predictions of N_1. The transients predicted here match the magnitude of N_1 well, but are too fast and does not match the breadth of this peak. The authors state that this may, in part, be due to the inhomogeneous shear field of the parallel plate geometry used in their experimentation. Other possibilities for this discrepancy might be due to flocculation of fibers, which are not accounted for in the model. Using the model parameters at 1 s^{-1}, the authors compare model predictions to experimental measurements at 0.5 s^{-1} and 5 s^{-1}. At the lower shear rate, the model over predicts both the overshoot and the steady state value of the viscosity. This discrepancy is more pronounced at higher flexibility. At the larger shear rate, however, the model under predicts the overshoots and steady state values. The shear thinning behavior was also well correlated between prediction and experiment. When used to predict orientation evolution, the model qualitatively agrees, but consistently over predicts the rate of orientation for all fibers explored. The authors acknowledge the fact that much work remains to accurately understanding the dynamics associated with long fiber suspensions.

2.3.1(b) Stress Models. In this subsection, current stress models commonly used in complex simulations will be discussed. After this subsection, a discussion of direct simulations and their relevance will be presented.

Most of the work pertaining to the understanding of suspension stress theory can be traced back to Ericksen (1960) [72], Batchelor (1971) [52], Goddard (1978) [68], Dinh and Armstrong (1984) [69], Gibson and Toll (1999) [12], and Shaqfeh and Fredrickson (1990) [70]. In general, such researchers often look for a form of a stress equation such that the total stress of the suspension is a linear combination of stresses from the suspending medium and stresses from the particles [71, 14].

$$\boldsymbol{\sigma} = -P\mathbf{I} + 2\eta_{Matrix}\mathbf{D} + \boldsymbol{\tau}_{Particles} \qquad 2.28$$

In Equation 2.28, P is the isotropic pressure, η_{Matrix} is the suspending medium viscosity and must be introduced through a constitutive equation, such as that for a Newtonian fluid or common non-Newtonian fluids [14]. The most general form for the stress on the suspension is,

$$\boldsymbol{\sigma} = -P\mathbf{I} + 2\eta_{Matrix}\mathbf{D} + 2\eta_{Matrix}\phi\left\{a\mathbf{A}_4 : \mathbf{D} + b\left(\mathbf{D}\cdot\mathbf{A} + \mathbf{A}\cdot\mathbf{D}\right) + c\mathbf{D} + f\mathbf{A}D_r\right\} \qquad 2.29$$

wherein, a, b, c and f are geometric shape factors, and D_r is the rotary diffusivity from Brownian motion [60]. For high aspect ratio particles, such as fibers, b and c are 0. For long fibers, Brownian motion is negligible and D_r may also be set to 0. Hence the stress theory for fibers reduces to,

$$\boldsymbol{\sigma} = -P\mathbf{I} + 2\eta_{Matrix}\left(\mathbf{D} + N\mathbf{A}_4 : \mathbf{D}\right) \qquad 2.30$$

where N is used to represent an anisotropic fiber stress, and is a function of the fiber concentration and aspect ratio [71]. This stress equation, Equation 2.30, was developed by Ericksen and Hand [72,73]. Again, the fourth order orientation tensor appears, and almost always must be accompanied by a closure approximation. A slightly different form of this stress equation was introduced by Batchelor (1970) [75], and is said to describe fluid-particle interactions and particle-particle interactions,

$$\boldsymbol{\sigma} = -P\mathbf{I} + 2\eta_{Matrix}\left(\mathbf{D} + N\mathbf{A}_4 : \mathbf{D} - \frac{1}{3}N\mathbf{A}\mathbf{I} : \mathbf{D}\right) \qquad 2.31$$

Much theoretical work has been done to determine values for N [52,70,74,69]. For a dilute suspension of fibers, Batchelor (1971) suggested an empirical form,

$$N = \frac{\pi n L^3}{6\ln(2L/D)}\left(\frac{1 + 0.64\varepsilon}{1 - 1.5\varepsilon} + 1.659\varepsilon^2\right) \qquad 2.32$$

$$\varepsilon = \frac{1}{\ln(2L/D)} \qquad 2.33$$

where n, again, is the number of fibers per unit volume. Corrections to dilute suspension theory for two body interactions was suggested by Shaqfeh et al. [71], and is valid for $nL^3 < \ln(2L/D)^2$,

$$\text{aligned suspension}: \quad N = N^{dilute} + 8.583 \times 10^{-3} \frac{\pi (nL^3)^2}{\ln(2L/D)^3} \tag{2.34}$$

$$\text{isotropic suspension}: \quad N = N^{dilute} + 9.250 \times 10^{-3} \frac{\pi (nL^3)^2}{\ln(2L/D)^3} \tag{2.35}$$

where N^{dilute} is formed by Equations 2.25 and 2.26. For the semi-dilute suspension ($D < n < L$), Dinh and Armstrong [69] suggested,

$$N = \frac{\pi n L^3}{6 \ln(2h/D)} \tag{2.36}$$

$$\begin{aligned} &\text{random orientation}: \quad h = \frac{1}{nL^2} \\ &\text{aligned orientation}: \quad h = \frac{1}{\sqrt{nL}} \end{aligned} \tag{2.37}$$

An expression for h for systems that are neither random nor perfectly aligned has also been suggested in terms of a combination of these two values [71]. Some stress expressions also include a stress enhancement due to presence of fiber volume fraction, as suggested by Lipscomb (1988) [80] for high aspect ratio particles,

$$\boldsymbol{\sigma} = -P\mathbf{I} + 2\eta_{Matrix}\left(\mathbf{D} + c_1\phi\mathbf{D} + N\mathbf{A}_4 : \mathbf{D}\right) \tag{2.38}$$

where c_1 may be fit to account for stress enhancement due the presence of fibers when they are fully aligned [2]. No theory, however, exists for fiber systems that are semi-concentrated (or higher) and some authors have chosen not to use analytical expressions for N, but rather choose to use it as a fitting parameter [19]. Additionally, strictly speaking, no stress theory to date considers fibers that are flexible.

Combining these stress expressions with the orientation models previously discussed have yielded varying amounts of success, but very limited success exists with long concentrated fibers [19,22]. Particularly, modeling rheological measurements for concentrated fibers using the Folgar-Tucker model with such a stress contribution as Equation 2.38, often yields shear stress and normal stress difference overshoots that cannot be fit, either in magnitude and/or peak breadth [22,19]. This is thought to be primarily due to our general lack of understanding of concentrated fiber interactions, especially when fiber flexibility is a non-negligible variable. This fact has led many authors to explore a more fundamental approach to modeling fibers and their interactions through direct simulations.

2.3.2 Direct Simulation

Direct simulations are used to approach the modeling of fibers from a more fundamental approach and are generally conducted to explore and understand a wide variety of phenomena [5]. Model fiber equations are usually constructed for a single or (at most) a small population of fibers and consist of the equations of forces and torques that evolve the particles and fiber configurations over time [5]. Most authors use this

opportunity to try and explore phenomena believed to be of significance or at least of interest, such as long and short range hydrodynamic effects, flexibility, Coulombic forces, and frictional forces [1,4,27,77,14]. In theory, such simulations are only limited by the computational resources that exist [5].

Direct simulations have been used to probe hydrodynamic effects for relatively dilute rigid fibers, and slowly began to consider more complex scenarios [81,82,77]. Rahnama et al. (1995) [81] studied the hydrodynamic interactions in dilute and semi-dilute suspensions. In this work, slender body theory was used to model short-range hydrodynamic interactions [81]. It was found that as concentration increases, such as in the case from dilute to semi-concentrated, the hydrodynamic interactions become of less significance [81]. Sundararajakumar and Koch [17] used numerical simulations for a population of fibers that were allowed to exhibit mechanical contacts in the form of normal forces and contact points. In their treatment, however, they purposely ignored short-range hydrodynamic interactions on the account that they believed these effects to be negligible in suspensions above the semi-dilute concentration regime. They also showed that such forces, such as lubrications forces, are not strong enough to prevent adjacent fibers from touching. It was found that suspension viscosity is enhanced with fiber contacts and increases nonlinearly with concentration. These fiber contacts also affect fiber orientation through increased fiber flipping. Mackaplow and Shaqfeh (1996) [74] used slender body theory to accurately account for long rage hydrodynamic effects. Simulations considering both short range and long-range hydrodynamic forces for many body interactions were attempted by Claeys and Brady (1993) [78,79]. Yamane (1994) [76] and Fan (1998) [77] simulated hydrodynamic interactions between rigid fibers and reported relatively good agreement with experiment.

One of the first fiber theories to describe the evolution of individual flexible fibers was proposed by Hinch (1975) [83]. Hinch used slender body theory for Stokes flow for a small, flexible, and inextensible thread. A force balance, due to the hydrodynamic effects of the suspending medium, is used to describe the motion of a single, perfectly flexible, thread in a dilute suspension. The model consists of two partial differential equations that are solved simultaneously to determine the motion of the thread with a pre-prescribed initial configuration,

$$\frac{\partial \mathbf{x}}{\partial t} - \frac{\partial T}{\partial s}\frac{\partial \mathbf{x}}{\partial s} = \frac{1}{2}T\frac{\partial^2 \mathbf{x}}{\partial s^2} + \mathbf{v}(\mathbf{x},t) \qquad 2.39$$

$$\frac{\partial^2 T}{\partial s^2} - \frac{1}{2}\left(\frac{\partial^2 \mathbf{x}}{\partial s^2}\right)\bullet\left(\frac{\partial^2 \mathbf{x}}{\partial s^2}\right)T = -\frac{\partial \mathbf{x}}{\partial s}\bullet\frac{\partial \mathbf{v}(\mathbf{x},t)}{\partial s} \qquad 2.40$$

where s is the arc length along the fiber, $\mathbf{x}$ is a function $\mathbf{x}(s,t)$ and is the 3-dimensional position vector of each point along the fiber, T is a function $T(s,t)$ and is the tension in the fiber, and $\boldsymbol{v}$ is the velocity field of the fluid. Hinch found that a highly non-aligned fiber will ultimately align with the flow field. This may be used to simulate the configurational changes of a thread in an arbitrary flow field, but does not account for any fiber interactions.

Later, Goddard and Huang (1983) [67] tried to improve upon this model for non-dilute suspensions by introducing fiber mobility into the above set of equations. The

mobility tensor is used to describe a flexible fiber whose motion is affected by the hydrodynamic effects of neighboring fibers. Application of this theory into Hinch's model becomes,

$$\frac{\partial \mathbf{x}}{\partial t} - K_{\mathrm{L}} \frac{\partial T}{\partial s} \frac{\partial \mathbf{x}}{\partial s} = T\mathbf{K}_{\mathrm{T}} \bullet \frac{\partial^2 \mathbf{x}}{\partial s^2} + \mathbf{v}(\mathbf{x},t) \qquad 2.41$$

$$\frac{\partial}{\partial s}\left(K_{\mathrm{L}} \frac{\partial T}{\partial s}\right) - \left(\frac{\partial^2 \mathbf{x}}{\partial s^2}\right) \bullet \left(\frac{\partial^2 \mathbf{x}}{\partial s^2}\right) K_{\mathrm{N}} T = -\frac{\partial \mathbf{x}}{\partial s} \bullet \frac{\partial \mathbf{v}(\mathbf{x},t)}{\partial s} \qquad 2.42$$

where $\boldsymbol{K}_T$ is the transverse mobility tensor, and K_L and K_N are the scalar lateral and normal components of the mobility tensor, respectively. One can see that Hinch's model is just a special case of the Goddard and Huang model, in which the mobility components take on constant values. Despite this work, few publications utilize its findings, which are most likely due to the lack of the dynamics captured, the lack of understanding of an appropriate mobility tensor, and cumbersome equations.

A more successful method of describing the configuration evolution of long fibers has been done by considering a connection of spheroids [5,14,18]. Yamamoto and Matsuoka (1993,1994) [84,85] modeled flexible fibers as chains of rigid spheres connected by springs, which provided resistance to bending and twisting. Similar to Yamamoto and Matsuoka, Skejtne et al. (1997) [18] modeled inextensible chains of rigid prolate spheroids connected through ball and socket joints in simple shear flow and a squeeze flow. Hydrodynamic interactions between different fibers were neglected, as well as fluid inertia, but interparticle forces, colloidal forces, and short-range repulsions forces were taken into consideration. When these fibers were made sufficiently stiff, they reproduced orbital stability found from Jeffery's model. Flexible fibers produced more complex dynamics, such as orbital drift, and a variety of complex dynamics including configurational changes and pole-vault dynamics near wall boundaries [18]. No relationship concerning the fiber configuration and the fluid stress was explored.

Joung and Fan (2001) [14] also simulated flexible fibers, for the case of simple shear flow and a Newtonian matrix, by modeling the fibers as a chain of spherical beads. In this model, viscous drag and long-range hydrodynamic effects were accounted for, as well as short-range lubrication effects. Stress theory was incorporated into this model with the use of theory from Batchelor [75]. A different form of this stress theory is often used for direct simulations, as opposed to those forms discussed in Section 2.3.1(b). In this form, a sum of the individual fiber stresses is averaged within a statistically sound volume,

$$\boldsymbol{\sigma} = -P\mathbf{I} + 2\eta_{Matrix}\mathbf{D} + \frac{1}{V}\int \boldsymbol{\tau}^P \, dV \qquad 2.43$$

where $\boldsymbol{\tau}^P$ is the stress contribution of a single particle (p) in the volume of interest. In practice, the particle term must be discretized into a finite number of contributions that account for fiber torque and stresslets on each fiber [75]. In this equation, the integral term involving τ^p often takes the form of,

$$\int \boldsymbol{\tau}^p \, dV = \sum_p \left(\mathbf{S}^p + \frac{1}{2}\varepsilon \cdot \mathbf{T}^p\right) \qquad 2.44$$

$$\mathbf{S}^p = \frac{1}{2}\iint \left[\mathbf{xt} + \left(\mathbf{xt}\right)^T\right]\psi(\mathbf{p},t)d\mathbf{p}ds \qquad 2.45$$

$\mathbf{S}^p$ is the stresslet on a particle, ε is the third-rank permutation tensor, and $\boldsymbol{T}^p$ is the torque vector on a particle. In the expression for a particle stresslet, Eq. 2.45, $\mathbf{x}$ is the position vector on a fiber contour, $\boldsymbol{t}$ is the traction vector, and s is the arc length position of the fiber [14,86]. Simulations of Joung et al. [14] predicted relative viscosity as a function of volume fraction for several different fiber materials. These predictions were in good agreement with the experimental findings of Bibbo (1987) [26]. They also used this work to approximate C_I for the Folgar-Tucker model.

Work done to understand frictional contacts, the effect of fiber shape on suspension viscosity, and fiber flocculation has also been accomplished using direct simulation methods [5,87]. In these simulations, long fibers were modeled as rigid spherocylinders linked by ball and socket joints. Using stress theory of Mackaplow and Shaqfeh (1996) [74] and Sundararajakumar and Koch (1997) [17], they devised a stress model that takes both hydrodynamic and non-hydrodynamic particle interactions into account. Specifically, they were interested in frictional contacts and some short-range repulsive forces (but not lubrication), because such contacts have been shown sufficient to cause flocculation [87]. The model fibers were subjected to simple shear flow. From their numerical experiments, rheological properties and fiber microstructure were found to be sensitive to equilibrium fiber shape, aspect ratio, friction, concentration, and matrix properties. Effects of fiber flexibility on suspension viscosity, however, did not agree with the comparative experimental work of Goto (1986) [39]. Next, in the absence of fiber friction they found both rigid and flexible fiber suspension viscosities increased linearly with concentration [5,75]. Additionally, they found flocculation to also be very dependent on fiber friction, stiffness, and equilibrium shape [5,87]. They found flocculation to be disrupted at higher shear rates, which is consistent with reports found within the literature [88,4].

Direct simulations are of great theoretical importance, and help explain a wide variety of interesting phenomena. However, the application of such models to industrial processes is almost never possible, due to the very high computational work loads needed to simulate interacting fibers, complex flows, and real-life geometries. As of now, much work is still needed to efficiently and accurately predict and optimize manufacturing processes of fiber composites.

2.3.4 Summary of Modeling

In this section, descriptions of fiber orientation and stress models were given by discussing their two classifications: continuum based and direct simulation based models. Continuum based models inherently describe a population of fibers and contain functions and variables that represent measurable quantities. Most continuum based orientation models stemmed from the work of Jeffery (1922) [89]. This work slowly began to consider more realistic dynamics including fiber interaction through the use of isotropic rotary diffusion, anisotropic rotary diffusion, and delayed orientation kinetics [22, 23, 24 61], and also was used to consider semi-flexible fibers [65]. In order to complete the description of fiber mechanics, a stress equation is needed to predict fiber stress contributions. Most used stress theory originated from theory proposed by Ericksen [72]

and Batchelor [75], which stems from continuum mechanics. Other authors, however, looked at kinetic theory of polymer liquids and thermodynamics as a fundamental basis for describing fiber orientation and their corresponding stresses contributions. Direct simulations, on the other hand, were seen to provide a first principles approach to understanding fiber dynamics and enable complex dynamics to be considered, including fiber-fiber interactions and flexibility. However, these simulations were said to be much more computationally expensive, and presently provide only limited, if any, industrial significance.

2.4 References

1. K.A. Ericsson, S. Toll, J-A.E. Manson. Sliding plate rheometry of planar oriented concentrated fiber suspensions. Rheologica Acta, 36, 397-405, 1997.
2. J. Thomasset, P.J. Carreau, B. Sanchagrin, G. Ausias, Rheological properties of long glass fiber filled polypropylene. Journal of Non-Newtonian Fluid Mechanics, 123, 25-34, 2005.
3. T. S. Creasy, S. G. Advani, Transient rheological behavior of a long discontinuous fiber-melt system. Journal of Rheology, 40(4), 497-518, 1996.
4. M. Keshtkar, M.C. Heuzey, P.J. Carreau, Rheological behavior of fiber-filled model suspensions: Effect of fiber flexibility, Journal of Rheology, 53(3), 631-650, 2009.
5. L.H. Switzer III, D.J. Klingenberg, Rheology of sheared flexible fiber suspensions via fiber-level simulations, Journal of Rheology, 47(3), 759-778, 2003.
6. C. Servais, J-A.E. Manson, Fiber-fiber interaction in concentrated suspensions: Disperse fibers, Journal of Rheology, 43(4), 991-1004, 1999.
7. R. Guo, J. Azaiez, C. Bellehumeur, Rheology of fiber filled polymer melts: role of fiber-fiber interactions and polymer-fiber coupling, Polymer Engineering and Science, 45(3) 385-399, 2005.
8. R.S. Jones, R.W. Roberts, Anisotropic shear flow in continuous fiber composites. Composites 25(3), 171-176, 1994.
9. C.P.J. Bennington, R.J. Kerekes, J.R. Grace, The yield stress of fiber suspensions, The Canadian Journal of Chemical Engineering, 68, 748-757, 1990.
10. S. Toll, J.-A.E. Manson, Elastic compression of a fiber network, Journal of Applied Mechanics, 62, 223-226, 1995.
11. T.S. Creasy, S.G. Advani, A model long-discontinuous-fiber filled thermoplastic melt in extensional flow, Journal of Non-Newtonian Fluid Mechanics, 73, 261-278, 1997.
12. A.G. Gibson, S. Toll, Mechanics of the squeeze flow of planar fibre suspensions, Journal of Non-Newtonian Fluid Mechanics, 82, 1-24, 1999.
13. S.G. Shuler, S.G. Advani, Transverse squeeze flow of concentrated aligned fibers in viscous fluids. Journal of Non-Newtonian Fluid Mechanics,
14. C.G. Joung, N. Phan-Thien, X.J. Fan, Direct simulation of flexible fibers, Journal of Non-Newtonian Fluid Mechanics, 99, 1-36, 2001.
15. M. Keshtkar, M.-C. Heuzey, P.J. Carreau, M. Rajabian, C. Dubois, Rheological properties and microstructural evolution of semi-flexible fiber suspensions under shear flow, Journal of Rheology 54(2), 197-222, 2010.
16. L.H. Switzer, D.J. Klingenberg, Flocculation in simulations of sheared fiber

suspensions, International Journal of Multiphase Flow, 30, 67-87, 2004.
17. R.R. Sundararajakkumar, D. L. Koch, Structure and properties of sheared fiber suspensions with mechanical contacts, Journal of Non-Newtonian fluid Mechanics, 73, 205-239, 1997.
18. P. Skjetne, R. Ross, D.J. Klingenberg, Simulation of single fiber dynamics, Journal of Chemistry Physics, 107(6), 2108-2121, 1997.
19. A.P.R. Eberle, D. G. Baird, P. Wapperom, and G.M. Vélez-García, Obtaining reliable transient rheological data on concentrated short fiber suspensions using a rotational rheometer, Journal of Rheology, 53, 1049-1069, 2009.
20. M. Doi, S.F. Edwards, The Theory of Polymer Dynamics, Oxford University Press: New York, 1988.
21. P.J. Hine, N. Davidson, R.A. Duckett, A.R. Clarke, I.M. Ward, Hydrostatically extruded glass–fiber reinforced polyoxymethylene. I. The development of fiber and matrix orientation, Polymer Composites, 17, 720–729, 1996.
22. B. Nguyen, S. Bapanapalli, J. Holbery, M. Smith, V. Kunc, B. Frame, J. Phelps, C.L. Tucker III, Fiber Length and Orientation in Long-Fiber Injection-Molded Thermoplastics-- Part I: Modeling of Microstructure and Elastic Properties, J. Thermoplastic Composite Materials, 42, 1003-1029, 2008.
23. J. Phelps, C.L. Tucker III, An anisotropic rotary diffusion model for fiber orientation in short- and long-fiber thermoplastics, Journal of Non-Newtonian Fluid Mechanics 156 165-176, 2009.
24. J. Wang, J. O'Gara, C.L. Tucker III, An objective model for slow orientation kinetics in concentrated fiber suspensions: Theory and rheological evidence. Journal of Rheology, 52(5), 1179-1200, 2008.
25. C. Mobuchon, P.J. Carreau, M.-C. Heuzey, M. Sepehr, G. Ausias, Shear and Extensional Properties of Short Glass Fiber Reinforced Polypropylene. Polymer Composites, 26(3), 247-264, 2005.
26. M. Bibbo, Rheology of semi-concentrated fiber suspensions. Ph.D. thesis, Michigan Institute of Technology, 1987.
27. M. Petrich, D. Koch, C. Cohen, An experimental determination of the stress-microstructure relationship in semi-concentrated fiber suspensions. Journal of Non-Newtonian Fluid Mechanics, 95, 101-133, 2000.
28. M. Sepehr, G. Ausias, P.J. Carreau, Rheological properties of short fiber filled polypropylene in transient flow. Journal of Non-Newtonian Fluid Mechanics, 123, 19–32, 2004a.
29. M. Sepehr, G. Ausias, P.J. Carreau, Rheological properties of short fiber model suspensions. Journal of Rheology 48, 1023–1048, 2004b.
30. A. Eberle, D.G. Baird, P. Wapperom, G. Velez-Garcia, Using transient shear rheology to determine material parameters in fiber suspension theory. Journal of Rheology, 53(3), 685-705, 2009.
31. L.A. Mondy, H. Brenner, S.A. Altobelli, J.R. Abbott and A.L. Graham, Shear-induced particle migration in suspensions of rods. J. Rheol 38 (1994), pp. 444–452.
32. M.L. Becraft, A. Metzner, The rheology, fiber orientation, and processing behavior of fiber-filled fluids. Journal of Rheology 36(1), 143-174, 1992.
33. Y. Chan, J.L. White, Y. Oyanagi, A fundamental study of the rheological properties of glass-fiber-reinforced polyethylene and polystyrene melts. Journal of Rheology,

22(5), 507-524, 1978.
34. E. Ganani, R. Powell, Rheological properties of rodlike particles in a Newtonian and a non-Newtonian fluid. Journal of Rheology, 30(5), 995-1013, 1986.
35. R.M. Soszynski and R.J. Kerekes, Elastic interlocking of nylon fibers suspended in liquid. Part 1. Nature of cohesion among fibers. Nord. Pulp Paper Res. J. 3 (1988), pp. 172–179.
36. R.M. Soszynski and R.J. Kerekes, Elastic interlocking of nylon fibers suspended in liquid. Part 2. Process of interlocking. Nord Pulp Paper Res. J. 3 (1988), pp. 180–184.
37. S. Toll and J.-A.E. Manson, Elastic compression of a fiber network, Journal of Applied Mechanics Transactions ASME, 62 (1), 223–226, 1995.
38. M. Chaouche, D. Koch, Rheology of non-Brownian rigid fiber suspensions with adhesive contacts. Journal of Rheology 45(2), 369-382, 2001.
39. S. Goto, H. Nagazono, H. Kato, The flow behavior of fiber suspensions in Newtonian fluids and polymer solutions. II: Capillary flow. Rheologica Acta**,** 25(3), 246-256, 1986.
40. A.G. Gibson, A.N. McClelland, Fibers Reinforced Composites, Paper 32, University of Liverpool, Institute of Mechanical Engineers, London, 1986, p. 99.
41. R. Kotsilkova, Dynamic rheological properties of glass fiber suspensions, Theoretical and Applied Rheology, in Proceedings of XIth International Congress on Rheology, edited by P. Moldenaers, and R. Keunings Elsevier Science, Brussels, Belgium, 1992, 856–858.
42. N.J. Mills, The rheology of filled polymers. Journal of Applied Polymer Science, 15, 2791-2805, 1971.
43. J.L. White, L. Czarnecki, H. Tanaka, Experimental studies of the influence of particle and fiber reinforcement on the rheological properties of polymer melts. Rubber Chemical Technology, 53, 823-835, 1980.
44. T. Kitano, T. Kataoka, Y. Nagatsuka, Dynamic flow properties of vinylon- and glass-fiber reinforced polyethylene melts. Rheologica Acta, 23(4), 408-416, 1984a.
45. M. Rajabian, C. Dubois, M. Grmela, Suspensions of semiflexible fibers in polymer fluids: rheology and thermodynamics. Rehologica Acta. 44, 521-535, 2005.
46. S.E. Barbosa, D.R. Ercoli, M.A. Bibbo, J. Kenny, Rheology of short-fiber composites: a systematic approach. Composite Structures, 27, 83-91, 1994.
47. S.E. Barbosa, M.A. Bibbo, Fiber motion and the rheology of suspensions with uniform fiber orientation. Journal of Polymer Science Part B: Polymer Physics, 38, 1788-1799, 2000.
48. M.R. Kamal, A.T. Mutel, Elongational behavior of short glass fiber reinforced polypropylene melts. Polymer Composites, 5, 289-298, 1984.
49. R.B. Bird, R.C. Armstrong, O. Hassagar, Dynamics of polymeric liquids. John Wiley and Sons, Inc. New York, 1987, Vol 1.
50. J. Mewis, B. Metzner, The rheological properties of suspensions of fibers in Newtonian fluids subjected to extensional deformations. Journal of Fluid Mechanics, 62(3), 593-600, 1974.
51. J. Ferec, M.-C. Heuzey, J. Perez-Gonzalez, L. Vargas, G. Ausias, P.J. Carreau, Investigation of the rheological properties of short glass fiber-filled polypropylene in extensional flow. Rheologica Acta, 48, 59-72, 2009.

52. G.K. Batchelor, The stress generated in a non-dilute suspension of elongated particles by pure straining motion. Journal of Fluid Mechanics, 46, 813-829, 1971.
53. T. Kitano, T. Kataoka, The rheology of suspension of vinylon fibers in polymer liquids. I. Suspensions in silicone oil. Rheologica Acta, 20, 390-402, 1981.
54. R. Meyer, D. Wahren, On the elastic properties of three-dimensional fibre networks. Svensk Papperstidn, 67(10), 432-436, 1964.
55. L.F. Carter, A study of the rheology of suspensions of rod-shaped particles in a Navier-Stokes liquid. Ph.D. thesis, University of Michigan, Ann Arbor MI, 1967.
56. H.M. Laun, Orientation effects and rheology of short glass fiber-reinforces thermoplastics. Colloid and Polymer Science, 262, 257-269, 1984.
57. M. A. Bibbo and R. C. Armstrong, "Rheology of Semi-Concentrated Fiber Suspensions in Newtonian and Non-Newtonian Fluids", Manufacturing Science of Composites, T.G. Gutowski (Ed.), ASME Publication, New York 1988.
58. A.P.R. Eberle, G.M. Velez, D.G. Baird, P. Wapperom, Fiber orientation kinetics of a concentrated short glass fiber suspension in startup of simple shear flow. Journal of Non-Newtonian Fluid Mechanics, 165 (3), 110-119, 2010.
59. A.P. Arlov, O.L Forgacs, S.G. Mason, Particle motions in sheared suspensions 4. General behavior of wood pulp fibers. Svensk Papperstidn, 61, 61-67, 1958.
60. D.H. Chung, T.H. Kwon, Improved model of orthotropic closure approximation for flow induced fiber orientation. Polymer Composites, 22(5), 636-649, 1999.
61. S.G. Advani, C.L. Tucker, Closure approximations for three-dimensional structure tensors. Journal of Rheology, 34(3), 367-386, 1990.
62. F.P. Folgar, C.L. Tucker III, Orientation behavior of fibers in concentrated suspensions. Journal of Reinforced Plastic Composites, 3, 98-119, 1984.
63. Bay, R. S. Fiber orientation in injection molded composites: A comparison of theory and experiment. Ph. D., University of Illinois Urbana-Champaign, 1991.
64. N. Phan-Thien, X.-J. Fan, R.I. Tanner, R. Zheng, Folgar-Tucker constant for fiber suspension in a Newtonian fluid. Journal of Non-Newtonian Fluid Mechanics. 103, 251-260, 2002.
65. U. Strautins, A. Latz, Flow-driven orientation dynamics of semiflexible fiber systems. Rheologica Acta, 46 (1057-1064, 2007.
66. G. Ausias, J.F. Agassant, M. Vincent, P.G. Lafleur, P.A. Lavoie, P.J. Carreau, Rheology of short glass fiber reinforced polypropylene, Journal of Rheology, 36(4), 525-542, 1992.
67. J.D. Goddard, Y.-H. Huang, On the motion of flexible threads in a Stokes shear field. Journal of Non-Newtonian Fluid Mechanics
68. J.D. Goddard, Tensile behavior of power-law fluids containing oriented slender fibers. Journal of Rheology 22, 615-622, 1978.
69. S.M. Dinh, R.C. Armstrong, A rheological equation of state for semiconcentrated fiber suspensions. Journal of Rheology, 28, 207-227, 1984.
70. E.S.G. Shaqfeh, G.H. Fredrickson, The hydrodynamic stress in a suspension of rods. Physics of Fluids A, 2, 7-24, 1990.
71. D.H. Chung, T.H. Kwon, Fiber orientation in the processing of polymer composites. Korean-Australian Rheology Journal, 14(4), 175-188, 2002.
72. J.L. Ericksen, Transversely isotropic fluids, Kolloid Zeitschrift, 173, 117-122, 1960.
73. G.L. Hand, A theory of anisotropic fluids. Journal of Fluid Mechanics, 13, 33-46,

1962.
74. M.B. Mackaplow, E.S.G. Shaqfeh, A numerical study of the rheological properties of suspensions of rigid, non-Brownian fibers. Journal of Non-Newtonian Fluid Mechanics, 329, 155-186, 1996.
75. G.K. Batchelor, The stress system in a suspension of force-free particles. Journal of Fluid Mechanics, 41, 545-570, 1970.
76. Y. Yamane, Y. Kaneda, M. Doi, Numerical simulation of semi-dilute suspensions of rodlike particles in shear flow. Journal of Non-Newtonian Fluid Mechanics, 54, 405-421, 1994.
77. X.J. Fan, N. Phan-Thien, R. Zheng, A direct simulation of fibre suspensions. Journal of Non-Newtonian Fluid Mechanics, 74, 113-135, 1998.
78. I.L. Claeys, J.F. Brady, Suspensions of prolate spheroids in Stokes flow. Part 1. Dynamics of a finite number of particles in an unbounded fluid. Journal of Fluid Mechanics, 251, 411–442, 1993a.
79. I.L. Claeys, J.F. Brady, Suspensions of prolate spheroids in Stokes flow. Part 2. Statistically homogeneous dispersions. Journal of Fluid Mechanics, 251, 443–477, 1993b.
80. G.G. Lipscomb, M.M. Denn, D.U. Hur, D.V.Boger, The flow of fiber suspensions in complex geometries. Journal of Non-Newtonian Fluid Mechanics, 26, 197-325, 1988.
81. M. Rahnama, D.L. Koch, E.S.G Shaqfeh, The effect of hydrodynamic interactions on the orientation distribution in a fiber suspension subject to simple shear flow. Physics of Fluids, 7(3), 487-506, 1995.
82. Y. Yamane, Y. Kaneda, M. Doi, Numerical simulation of semi-dilute suspensions of rodlike particles in shear flow. Journal of Non-Newtonian Fluid Mechanics, 54, 405-421, 1994.
83. E.J. Hinch, L.G. Leal, The effect of Brownian motion on the rheological properties of a suspension of non-spherical particles. Journal of Fluid Mechanics, 52, 683-712, 1972.
84. S. Yamamoto, T. Matsuoka, A method for dynamic simulation of rigid and flexible fiber in a flow field. Journal of Chemistry Physics, 98, 644-650, 1993.
85. S. Yamamoto, T. Matsuoka, Viscosity of dilute suspension of rodlike particles: a numerical simulation method. Journal of Chemical Physics, 100, 3317-3324, 1994.
86. R. Ross, D. Klingenberg, Dynamic simulation of flexible fibers composed of linked rigid bodies. 106(7), 2949-2960, 1997.
87. C. Schmid, L. Switzer, D. Klingenberg, Simulations of fiber flocculation: Effects of fiber properties and interfiber friction. Society of Rheology, 44(4), 781- 809, 2000.
88. B. Chen, D. Tatsumi, T. Matsumoto, Floc structure and flow properties of pulp fiber suspensions. Journal of Rheology, 30, 19-25, 2002.
89. G.B. Jeffery, The motion of ellipsoidal particles immersed in a viscous fluid. Proceedings of the Royal Society A, 102, 161-179, 1922.
90. P.J. Carreau, Rheological equations from molecular network theories. Transaction of the Society of Rheology, 16, 99-127, 1972.

Chapter 3

Transient Shear Flow Behavior of Concentrated Long Glass Fiber Suspensions in a Sliding Plate Rheometer

Preface

This chapter discusses the validation and use of a sliding plate rheometer to measure the transient rheology of long glass fiber reinforced polypropylene, with 3 different initial fiber orientations. Additionally, it reports initial and final orientation measurements for all samples explored. This chapter is organized as a manuscript for publication.

Transient Shear Flow Behavior of Concentrated Long Glass Fiber Suspensions in a Sliding Plate Rheometer

Kevin C. Ortman, Neeraj Agarwal, Aaron P.R. Eberle, Donald G. Baird
Chemical Engineering Department, Virginia Tech, Blacksburg, VA 24061

Peter Wapperom
Mathematics Department, Virginia Tech, Blacksburg, VA 24061

A. Jeffrey Giacomin
Rheology Research Center and Mechanical Engineering Department, University of Wisconsin, Madison, WI 53706

3.1 Abstract

In order to eventually predict the behavior of long fiber suspensions in complex flows commonly found in processing operations, it is necessary to understand their rheology and its connection to the evolution of fiber orientation and configuration in well defined flows. In this paper we report the transient behavior at the startup of shear flow of a polymer melt containing long glass fibers with a length (L) > 1 mm, using a sliding plate rheometer (SPR). The operation of the SPR was confirmed by comparing the transient shear viscosity (η^+) for a polymer melt and a melt containing short glass fibers (L < 1 mm) with measurements obtained from a cone-and-plate device, using a modified sample geometry that was designed to avoid wall effects. For the long fiber systems, measurements could only be obtained in the SPR because these systems would not stay within the gap of the rotational rheometer. Transient stress growth behavior of the long fiber systems was obtained as a function of shear rate and fiber concentration for samples prepared with three different initial orientations. Results showed that, unlike short fiber systems (with a random planar initial orientation) that usually exhibit a single overshoot peak followed by a steady state, η^+ of the long fiber suspensions often passed through multiple transient regions, depending on the fiber concentration and applied shear rate. Additionally, η^+ of the long fiber suspensions was found to be highly dependent on the initial orientation of the sheared samples. Finally, the initial and final fiber orientations of the long glass fiber samples were measured and used to initiate an explanation of the viscosity behavior. The results obtained in this research will be useful for future assessment of a quantitative correlation between transient rheology and the evolution of fiber orientation.

3.2 Introduction

Fiber reinforced composites are presently of great interest due to their mechanical properties and broad application. Today, many applications utilize the advantages of concentrated long glass fibers, but a fundamental understanding of these fluids is needed to optimize processing conditions for final part properties. Because the final properties of

glass fiber composites are highly dependent on their resulting microstructure, a link between the processing conditions of long fiber composites and their resulting microstructure is needed. Studying the rheology of long fibers can ultimately aid in creating this link.

The term "long fiber" is used in this context to describe fibers that are able to bend or flex during processing, and thus may affect both the material's properties and microstructure. Subsequently, the term "flexibility" will be used to describe the fiber's ability to bend in the presence of flow. Specifically, a fiber exhibiting a larger degree of flexibility is easier to bend within a specified flow field. Switzer and Klingenberg [1] quantified the effective flexibility (f^{eff}) of a fiber in a viscous medium by proposing a dimensionless group that contains both the viscous stress of the matrix, the aspect ratio (a_r) of the fiber, and the Young's modulus (E_Y) of the fiber,

$$f^{eff} \equiv \frac{64\eta_m \dot{\gamma} a_r^4}{E_Y \pi} \tag{3.1}$$

In Eq. 3.1, η_m is the matrix viscosity, $\dot{\gamma}$ is the shear rate, and a_r is defined to be the length of the fiber divided by the diameter (D) of the fiber, $a_r = L/D$. From this expression, the flexibility of a fiber can be seen to increase with aspect ratio for a given material (fixed Young's modulus). In the literature [2], glass fibers less than 1 mm in length are considered to be "short" (and hence rigid) while fibers of length greater than 1 mm are considered to be "long" (and hence flexible).

The rheology of long fiber suspensions is quite complex because of various factors such as fiber-matrix interaction, fiber-fiber interaction, fiber migration, and fiber breakage during processing [3]. These factors become more prominent in high concentration regimes, where the volume fraction of fibers (ϕ) is $\phi \geq a_r^{-1}$. This is because, with increased concentration, there exists an increased probability of encountering short range hydrodynamic forces, frictional, and other mechanical interactions between the fibers [4]. These complexities, along with interactions of the fibers with the walls of the rheometer and their inability to follow the curvilinear streamlines in conventional rotational devices, make the study of the transient rheological properties of concentrated long fiber suspensions more challenging.

As alluded to above, fiber flexibility is a characteristic that plays an important role in determining the rheological behavior of long fiber composites. The length of the glass fibers used within these composites allows them to be considered flexible. Unlike short fibers, long fibers have the ability to change curvature under flow deformations. The flexibility of a fiber varies with the intrinsic properties of the fiber and the strength of the flow field, Eq. 3.1. If the fibers are flexible enough, bending forces acting on the fibers (such as ones resulting from the flow field) can influence the orientation state of the fibers, and in turn can influence the macroscopic properties of the suspension [5]. As a result, fiber flexibility has been shown to have considerable effect on the steady suspension viscosity [6-8].

Due to the complex nature of long fiber composites and the difficulties that are encountered during their rheological characterization, there exists only a limited literature devoted to the experimental study of their rheology. Forgacs and Mason [9] investigated the role of fiber length on the rotational period of fibers in dilute fiber suspensions. They

found that as the apparent aspect ratio decreased (due to fiber bending), the period of rotation was shortened. Tchen [10] showed that curvature greatly influences the drag force on the fibers, while moving in a viscous medium.

Many experimental results have emphasized the role of flexibility on the steady state suspension viscosity. Nawab and Mason [11], in their study of thread-like particles in castor oil, found the rheological behavior of their suspensions to become more complex (i.e. presence of Weissenberg effect, increased sensitivity to shear rate) with increased fiber length. They suspected this behavior was due to the elastic deformation and bending of fibers. Additionally, Blakeney [12] showed that even a 'slight curvature' of fibers has a pronounced effect on the viscosity. Also, Kitano et al. [13,14] and Goto et al. [15] showed that fibers with increased flexibility had a more pronounced effect on the suspension viscosity.

Becraft and Metzner [16] concentrated their efforts on the effect of volume fraction on suspension rheology. They showed a significant increase in viscosity with increased fiber loading at low shear rates, but only a small increase in viscosity at high shear rates. Thomasset et al. [17], in a similar study of polypropylene based long fiber suspensions, observed an increase in shear viscosity with increased fiber content and fiber length, but this viscosity rise was relatively small. Fiber breakage, however, could not be ruled out as a reason for only small enhancements. Additionally, non-Newtonian fluid characteristics such as shear thinning were observed.

In a recent study, Keshtkar et al. [18] investigated the effect of two fiber flexibility parameters, Young's modulus and aspect ratio, in both the semi-dilute and semi-concentrated regimes using a parallel plate rheometer. They found a significant increase in the steady state shear viscosity (η) and primary normal stress difference function (N_1) of the semi-concentrated regime as compared to the semi-dilute regime, where N_1 is defined as

$$N_1 = \sigma_{11} - \sigma_{22} \tag{3.2}$$

and σ_{ij} are components of the total stress tensor. They also found that the effects of aspect ratio and Young's modulus on the flexibility of the fibers are different in each concentration regime. Specifically, they found that in the semi-concentrated regime the effect of aspect ratio is more dominant than the modulus. This was attributed to significant long range hydrodynamic forces. In the concentrated regime, the opposite was found, indicating that fiber-fiber interactions dominated. Additionally, Keshtkar et al. [18] were also among the very few authors to measure the transient stress growth behavior of flexible fiber composites. Viscosity measurements were reported to increase considerably with fiber flexibility. They also found that the duration and magnitude of the stress overshoot increased with increasing fiber flexibility. Although they did not measure orientation in this publication, they attributed this behavior to the notion that increased flexibility may hinder flow induced alignment [18]. In a later paper, however, Keshtkar et al. [19] performed orientation visualization experiments with their materials to quantify the transient orientation, and compared these measurements against predictions using the GENERIC framework. Predictions were observed to be qualitatively good, but it has been suggested that experimental concerns exist when studying fiber systems with parallel plate rheometers [20].

Traditionally, capillary and rotational rheometers have been used to characterize the rheological behavior of concentrated fiber composites. However, certain limitations associated with these rheometers may make them undesirable to perform rheological measurements on fiber suspensions. Rotational rheometers that are generally used at low shear rates employ two geometries: cone-and-plate and parallel disk. For the case of a parallel disk rheometer (PDR), the shear rate varies from the center to the outer boundary and results in an inhomogeneous shear field. Because the rate of rotation of fibers depends on shear rate, it was surmised that such a flow field could result in increased fiber-fiber interaction and thus give rise to enhanced transient rheological measurements [20]. Conversely, the cone-and-plate rheometer (CPR) provides a homogeneous shear field, but the gap between the cone-and-plate varies from center to the outer edge. In the region of small gap, the boundary effects can disrupt the transient stress measurements [3,19,20,21]. While studying short glass fibers with an average length of 0.4 mm, Eberle et al. [20] found reliable stress growth behavior in a CPR was obtained by using a test sample in which the center was bored out. This modification maintained a gap greater than what was found to affect rheology measurements in the PDR.

Capillary rheometers are mostly used to investigate the deformation behavior of long fiber filled suspensions at very high shear rates that are out of reach of rotational devices, but they also present certain limitations. Studies have shown that in laminar flows, migration of fibers may occur across the streamlines and away from the capillary wall [13,22]. This can reduce the fiber concentration at the boundaries of the capillary resulting in a stress response similar to the pure matrix. Additionally, there is considerable fiber breakage that occurs during the extrusion of fibers through the capillary [16,17]. Presently, there is no way to account for the effects of fiber migration and fiber breakage within the rheological results. Finally, these devices cannot be used to track the evolution of fiber orientation at the startup of shear flow.

Few attempts have been made to overcome some of the problems encountered with conventional rheometers. Jones and Roberts [23] utilized a linear oscillator to perform an investigation of the dynamic behavior of an aligned continuous fiber suspension. They measured both longitudinal as well as transverse viscosity of unidirectional fiber suspensions. Shuler and Advani [24] developed an approach to utilize squeeze flow in order to more accurately resemble the real processing of composite sheet laminates. In another investigation, Laun [25] utilized a sandwich rheometer to obtain creep curves on fiber filled low density polyethylene (LDPE) having different initial fiber orientation. Ericsson et al. [26] employed a similar device called a sliding plate rheometer (SPR) incorporating a shear stress transducer (SST) to characterize the steady shear response of a concentrated fiber suspension with planar orientation. This rheometer seemed to overcome the limitations posed by capillary and rotational rheometers. Unlike conventional rheometers, localized measurements are obtained in the SPR and can eliminate typical problems arising from edge effects, oxidative degradation, and sample size [26]. Moreover, homogeneous rectilinear flow field and sufficient gap aid in removing undesirable fiber-fiber and fiber-wall interactions found in most rotational rheometers. Additionally, this rheometer more easily accommodates samples with different initial orientations than rotational geometries.

A sliding plate rheometer, incorporating a wall shear stress transducer, was first developed by Dealy and Giacomin et al. [27-29]. In various publications by Dealy et al.

[29-31] it has proven itself as a trustworthy tool to measure rheological properties of polymer melts under various conditions (i.e. high pressure). Given the advantages the SPR has over conventional rotational and capillary rheometers, it is believed that the SPR has the potential to perform unbiased transient shear experiments on concentrated long glass fiber composites and may also be used to study the evolution of fiber orientation at the startup of shear flow.

The goal of this work is to assess the ability of the SPR to provide transient rheological behavior of both short and long glass fiber suspensions. In particular, the first goal is to show that consistent transient shear stress growth measurements can be obtained for short glass fiber suspensions. Furthermore, the SPR will be used to assess the limitations of obtaining transient stress growth behavior in rotational rheometers such as the parallel disk geometry. The second goal is to determine the effects of fiber concentration, shear rate, and the initial fiber orientation on the transient stress growth behavior of long fiber suspensions in the startup of shear flow. In this work, the suspending medium is an industry supplied polypropylene whose characterization will be reported. The results obtained in this research will be useful for future assessment of a quantitative correlation between transient rheology and the evolution of fiber orientation and used to also assess rheological models connecting the stress with fiber orientation evolution.

3.3 Experimental

3.3.1 Materials

Two different fiber filled systems were used during this study. First, a 30 wt.% chopped short glass fiber (SGF) filled polypropylene (SGF-30), provided by the RTP Company under the commercial name RTP-105, was used to examine the performance of the sliding plate rheometer. SGF-30 material was processed by passing it through a Killion extruder at 20 revolutions per minute (RPM). This was done to homogenize the matrix coated glass fiber pellets and to also erase the deformation history of the material. The extruded strands were cut into pellets (pelletized) and were then compression molded in an appropriate mold (i.e. either a rectangular or a cone-shaped sample) for rheological testing. More details about sample preparation are given in Section 3.3.2. To characterize the fiber length of the glass fibers, pyrolysis was performed on the extrudate at 500^{o}C to extract the fibers from the matrix. An image analysis code was written to determine the number average (L_N) and weight average length (L_W) of approximately 2000 randomly chosen fibers (n_i), as defined in Eq. 3.3 and Eq. 3.4, respectively.

$$L_N = \frac{\sum_i n_i L_i}{\sum_i n_i} \tag{3.3}$$

$$L_W = \frac{\sum_i n_i L_i^2}{\sum_i n_i L_i} \tag{3.4}$$

This method is based on one suggested by Nguyen and co-workers [2]. The L_N and L_W were found to be 0.350 and 0.403 mm, respectively. The average diameter is 12 μm.

The long glass fiber (LGF) reinforced polypropylene material was provided by SABIC Innovative Plastics and had an initial concentration of 30 wt.% (LGF-30). The matrix of this material will be referred to as LGF-M to distinguish it from the polypropylene used in the manufacturing of the SGF samples. The pellets contained bundles of long fibers (13 mm in length) and required dispersion by passing them through the screw of an extruder at 20 RPM. The initial fiber length of 13 mm was reduced significantly during the extrusion process, and it was found via digital imaging that the materials had an L_N and L_W of 3.22 and 4.67 mm, respectively. The average diameter of the fibers is 14.5 μm. The extrudate was collected and pelletized into long strands. The strands were pelletized at lengths that were found to not affect the measured fiber length distribution. Specifically, they were pelletized into lengths of 15 and 76 mm, for reasons that will be discussed in Section 3.3.2. An additional concentration of 10 wt.% fiber (LGF-10) was prepared by mixing the correct amount of long fiber pellets with pure matrix in an extruder at 20 RPM. In all cases, the glass fiber systems used in this research contained a volume fraction of fibers such that the suspensions were classified as concentrated [32].

The effect of the rheometric shearing process on the average fiber length was also investigated. One sample from the highest concentration (30 wt.%) was analyzed after being sheared at the highest shear rate (4.0 s^{-1}) in the SPR. This combination of sample concentration and shear rate was chosen because it is believed to have the most fiber breakage, as compared to any other combination. It was found that the shearing process only slightly affected the number average fiber length, which decreased by less than 10% (L_N = 2.92 mm L_W = 4.10 mm).

3.3.2 Preparation of Samples for Rheological Measurements

For the case of the short fiber suspensions, samples for the CPR having a 50 mm diameter with a 0.1 radian cone angle were compression molded from the extruded pellets to generate samples with a near random planar orientation (as discussed below). Following the procedure of Eberle et al. [20], the samples for the CPR were modified by boring a hole through their center to form cone-and-"donut" (CDR) shaped rheometer samples. The purpose of this was to eliminate boundary effects that are known to exist in CPR devices when the gap is too small near the center.

Long glass fiber samples, having different initial fiber orientations, were prepared from the pellets generated in Section 3.3.1. These samples were initially oriented either in the flow direction (1 direction), the neutral direction (3-direction), or random in the plane (1-3 direction), and will be referred to as D1, D3 and DX samples, respectively, as shown by the coordinate system in Fig. 3.1. The D1 samples were prepared by laying the 76 mm pieces parallel to each other in the flow direction of a 254 mm x 76 mm mold, and then were compression molded at 180°C for 15 minutes. Rheological tests were performed on the neat matrix to verify its integrity after being heated for this length of time, and no signs of degradation were observed. Similarly, D3 samples were prepared by laying 76 mm pieces of the strands in the neutral direction of the mold. The samples having fibers oriented randomly in the 1-3 plane (DX) were fabricated by randomly

distributing the 15 mm pieces of the extruded strands in the mold and then compression molding them. Two different lengths of extruded strands (76 mm and 15 mm) were used to achieve the intended initial orientations more accurately. Specifically, the DX samples required a smaller length strand to achieve better homogeneity and random orientation. All the samples prepared had final dimensions of 254 mm x 76 mm x 1.70 mm. However, the thickness varied between 1.65 mm to 1.85 mm.

3.3.3 Measurement of Initial and Final Fiber Orientations

Both the initial and final fiber orientations of the sheared samples were measured using a micrographic technique proposed by Hine et al. [33]. Using this method, a sample is cut in a plane of interest and carefully polished to expose the elliptical cross-sections of the intersecting fibers within the polymer sample. Short fibers remain rigid and possess an orientation that can be described as a vector that is parallel to the fiber, usually denoted as $\boldsymbol{u}$. For a given orientation distribution function ψ, the second moment of ψ may be evaluated in the following way to form an orientation tensor ($\boldsymbol{A}$) [34],

$$\boldsymbol{A}(t) = \int \boldsymbol{uu}\psi(\boldsymbol{u},t)d\boldsymbol{u} \tag{3.5}$$

The orientation tensor provides a comparatively convenient means of describing the orientation of a population of fibers. Physically, if the fibers are all oriented in the 1-direction (i.e. the flow direction), the orientation tensor will have an A_{11} component of 1.0, and zero for all other components. Likewise, an initial 3-direction orientation would have an orientation tensor whose A_{33} component is 1.0, and zero for all other components. Consequently, fibers randomly oriented in the 1-3 plane will have components $A_{11} = A_{33} = 0.5$, with zero for all other components. In accordance with the method proposed by Hine et al. [33], the shape of a cross-sectional ellipse of a fiber may be used to determine its orientation vector. Constructing this data for a population of fibers yields an average orientation of the microstructure. For long fibers used in the SPR, which may be flexible, the elliptical cross sections measured (for the time being) are used to determine the local orientation of the fibers within the microtomed plane and does not necessarily depict the orientation of the whole fiber (as it does for rigid fibers). Nevertheless, this method is used initially in an effort to quantify the orientation of the LGF samples both before and after shearing them.

In each case, three samples were cut in the 2-3 plane to inspect fibers in the flow direction. This plane was chosen because it should yield a surface with the highest probability of intersecting fibers. Samples were polished using alumina oxide based polishing grits and slurries. A polished sample length of 3 times the average fiber diameter was imaged using an optical microscope along the full part thickness. Specifically, each sample taken was 10 mm x 1.5 mm. A digital imaging program was written to analyze the cross-sectional ellipses to determine the values of the orientation tensor [35]. Each orientation measurement reported within this research contains the averaged results of three samples. Within each polished sample, at least 1,000 fibers were analyzed over the polished sample dimensions. An average standard deviation of about 4% was found for the orientation data, specifically the A_{11} component.

3.3.4 Rheological Measurements

Transient rheological measurements were performed using two different rheometers: a Rheometrics Mechanical Spectrometer (RMS-800) with cone-and-plate fixtures and a sliding plate rheometer, both at 180°C for the SABIC materials and 185°C for the RTP materials. The results from the RMS-800 were mostly used for comparison purposes to validate the performance of the sliding plate rheometer. A 25 mm cone-and-plate fixture with cone angle of 0.1 radians was used to perform experiments on pure resins. Rheological measurements of SGF-30 were performed on a 50 mm cone-and-plate fixture having an identical cone angle of 0.1 radians, but center bored donut shaped samples, as proposed by Eberle et al. [20], were used to eliminate fiber interactions with the plate walls near the center of the sample where the rheometer gap to fiber length ratio is small. The transient shear viscosity, η^+, was calculated as a function of torque $M(t)$ required to rotate the upper fixture from,

$$\eta^+(t) = \frac{3M(t)}{2\pi\dot{\gamma}}\left(R_o^3 - R_i^3\right)^{-1} \tag{3.6}$$

where, R_o and R_i are the outer and inner radii of the donut sample, respectively.

The sliding plate rheometer used in this work was fabricated based on the design initially developed by Giacomin [27] and later modified by Dealy et al. [28, 29]. Figure 1 shows a schematic diagram of the SST and the assembled SPR (including both the stationary plate and bottom moving plate). The apparatus was encased in a forced convection oven (Russells Technical Products, Model RB-2-340) and was mounted vertically in an electromagnetic drive system, specifically an Instron-4204. The Instron can be programmed to drive the moving plate at a desired speed. Once the plate is set into motion, the melt sample therein is sheared homogeneously. The resulting shear stress is measured using a SST that is flush mounted to the stationary plate. The rigid lever in the SST, suspended by a diaphragm, deflects in response to the applied stress of the moving fluid. It causes the other end of the lever to deflect in the opposite direction. This deflection is measured using a capacitance probe, Capacitec, Model HPT-75G-E-L2-2-B-D. The signals from the probe are amplified in a signal amplifier (Capacitec 4100-SL-BNC Amplifier Card) and then sent to a data acquisition card (National Instruments USB-6008). The device is calibrated to convert and quantify the resulting deflection into a shear stress. The calibration was performed using a fluid of known viscosity [36]. A detailed discussion of the calibration procedure adopted for the constructed device can be found elsewhere [31,36]. The face of the lever that is in contact with the melt has a small gap (0.5 mm) around it that allows the lever to deflect in response to a shear force. As a side effect, small amounts of polymer are able to penetrate into this gap. Dealy and co-workers [29-31] have shown that the gap does not have any significant effect on data measured with the SPR, and the device records the true wall shear stress. To be safe, care was taken to clean the instrumentation before each experiment. Two different diaphragms were constructed with different sensitivities to allow a range of materials to be tested in the SPR. The gap between the stationary and moving plate of the SPR was kept at 1.5 mm and yields a gap to fiber diameter ratio of approximately 100 for all glass systems analyzed. This ratio is above the ratio used for

SGF samples [3,20]. The effect of gap on LGF samples, however, has not yet been determined. Samples were squeezed down to the rheometer gap during the insertion process, and allowed better wall-matrix contact before they were sheared. In all rheological experiments conducted within this research, at least 3 samples were tested per experiment. Reported results are an average of the samples tested and have an average standard deviation < 15% for the LGF-10 samples, and < 20% for the LGF-30 samples. Additionally, each sample's deformed length was measured after shearing and compared to the programmed Instron displacement. In all cases, less than +/-3% discrepancy exists between repeated runs, and this suggests slippage between the sample and plates is negligible.

Lastly, to characterize the neat polymer matrix (LGF-M) a 25-mm parallel disk geometry was used with a gap of 2.0 mm. The steady viscosity η (and dynamic viscosity $|\eta^*|$) and primary normal stress difference function N_1 (Eq. 3.2) were measured for LGF-M as a function of shear rate (and frequency) at 180°C. The matrix characterization of η ($|\eta^*|$) and N_1 for LGF-M is reported in Fig. 3.2.

3.4 Results and Discussion

In the following section both the results obtained and their significance will be discussed. First, the measured initial orientations of the sheared LGF samples will be discussed and used as a reference for the starting state of the rheological samples explored. Second, confirmation of the sliding plate as a method for obtaining the transient response of both short and long fiber suspensions will be presented. The effects of initial fiber orientation, shear rate, and concentration on LGF rheology will be presented. Additionally, in an effort to better understand the relation between the evolution of fiber orientation and rheological properties, the final measured orientation (after shearing) will be compared against the initial measured orientation (prior to shearing).

3.4.1 Initial Fiber Orientation

The initial fiber orientations of the fiber samples were measured using the method described in Section 3.3.3 and the results are presented in Table 3.1 (along with final values, to be discussed later). LGF samples with three different initial orientations were measured for two different concentrations, as described in Section 3.3.1, and one SGF sample was also measured. Essentially, all samples with initial random orientation in the shear plane (DX) have A_{11} and A_{33} values that are close to the theoretical value of 0.5. The two LGF samples prepared with fibers in the flow direction (D1) showed values of A_{11} approaching 1.0 while the values of A_{22} and A_{33} were close to 0.0. Although perfect alignment in the flow direction was not obtained, the results indicate that the fibers have a preferential alignment in the flow direction. Finally, both samples prepared with fiber orientation in the 3-direction (D3) show an A_{33} component close to 1.0. All the samples, both initial orientated and final sheared samples, have a relatively small A_{22} component. This suggests that most fibers stay within the 1-3 plane during the deformation process and do not significantly rise in the 2-direction.

3.4.2 Confirmation of the Sliding Plate Rheometer Usage

To validate the usage of the SPR, a comparison of the viscosity of the neat polypropylene matrix (LGF-M), at the startup of shear flow, using the SPR is made with values obtained using a CPR at shear rates of 0.4, 1.0, and 4.0 s^{-1}. For the LGF-M samples, very good agreement exists between the values obtained by both rheometers, as seen in Fig. 3.3. Additionally, it is seen that the polypropylene matrix reaches a steady state viscosity that ranges between 512-570 Pa*s over the shear rates measured and possesses a shear thinning behavior of about 10% within this range. To confirm the use of the SPR for fiber filled systems, η^+ of a 30 wt.% SGF sample obtained using an SPR is compared to that obtained using a CDR, as shown in Fig. 3.4, for an exemplary shear rate of 1.0 s^{-1}. Each sample's initial fiber orientation, in both the SPR and CDR rheometers, was nearly random in the 1-3 plane (see "SGF30%-DX-Initial" in Table 3.1 and Fig. 3.1 for coordinate reference). The values of η^+ measured in the CDR were obtained using the method proposed by Eberle et al. [20] in which a donut shaped sample (the center of the sample was bored out to eliminate wall effects) was employed. As one can see from Fig. 3.4 the transient response measured in the SPR, in terms of overshoot and time to reach steady state, are in excellent agreement with those obtained using the CDR. This confirms the operation of the SPR for measuring the transient response of fiber suspensions, or at least, suspensions of short fibers.

These results for the short fiber system are of further significance. It has been shown that even when studying SGF systems, special considerations must be taken to obtain unbiased and reproducible rheological results [3,19,20]. Measurements of the transient stresses of SGF systems using a traditional PDR produce transients that are enhanced both in overshoot magnitude and in the time (or strain) to reach steady state (even when gap effects are no longer prevalent) relative to those measured in a homogeneous shear field such as those obtained using a CPR (large diameter) or CDR. This discrepancy within the PDR is believed to be due to the variation in shear rate from the center of the sample to the edge of the sample [20]. The low shear rates in the center of the PDR slow up the evolution of orientation of the fibers in the higher shear rate regions. The results gained here confirm the approach proposed by Eberle et al. [20] in which a modified sample is used in a CPR, and raise questions about the validity of measurements reported by others using a PDR, even when gap effects are eliminated.

To check the reproducibility of these results, the same experiments were performed twice in the SPR and it was found that the results are reproducible within an average error of +/- 5% for the SGF systems. From these results, it is believed that the SPR is capable of producing unbiased and reproducible results for concentrated fiber-filled systems, and its use can be extended to measure LGF systems.

3.4.3 Effects of Initial Orientation

As stated before, the goal of this research is to ultimately determine the relationship between the evolution of long glass fiber orientation and the transient rheology of the suspension. As a first step in determining this relationship, the effect of the initial orientation on the transient shear rheology of LGF systems was studied. Furthermore, the final orientations of the sheared samples were measured to help

qualitatively understand the evolution of fiber orientation at the startup of shear flow. A more precise description of the transient fiber orientation will be the subject of a future publication. Samples containing fibers were molded with three different initial orientation states, as explained in Section 3.3.2. Considering the 10 wt.% LGF samples sheared at a rate of 0.4 s^{-1} in Fig. 3.5, one can note the relative differences in the measured rheology due to the initial orientation. Fig. 3.5 shows that both the DX and D1 samples possess an overshoot and plateau in viscosity. As expected from short fiber theory, an overshoot in viscosity arises as the fiber orientation changes and begins to align in the flow direction [37,38]. The D1 sample has an overshoot magnitude that is, on average, slightly less than its DX counterpart. This behavior is probably because the D1 sample contains fibers whose initial orientation is nearly in the flow direction. The D3 sample, on the other hand, has a very low but broad overshoot. Even though the D3 sample does not seem to show a behavior that is as dynamic as the other initially oriented samples, interestingly the fiber orientation does change with strain. This can be seen by noting that the final A_{11} orientation component of this sample is predominately in the flow direction (Table 3.1) and thus must have evolved from an initial orientation that was primarily in the neutral direction (large A_{33}). The evidence of the broad viscosity overshoot suggests a longer transient time for fiber orientation. Lastly, Table 3.1 shows that the A_{11} orientation component of the D3 sample is slightly less aligned than both the D1 and DX samples at this shear rate, suggesting why the viscosity is slightly elevated in comparison to the other samples (after a strain of 120).

When the 10 wt.% samples are sheared at 1.0 s^{-1}, we see even more dynamic behavior in the rheology, Fig. 3.6. Again, both the D1 and DX samples show a relatively large initial peak in viscosity that then begins to approach steady state, while the D3 sample has a very broad overshoot. Although DX has a larger overshoot, the D1 sample has a viscosity that is always greater than the other samples at this shear rate. This may seem counter intuitive, because the D1 sample is initially orientated closer to the flow direction. Observing the final orientations in Table 3.1, we see that the D1 sample in this case has the largest A_{11} component, indicating good alignment, but also has the largest A_{12} component. This component of the orientation tensor has classically been responsible for part of the extra stress tensor in the stress theory concerning transversely isotropic fluids, such as those containing short fibers [37,38]. Hence, as the A_{12} component becomes larger, so does the shear viscosity of the composite fluid. This, therefore, may explain why the D1 sample has a higher final viscosity. Unfortunately, there is very limited theory that addresses the relationship between the stress response and the orientation tensor of concentrated long fiber suspensions. This link, of course, is of significant importance and needs to be further investigated.

At a shear rate of 4.0 s^{-1}, the D1 sample exhibits a fairly large overshoot and after approximately 60 strain units approaches a steady state viscosity similar to that of the neat matrix, Fig. 3.7. Again, D3 shows a very broad overshoot, inferring a slower transient fiber orientation before the viscosity begins to approach the matrix viscosity. The DX sample goes through a relatively quick overshoot and reaches a plateau, but then begins to later decrease again around 100 strain units. The latent dynamics observed in the DX sample may be because long fibers have the tendency to network and flocculate, as a result of their semi-flexible nature [1,10,18,19,39]. Such phenomena have been reported in the literature [10,40,41], and it has been found that both higher shear rates and

larger strains may have the ability to break up these fiber networks. The initially random sample may be exhibiting the dynamics of the destruction of fiber flocculation after approximately 100 strain units, causing a further decrease in viscosity, and may still be evolving even after 120 strain units. Sample inspection revealed no lack of uniformity or evidence of slippage that would indicate incorrect measurements. Additionally, minimal fiber breakage occurs from the shearing process, as discussed in Section 3.3.1, and all changes in the transient viscosity are believed to be due to orientational/configurational changes of the fibers. From Fig. 3.7, it is seen that the DX sample has the largest viscosity after 120 strain units of shearing. This relatively larger viscosity may be explained by comparing the DX sample's lower A_{11} component and somewhat larger A_{12} component with those of the other two samples.

Identical experiments were conducted with the 30 wt.% materials with all three initial orientations. Similar, but more dramatic trends are visualized, Fig. 3.8. At the 0.4 s^{-1} shear rate, the D3 sample again exhibits a relatively small but broad overshoot. Both the DX and D1 samples show an initial overshoot, followed by a plateau in the viscosity. This initial overshoot, as stated before, is probably due to the orientation process of most of the fibers. Interestingly, however, the D1 sample begins to decrease from its plateau around 100 strain units and may suggest the viscosity plateaus at this concentration are due to fiber interlocking mechanisms that have the ability to temporally enhance the viscosity. It is also apparent that this D1 sample may still be evolving even after 120 strain units. Much more detailed orientation information (as a function of strain) is needed to confirm this and to link the measured rheology with the transient evolution of the fiber orientation. Additionally, the DX sample maintains a higher viscosity relative to that of the D1 sample throughout the experiment. The final orientation measurements (Table 3.1) agree with this and suggest that the D1 sample is the sample whose fibers are most aligned in the flow direction, followed by a slight decrease in alignment in the DX sample. The D3 sample has the least amount of final alignment with an A_{11} component of only 0.67.

At a shear rate of 1.0 s^{-1}, the same trends occur, but the initial peaks are becoming much more defined, Fig. 3.9. At this shear rate and concentration, it is clear that the DX and D1 samples are exhibiting an overshoot, followed by a plateau. Unlike the DX sample, however, the D1 sample is again able to descend from its initial plateau, this time around 80 strain units. Again, it is conceivable that the LGF samples may be exhibiting fiber networking mechanisms that are more easily broken at higher shear rates, thus causing the plateau edge to shorten and shift to lower strain units. Orientation measurements again suggest that the D1 sample exhibits the greatest final alignment and may provide reasoning as to why its final viscosity is the lowest of the samples depicted in Fig. 3.9.

Finally, at the highest shear rate, all samples exhibit three regions of interest, Fig. 3.10. The viscosity growth shows a peak followed by a plateau and then a descent. The D1 samples are able to reach their steady state viscosity most rapidly. In this case, it readily approaches the matrix viscosity at this applied shear rate. The DX sample and the D3 sample now have similar profiles, but the DX sample viscosity values are primarily below those of the D3 sample's values. This is most likely because the DX sample's initial orientation is more aligned in the flow direction than compared to its D3 counterpart. This data also suggests that the microstructure of the DX and D3 samples

are still evolving after 120 strain units and have not yet reached steady state. Unfortunately, the final orientation measurements do not suggest an answer that fully supports this description. Although the final viscosity measurements (after 120 strain units) of the DX and D3 samples are very similar, orientation measurements at this strain magnitude show the D1 sample is actually closer in final orientation to that of the D3 sample. In fact, the orientation measurements suggest that the fibers in the DX sample are most aligned in the flow direction, despite the large differences in final viscosity (especially between D1 and DX). This result may suggest that a fiber's entire configuration (i.e. those accounting for fiber curvature), as opposed to the measured "local" orientations supplied in Table 3.1, may be a large contributing factor to fully understanding LGF systems and the rheological link to their microstructure.

3.4.4 Effects of Shear Rate

The effect of shear rate on the transient shear rheology of LGF systems is analyzed in this section. The most notable consequence of increasing the shear rate is in the shear thinning behavior of these systems. This is observed in almost all the data, and for an exemplary case is shown in Fig. 3.11. For the case of the 10 wt.% DX samples it is seen that the initial overshoot magnitude decreases with increasing shear rate and, although not directly shown here, is also true for the 30 wt.% samples (see Figs. 8-10). Interestingly, within both concentrations there is a plateau in the viscosity of the DX samples sheared at 4.0 s^{-1} that seems to descend around 100 strain units. This behavior, as discussed in Section 3.4.3, may be due to fiber flocculation and is even more apparent in the 30 wt.% D1 samples. As the shear rate increases, the plateaus of the 30 wt.% D1 samples shift to the left and shorten. For most of the 10 wt.% samples, however, with the possible exception of the DX sample at 4.0 s^{-1}, these plateaus are not seen and are instead believed to be at steady state. For the case of the D1 samples (both 10 wt.% and 30 wt.%), as shear rate is increased the systems are able to approach values near the matrix viscosity. Finally, the samples initially oriented in D3 (both 10 wt.% and 30 wt.%) show more dynamic viscosity behavior as the shear rate is increased for both concentrations. As shear rate increases, more shear thinning occurs and, for the case of the 30 wt.% D3 sample at a shear rate of 4.0 s^{-1}, a just noticeable plateau descent is visible in the viscosity at 100 strain units. Again, this plateau may be due to the complex behavior of flexible fibers that are able to highly interact. Furthermore, these interactions may occur in ways that current theory cannot yet quantify.

The effect of shear rate on the final orientation of the fibers is unclear. From Table 3.1, we see that for the case of the 10 wt.% samples, the magnitude of the A_{11} component generally increases between 0.4 s^{-1} and 4.0 s^{-1} samples, but in all cases experiences a slight decrease in orientation in the intermediate shear rate, 1.0 s^{-1}. This is believed to be a consequence of fiber-fiber interactions and bending mechanisms that may be dependent on shear rate. An additional comment is needed for 10 wt.% D1 samples. It is apparent from Table 3.1 that the final A_{11} orientation component for all 10 wt.% D1 samples is less than its initial value. This is most likely due to fiber-fiber interactions and has been theoretically accounted for in short fiber orientation theory via dissipation terms such as rotary diffusion [42]. For the 30 wt.% samples, the final orientation values stay more consistent regardless of shear rate, with the exception of the

samples with an initial D3 orientation. In these samples, an orientation difference of approximately 0.10 exists in the in A_{11} between the low shear rate and the two higher shear rates. The 30 wt.% DX samples show an increase in orientation with shear rate but differ only slightly.

3.4.5 Effects of Concentration

Previous work on long fiber suspensions has shown that increasing the fiber concentration increases the shear viscosity of the suspension [13,16,17,18,26,43]. An increase in viscosity with increase in concentration can be observed in these experiments as well. Koch and coworkers [44,45] attributed this behavior to increased fiber-fiber interactions. They suggested that at high concentrations, the fiber collision frequency is expected to increase significantly and may give rise to mechanical contacts that contribute to the enhanced stress. Large viscosity overshoots were observed in this research for the DX and D1 samples and is the result of both fiber orientation and fiber-fiber interactions. Both the magnitude and the width of the overshoot generally increased with higher fiber loading. This indicates that as fiber concentration is increased, and therefore the frequency of fiber contacts is increased, the ability for fibers to orient in the flow direction becomes more inhibited. However, once the fibers become more aligned, the resistance to the fluid flow decreases, thus causing an overshoot in stress. We believe that some of the larger overshoots observed within the higher concentrations, especially those exhibiting viscosity plateaus, may be a result of increased fiber networking or flocculation, as has been postulated in literature [1,10,18,19,40]. As a result, it can be concluded that the mechanical contacts between fibers play a major role in determining the dynamics of fiber evolution in concentrated suspensions. Lastly, a comment about the effect of concentration on the final orientation will be made. With the exception of the D3 samples, the final magnitudes of the A_{11} orientation components are either similar or higher for the 30 wt.% samples (as compared with the 10 wt.% samples) which may suggest some form of ordering potential (clustering effect) may also exist within more highly concentrated systems [32]. Visual inspection of polished micrographs, although not produced here, may also supply evidence for the existence of this phenomenon.

3.5 Conclusions

In this work, a sliding plate rheometer was shown to be a viable means of obtaining the transient viscosity at the startup of shear flow for concentrated short and long glass fiber suspensions. Additionally, the sliding plate rheometer was shown to confirm the short glass fiber results obtained by Eberle et al. [20], who suggested that the inhomogeneous shear field generated in a conventional parallel disk rheometer may lead to enhanced stress transients, both in terms of the magnitude of the overshoot and the time to reach steady state. Using the sliding plate rheometer, the transient rheology at the startup of shear flow was measured for concentrated long glass fiber suspensions with different initial orientations. It was shown that the initial fiber orientation and concentration greatly affect the rheological behavior. Specifically, results showed that, unlike short fiber systems that usually exhibit a single overshoot peak followed by steady state, η^+ of the long fiber suspensions often passed through multiple transient regions,

depending on the fiber concentration and applied shear rate. Reasons for this behavior were suggested to be a consequence of strong fiber-fiber interactions, the semi-flexible nature of the fibers, and possibly due in part to fiber interlocking and flocculation. All long fiber systems studied showed shear thinning over the range of shear rates used, and an increase in concentration was shown to increase the viscosity. Finally, fiber orientation measurements were made for each sample, both prior to and after shearing, and were used to help qualitatively relate the measured rheology to the transition in fiber orientation. This work will be of further use for the future assessment of a quantitative correlation between the transient rheology and the transient evolution of fiber orientation, wherein long fiber orientation and configuration will be tracked with strain.

3.6 Acknowledgments

The financial support for this work, from the National Science Foundation through Grant No. CMMI-0853537, is greatly appreciated. We would also like to thank RTP and SABIC for providing the materials used in this work. Additional gratitude is given to the Materials Science and Engineering department at Virginia Tech for providing polishing and microscopy facilities.

3.7 References

1. L. Switzer III, D.J. Klingenberg, Rheology of sheared flexible fiber suspensions via fiber-level simulations, J. Rheol. 47 (2003) 759-778.
2. B. Nguyen, S. Bapanapalli, J. Holbery, M. Smith, V. Kunc, B. Frame, J. Phelps, C.L. Tucker III, Fiber length and orientation in long-fiber injection-molded thermoplastics-- Part I: modeling of microstructure and elastic properties, J. Thermoplast. Compos. Mater. 42 (2008) 1003-1029.
3. M. Sepehr, G. Ausias, P.J. Carreau, Rheological properties of short fiber filled polypropylene in transient shear flow, J. Non-Newtonian Fluid Mech. 123 (2004) 19-32.
4. R. Guo, J. Azaiez, C. Bellehumeur, Rheology of fiber filled polymer melts: role of fiber-fiber interactions and polymer-fiber coupling, Polym. Eng. Sci. 45 (2005) 385-399.
5. U. Strautins, A. Latz, Flow-drive orientation dynamics of semiflexible fiber systems, Rheol. Acta 46 (2007) 1057-1064.
6. C. Joung, N. Phan-Thien, X. Fan, Direct simulation of flexible fibers, J. Non-Newtonian Fluid Mech. 99 (2001) 1-36.
7. C. Joung, N. Phan-Thien, X. Fan, Viscosity of curved fibers in suspension, J. Non-Newtonian Fluid Mech. 102 (2002) 1-17.
8. S. Bapanapalli, B. Nguyen, Prediction of elastic properties for curved fiber polymer composites, Polym. Compos. 29 (2008) 544-550.
9. O. Forgacs, S. Mason, Particle motions in sheared suspensions IX. Spin and deformation of threadlike particles, J. Colloid Sci. 14 (1959) 457-472.
10. C.-M. Tchen, Motion of small particles in skew shape suspended in a viscous liquid, Appl. Phys. 25 (1954) 463-473.
11. M. Nawab, S. Mason, Viscosity of dilute suspensions of thread-like particles, J.

Phys. Chem. 62, (1958), 1248-1253.
12. W. Blakeney, The viscosity of suspensions of straight, rigid rods. J. Colloid Interface Sci. 22 (1966) 324-330.
13. T. Kitano, T. Kataoka, Y. Nagatsuka, Dynamic flow properties of vinylon fibre and glass fiber reinforced polyethylene melts, Rheol. Acta 23 (1984) 408-416.
14. T. Kitano, T. Kataoka, Y. Nagatsuka, Shear flow rheological properties of vinylon- and glass-fiber reinforced polyethylene melts, Rheol. Acta 23 (1984) 20-30.
15. S. Goto, H. Nagazono, H. Kato, The flow behavior of fiber suspensions in Newtonian fluids and polymer solutions, Rheol. Acta 25 (1986) 119-129.
16. M. Becraft, A. Metzner, The rheology, fiber orientation, and processing behavior of fiber-filled fluids, J. Rheol. 36 (1992) 143-174.
17. J. Thomasset, P.J. Carreau, B. Sanschagrin, G. Ausias, Rheological properties of long glass fiber filled polypropylene, J. Non-Newtonian Fluid Mech. 125 (2005) 25-34.
18. M. Keshtkar, M.C. Heuzey, P.J. Carreau, Rheological behavior of fiber-filled model suspensions: Effect of fiber flexibility, J. Rheol. 53 (2009) 631-650.
19. M. Keshtkar, M.C. Heuzey, P.J. Carreau, M. Rajabian, C. Dubois, Rheological properties and microstructural evolution of semi-flexible fiber suspensions under shear flow, J. Rheol. 54 (2010) 197-222.
20. A.P.R. Eberle, D.G. Baird, P. Wapperom, Fiber orientation kinetics of a concentrated short glass suspension in startup of simple shear flow, J. Non-Newtonian Fluid Mech. 165 (2010) 110-119.
21. R. Powell, Rheology of suspensions of rodlike particles, J. Stat. Phys. 62 (1991) 1073-1094.
22. L. Mondy, A. Geller, D. Rader, M. Ingber, Boundary element method calculations of the mobility of nonspherical particles—II. Branched chains and flakes, J. Aerosol Sci. 27 (1996) 537-546.
23. R.S. Jones, R.W. Roberts, Anisotropic shear flow in continuous fibre composites, Composites Part A 25 (1994) 171-176.
24. S. Shuler, S. Advani, Transverse squeeze flow of concentrated aligned fibers in viscous fluids, J. Non-Newtonian Fluid Mech. 65 (1996) 47-74.
25. H. Laun, Orientation effects and rheology of short glass fiber-reinforced thermoplastics, Colloid. Polym. Sci. 262 (1984) 257-269.
26. K.A. Ericsson, S. Toll, J. Månson, Sliding plate rheometry of planar oriented concentrated fiber suspension, Rheol. Acta 36 (1997) 397-405.
27. A.J. Giacomin, A sliding plate melt rheometer incorporating a shear stress transducer, Ph.D. thesis, Department of Chemical Engineering, McGill University (1987).
28. A.J. Giacomin, T. Samurkas, J.M. Dealy, A novel sliding plate rheometer for molten plastics, Poly. Eng. Sci. 29 (1989) 499-504.
29. J.M. Dealy, S. Soong, A parallel plate melt rheometer incorporating a shear stress transducer, J. Rheol. 28 (1984) 355-365.
30. H. Park, S. Lim, F. Smillo, J.M. Dealy, C. Robertson, Wall slip and spurt flow of polybutadiene, J. Rheol. 52 (2008) 1201-1239.
31. F. Koran, J.M. Dealy, A high pressure sliding plate rheometer for polymer melts, J. Rheol. 43 (1999) 1279-1290.

32. M. Doi, S.F. Edwards, The Theory of Polymer Dynamics, Oxford University Press: New York, 1988.
33. P.J. Hine, N. Davidson, R.A. Duckett, A.R. Clarke, I.M. Ward, Hydrostatically extruded glass–fiber reinforced polyoxymethylene. I. The development of fiber and matrix orientation, Polym. Compos. 17 (1996) 720–729.
34. S.G. Advani, C.L. Tucker III, The use of tensors to describe and predict fiber orientation in short fiber composites, J. Rheol. 31 (1987) 751-784.
35. Y.H. Lee, S.W. Lee, J.R. Youn, Characterization of fiber orientation in short fiber reinforced composites with an image processing technique, Mater. Res. Innovations 6 (2002) 65-72
36. N. Agarwal, Transient shear flow rheology of concentrated long glass fiber suspensions in a sliding plate rheometer, Master's thesis, Department of Chemical Engineering, Virginia Polytechnic Institute and State Univeristy, 2009.
37. S. Dinh, R.C. Armstrong, A rheological equation of state for semiconcentrated fiber suspensions, J. Rheol. 28 (1984) 207-227.
38. E. Shaqfeh, G. Fredrickson, The hydrodynamic stress in a suspension of rods, Phys. Fluids A 2 (1990) 7-24.
39. S. Toll, and J.-A.E. Manson. Elastic compression of a fiber network, J. Appl. Mech. 62 (1995) 223-226.
40. C.F. Schmid, L.H. Switzer, D.J. Klingenberg. Simulations of fiber flocculation: Effects of fiber properties and interfiber friction, J. Rheol. 44 (2000) 781-809.
41. E. Bonano, Study of Flow Breakup and Formation in Flowing Concentrated Fiber Suspensions, Int. J. Multiphase Flow, 10 (2984) 623-633.
42. F.P. Folgar, C.L. Tucker III, Orientation behavior of fibers in concentrated suspensions, J. Rein. Plast. Comp. 3 (1984) 98–119.
43. E. Ganani, R. Powell, Rheological properties of rodlike particles in a Newtonian and a non-Newtonian fluid, J. Rheol. 30 (1986) 995-1013.
44. R. Sundararajakumar, D. Koch, Structure and properties of sheared fiber suspensions with mechanical contacts, J. Non-Newtonian Fluid Mech. 73 (1997) 205-239.
45. M. Chaouche, D. Koch, Rheology of non-Brownian rigid fiber suspensions with adhesive contacts, J. Rheol. 45 (2001) 369-382.

Sample Name	A11	A12	A22	A33	# Fibers Analyzed/Sample
SGF30%-DX-Initial	0.484	0.056	0.048	0.468	4988
LGF10%-DX-Initial	0.565	0.048	0.038	0.397	1372
LGF10%-DX-0.4	0.760	0.040	0.043	0.197	1093
LGF10%-DX-1.0	0.668	0.070	0.067	0.265	1313
LGF10%-DX-4.0	0.733	0.063	0.055	0.212	1249
LGF10%-D1-Initial	0.863	0.025	0.043	0.094	1524
LGF10%-D1-0.4	0.725	0.075	0.086	0.189	1533
LGF10%-D1-1.0	0.697	0.115	0.130	0.173	1316
LGF10%-D1-4.0	0.822	0.047	0.049	0.129	1300
LGF10%-D3-Initial	0.051	0.038	0.050	0.900	1258
LGF10%-D3-0.4	0.708	0.061	0.046	0.245	1369
LGF10%-D3-1.0	0.625	0.057	0.057	0.318	1339
LGF10%-D3-4.0	0.808	0.029	0.025	0.167	1291
LGF30%-DX-Initial	0.609	0.037	0.028	0.363	3843
LGF30%-DX-0.4	0.763	0.101	0.111	0.126	3531
LGF30%-DX-1.0	0.783	0.061	0.059	0.158	4244
LGF30%-DX-4.0	0.817	0.057	0.063	0.120	3951
LGF30%-D1-Initial	0.794	0.068	0.077	0.129	2855
LGF30%-D1-0.4	0.807	0.056	0.066	0.127	3118
LGF30%-D1-1.0	0.805	0.076	0.083	0.112	2503
LGF30%-D1-4.0	0.780	0.072	0.079	0.141	4140
LGF30%-D3-Initial	0.093	0.065	0.080	0.828	3111
LGF30%-D3-0.4	0.666	0.038	0.033	0.300	4139
LGF30%-D3-1.0	0.767	0.033	0.029	0.204	4170
LGF30%-D3-4.0	0.757	0.037	0.037	0.206	3164

Table 3.1: Initial and final measured orientations. All final measurements were taken after 120 strain units. Samples containing the word "Initial" denote initial orientation values (0 strain units). Sample naming is of form: material-initial direction-shear rate s^{-1}.

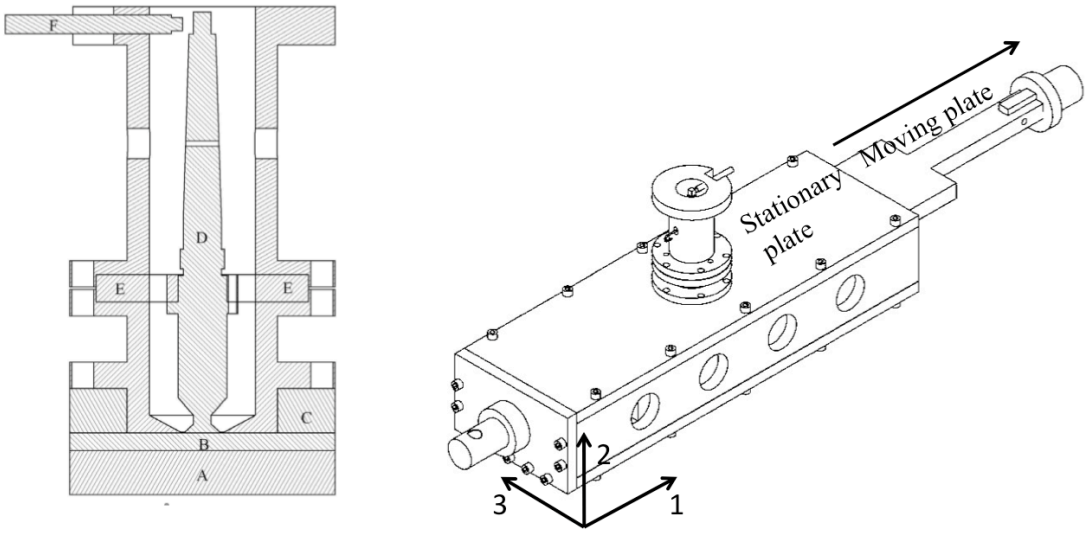

Figure 3.1: Schematics of the sliding plate rheometer from the perspective of the shear stress transducer (Left) and the sliding plate (Right). The left figure shows the moving plate (A), the sample region (B), the stationary plate (C), the transducer lever (D), the diaphragm (E), and the capacitance probe (F). The right figure shows the schematic of the sliding plate and the coordinate system employed.

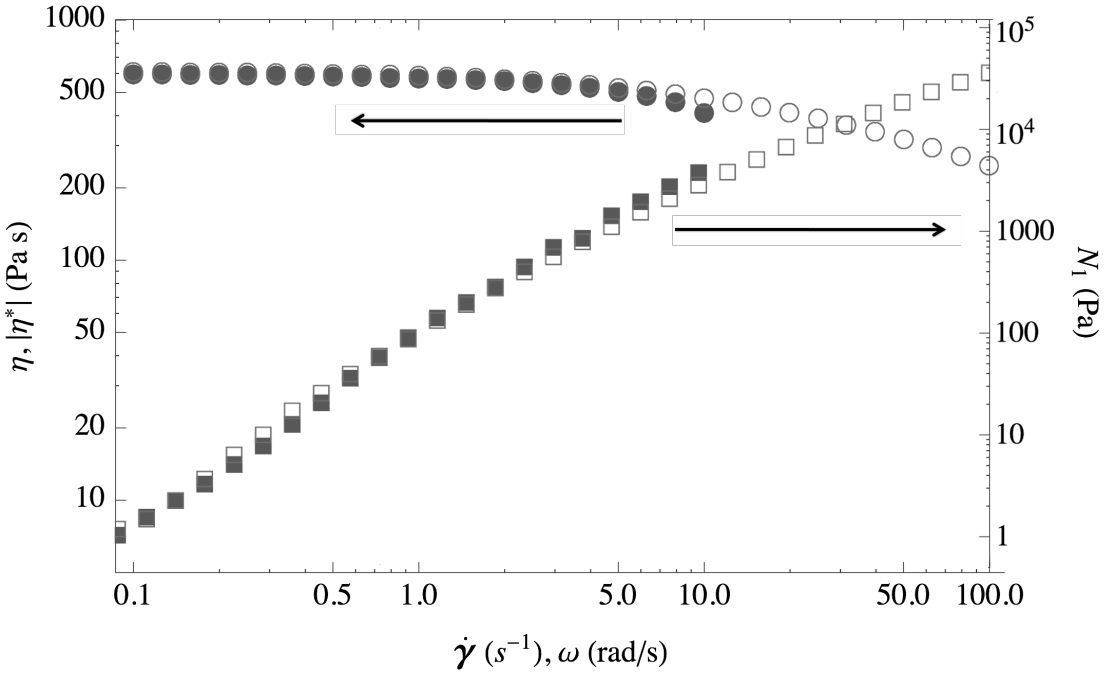

Figure 3.2: Characterization of the matrix LGF-M showing the steady viscosity (●), complex viscosity (○), and first normal stress difference function (■) with Laun's approximation (□) as a function of shear rate (or frequency).

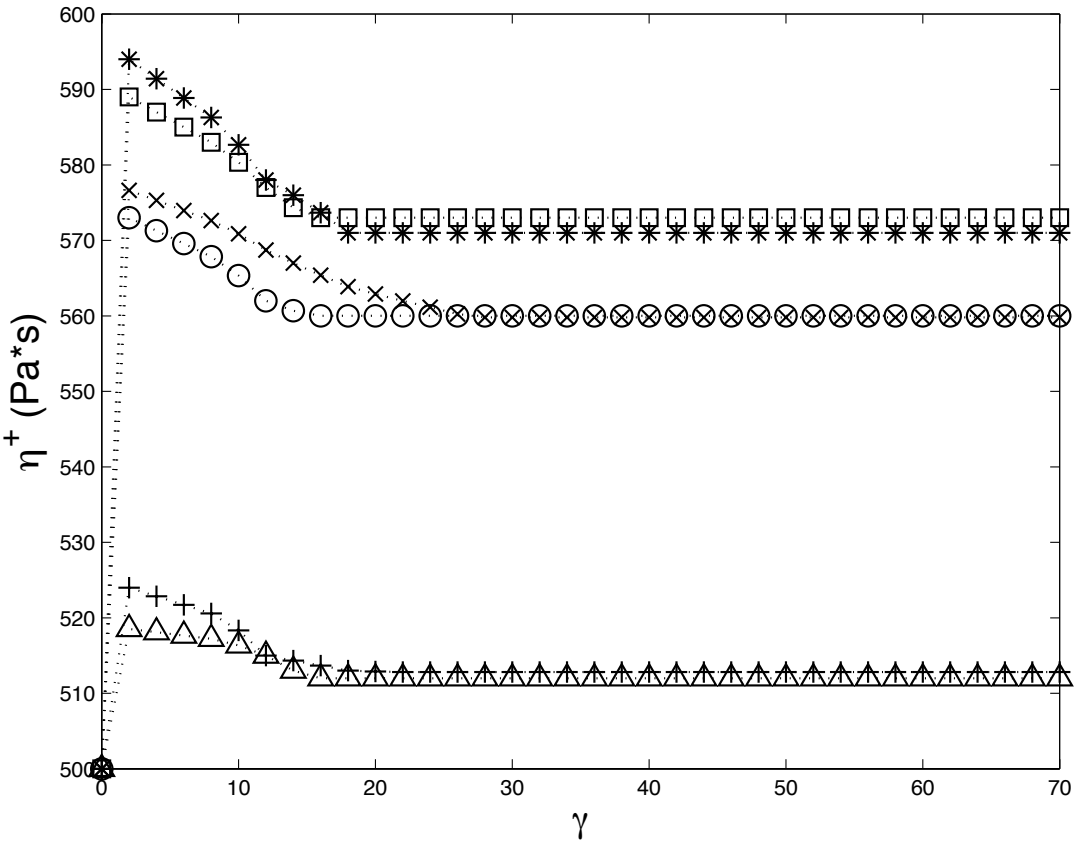

Figure 3.3: Comparison of the transient viscosity at the startup of shear flow measured using the sliding plate rheometer and a cone-and-plate rheometer for the SABIC polypropylene matrix (LGF-M) at shear rates of 0.4, 1.0, and 4.0 s^{-1}. The symbols (□) and (*) denote measurements at 0.4 s^{-1}, the symbols (○) and (x) denote measurements at 1.0 s^{-1}, and the symbols (△) and (+) denote measurements at 4.0 s^{-1} in the SPR and CPR, respectively.

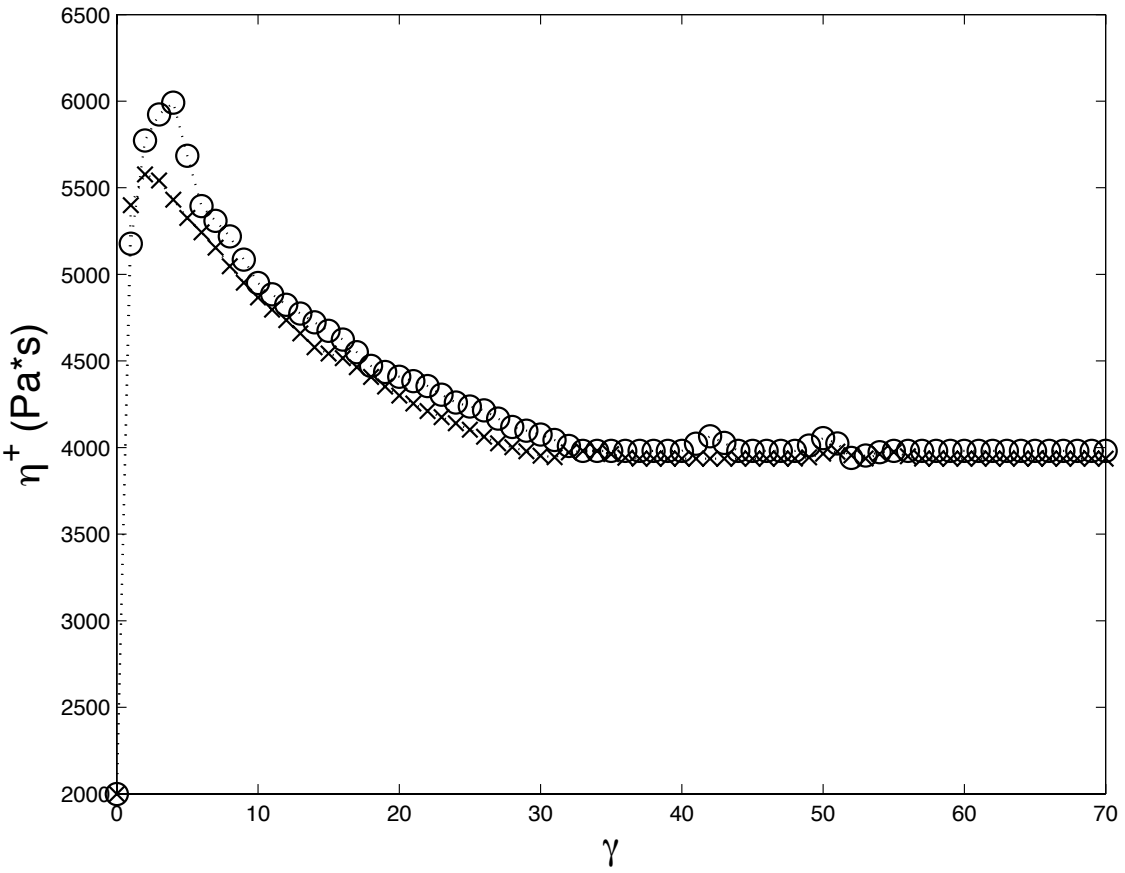

Figure 3.4: Comparison of the transient viscosity at the startup of shear flow using the sliding plate rheometer and a cone-and-disk rheometer for an initially random 30 wt.% RTP short glass fiber system at a shear rate of 1.0 s^{-1}. The symbols (○) and (x) denote the SPR and CDR measurements, respectively.

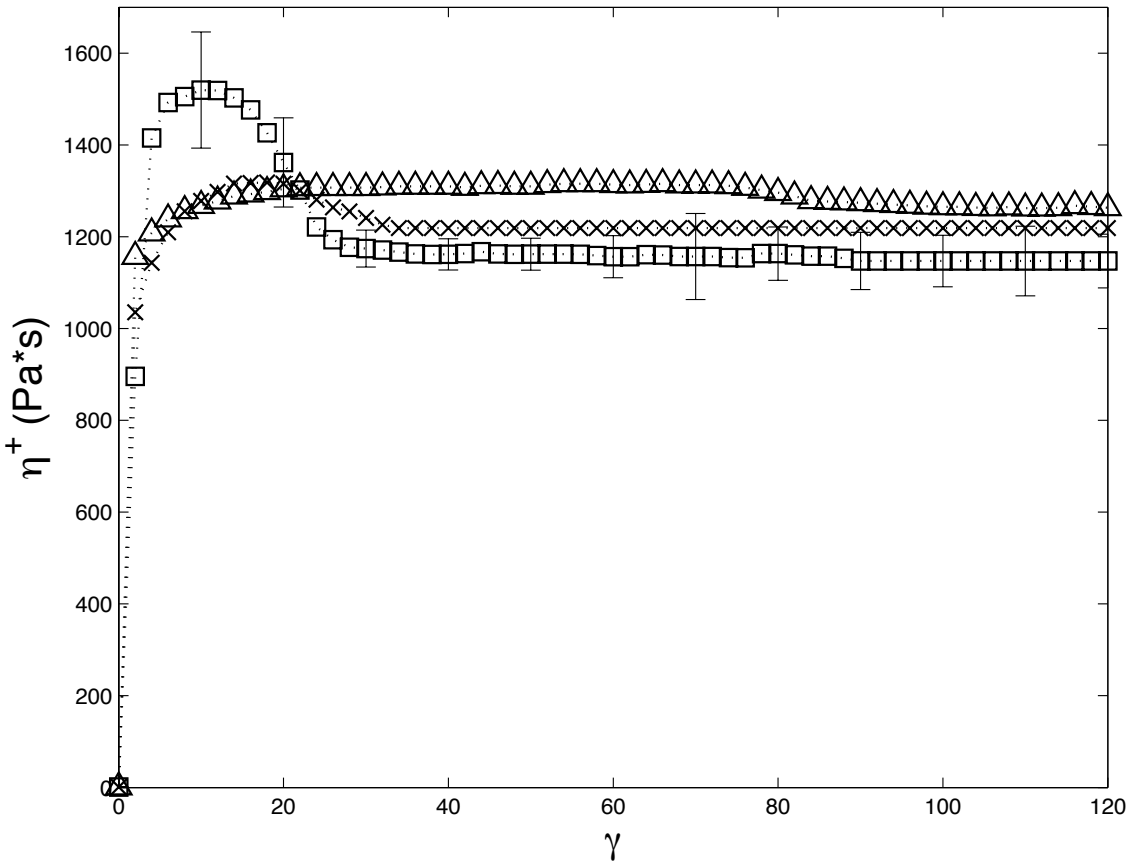

Figure 3.5: Comparison of the effect of initial orientation on the transient viscosity of a 10 wt.% long glass fiber system sheared at 0.4 s^{-1}. The symbols (□), (x), (△), denote initially random (DX), aligned (D1), and neutral (D3) orientations, respectively. Error bars represent the standard deviation.

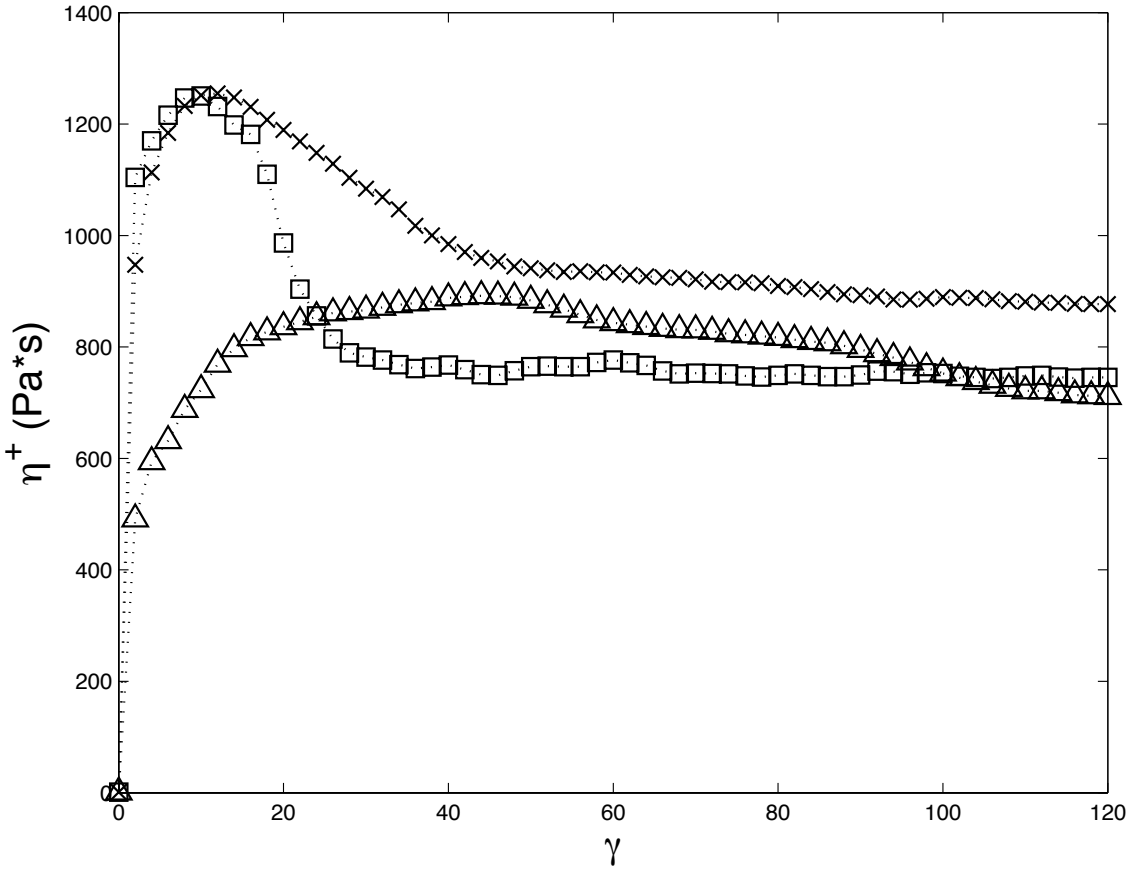

Figure 3.6: Comparison of the effect of initial orientation on the transient viscosity of a 10 wt.% long glass fiber system sheared at 1.0 s^{-1}. The symbols (□), (x), (△), denote initially random (DX), aligned (D1), and neutral (D3) orientations, respectively.

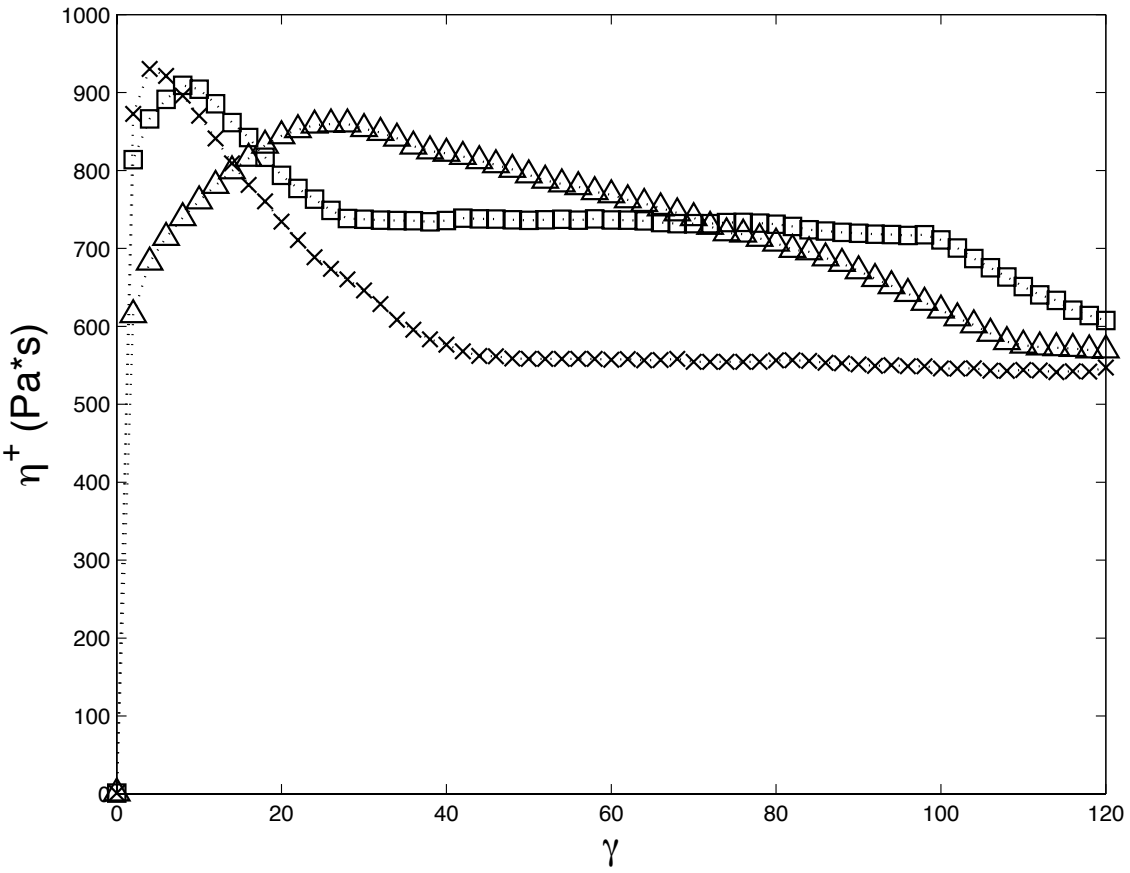

Figure 3.7: Comparison of the effect of initial orientation on the transient viscosity of a 10 wt.% long glass fiber system sheared at 4.0 s^{-1}. The symbols (□), (x), (△), denote initially random (DX), aligned (D1), and neutral (D3) orientations, respectively.

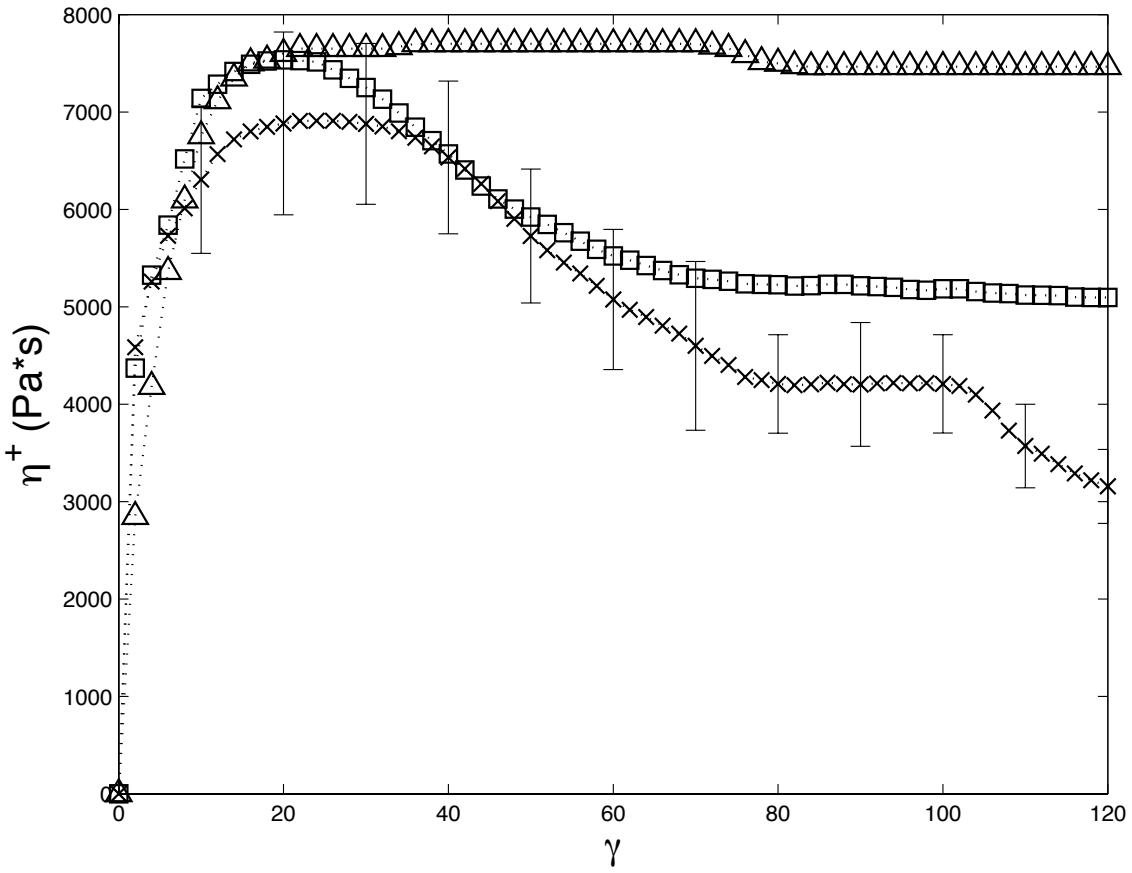

Figure 3.8: Comparison of the effect of initial orientation on the transient viscosity of a 30 wt.% long glass fiber system sheared at 0.4 s^{-1}. The symbols (□), (x), (△), denote initially random (DX), aligned (D1), and neutral (D3) orientations, respectively. Error bars represent the standard deviation.

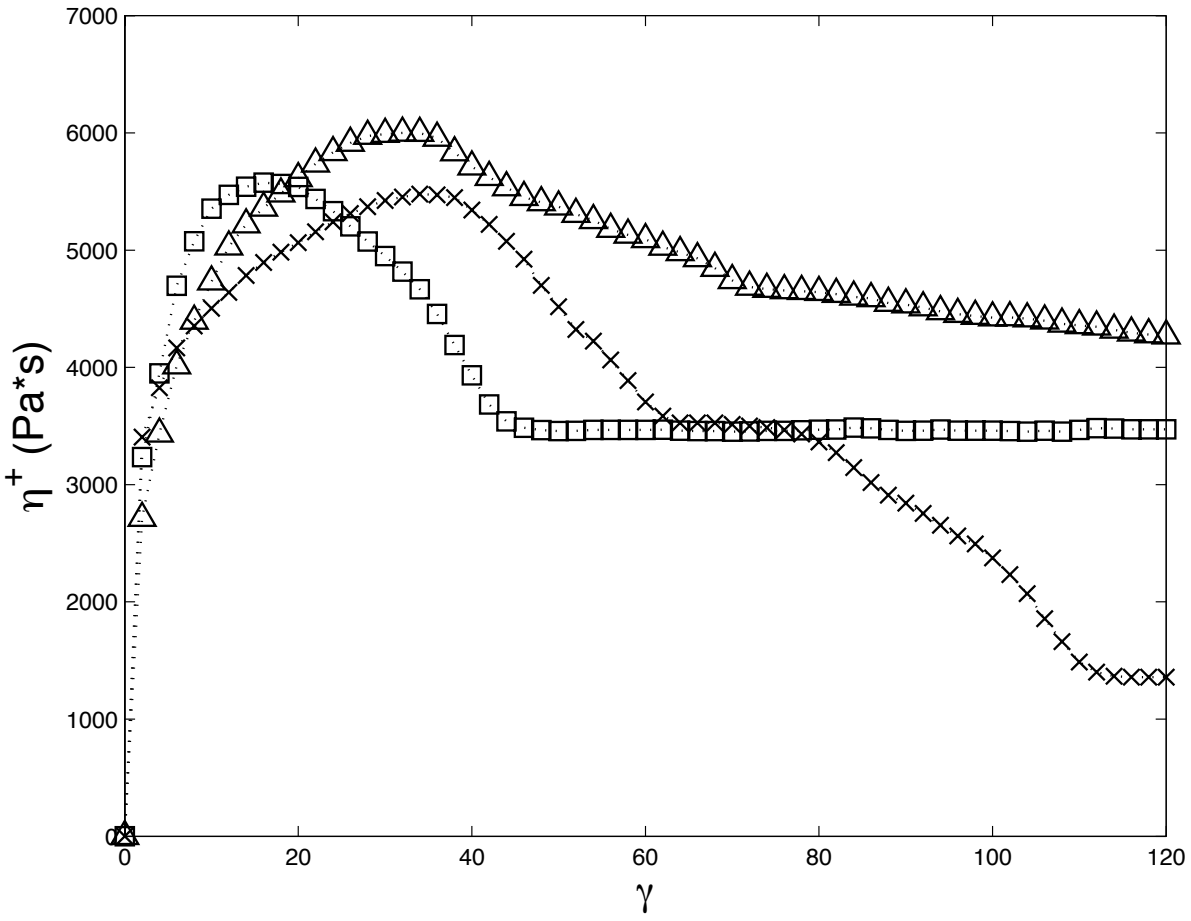

Figure 3.9: Comparison of the effect of initial orientation on the transient viscosity of a 30 wt.% long glass fiber system sheared at 1.0 s^{-1}. The symbols (□), (x), (△), denote initially random (DX), aligned (D1), and neutral (D3) orientations, respectively.

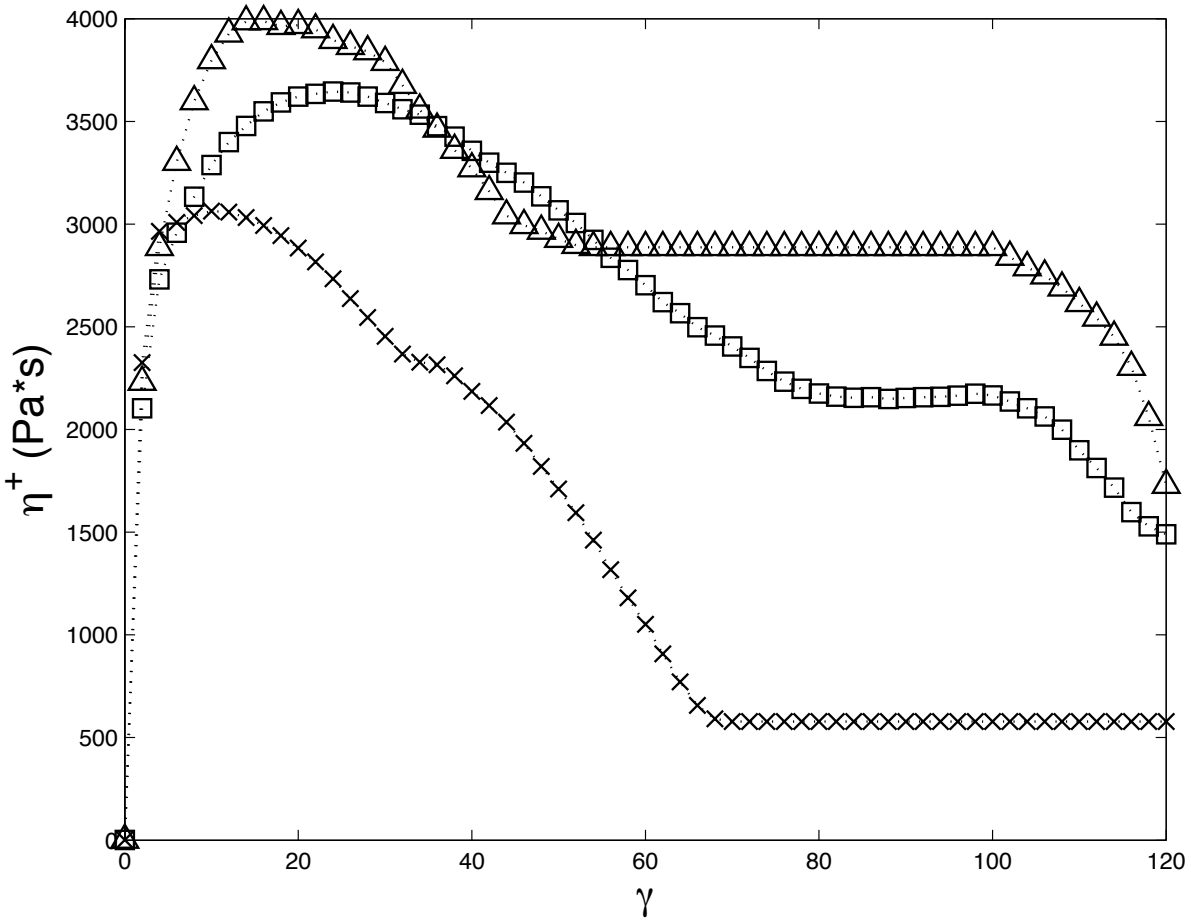

Figure 3.10: Comparison of the effect of initial orientation on the transient viscosity of a 30 wt.% long glass fiber system sheared at 4.0 s^{-1}. The symbols (□), (x), (△), denote initially random (DX), aligned (D1), and neutral (D3) orientations, respectively.

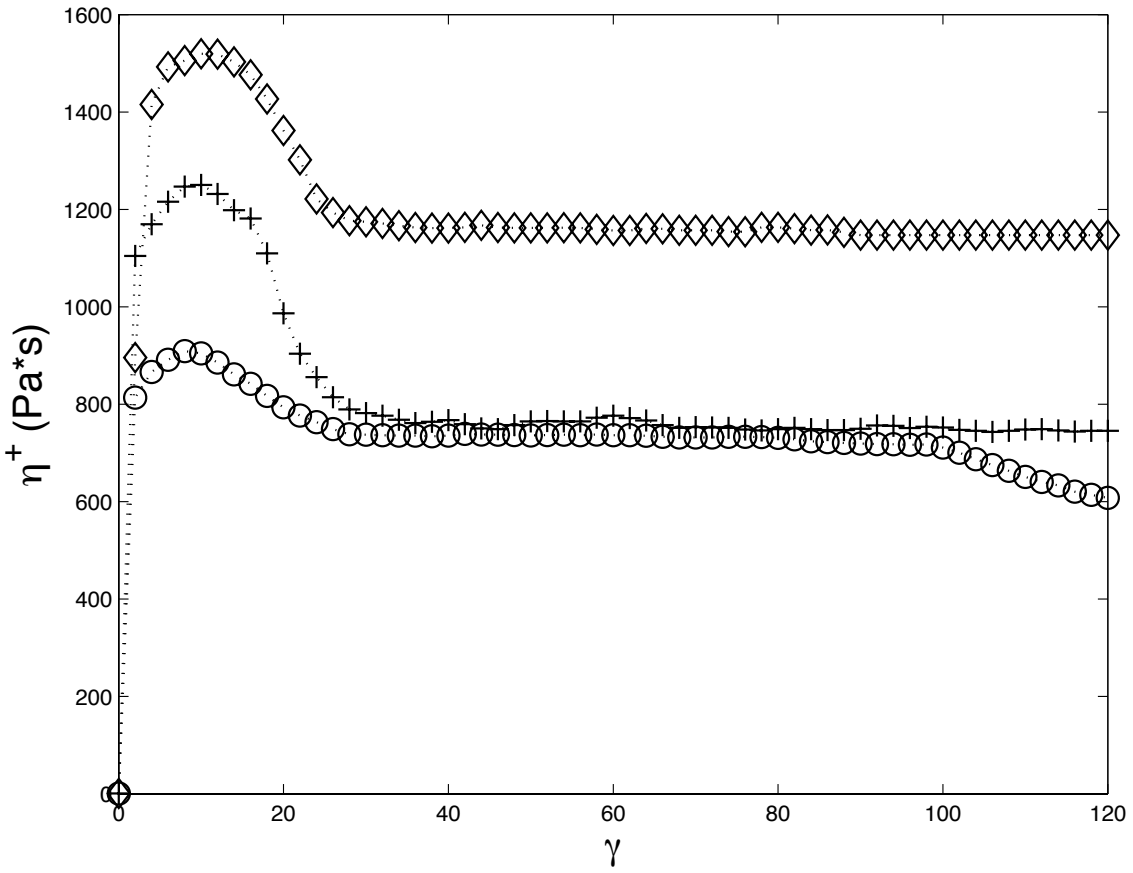

Figure 3.11: Comparison of the effect of shear rate on the transient viscosity of a 10 wt.% long glass fiber system initially random (DX). The symbols (◇), (+), (◯), denote samples sheared at 0.4, 1.0, and 4.0 s^{-1}, respectively.

Chapter 4

Using Startup of Steady Shear Flow in a Sliding Plate Rheometer to Determine Material Parameters for the Purpose of Predicting Long Fiber Orientation

Preface

This chapter assesses the performance of an orientation and stress model based on bead-rod theory, in its ability to predict fiber orientation in a simple shear flow, using model parameters determined from a rheological study conducted using a sliding plate rheometer. This chapter provides extensions for the Bead-Rod model to non-dilute suspension, proposes a stress addition that accounts for fiber flexibility, and proposes empirical modifications to stress theory that resulted in better rheological performance. This chapter is organized as a manuscript for publication.

Using Startup of Steady Shear Flow in a Sliding Plate Rheometer to Determine Material Parameters for the Purpose of Predicting Long Fiber Orientation

Kevin Ortman, Donald Baird
Chemical Engineering, Virginia Tech, Blacksburg, VA 24061

Peter Wapperom
Mathematics, Virginia Tech, Blacksburg, VA 24061

Abby Whittington
Material Science and Engineering, Virginia Tech, Blacksburg, VA 24061

4.1 Abstract

The properties of long glass fiber reinforced parts, such as those manufactured by means of injection molding and compression molding, are highly dependent on the fiber orientation generated during processing. A sliding plate rheometer was used to understand the transient stress and orientation of concentrated long glass fibers during the startup of steady shear flow, and an orientation model and stress tensor based on semi-flexible fibers were assessed. Specifically, samples of different initial fiber orientations were subjected to the startup of steady shear flow. An orientation model, based on bead and rod theory, was coupled with a derived stress tensor that accounts for the semi-flexibility of the fibers. Orientation and stress model parameters were determined by best fitting these coupled equations to the measured stress data. Results showed the semi-flexible orientation model and stress tensor combination, overall, provided improved rheological results as compared to the Folgar-Tucker model when coupled with the stress tensor of Lipscomb (1988). Furthermore, it was found that both stress tensors required empirical modification to accurately fit the measured data. Both orientation models provided encouraging results when predicting the transient fiber orientation for all initial fiber orientations.

4.2 Introduction

The term "long fiber" is used in this context to describe fibers that are able to bend or flex during flow and thus during processing. This bending and flexing, therefore, could affect both the material's microstructure and properties. Subsequently, the term "flexibility" will be used to describe the fiber's ability to bend in the presence of flow. Specifically, a fiber exhibiting a larger degree of flexibility is easier to bend within a specified flow field. Switzer and Klingenberg (2003) quantified the effective stiffness (S^{eff}) of a fiber in a viscous medium by proposing a dimensionless group that contains both the viscosity of the matrix, the fiber aspect ratio ($a_r = L/d$, where L is the fiber length and d is the diameter) and the Young's modulus (E_Y) of the fiber:

$$S^{eff} = \frac{E_Y \pi}{64 \eta_m \dot{\gamma} a_r^4} \tag{4.1}$$

In Eq. 4.1, η_m is the matrix viscosity and $\dot{\gamma}$ is the shear rate. From this expression, the stiffness of a fiber can be seen to decrease (increased flexibility) with aspect ratio for a given material (ie. fixed Young's modulus). Glass fibers less than 1 mm in length are often considered to be "short" (and hence rigid) while fibers of length greater than 1 mm are considered to be "long" (and hence flexible).

Predicting the transient rheological response of long fiber suspensions is complex because of various factors such as fiber-matrix interaction and fiber-fiber interactions. These factors become more prominent in high concentration regimes, where the volume fraction of fibers (ϕ) is $\geq a_r^{-1}$ (Doi and Edwards, 1988). This is because as fiber concentration is increased, short range hydrodynamic forces, frictional, and other mechanical interactions between the fibers also increase. As a result, direct simulations have been used to model fibers from a fundamental approach to explore and understand a wide variety of phenomena. Model fiber equations are usually constructed for a single or small population of fibers and consist of the equations of forces and torques that evolve the particles and fiber configurations over time. Many authors use direct simulations to try and explore phenomena believed to be of interest, such as long and short range hydrodynamic effects, flexibility, Coulombic forces, and frictional forces, for example see the works of Yamamoto and Matsuoka (1993, 1995), Skjetne et al. (1997), and Joung and Fan (2001). Direct simulations, however, are currently very limited in their application to real processing flows due to the high computational resources needed to use them.

Keshtkar et al. (2009) were one of the first groups to study the effect of flexibility on the transient shear rheology of fiber suspensions. They studied the start-up and flow reversal rheology of fibers with different flexibility in a Newtonian oil using a parallel disk rheometer. They found an increase in both the start-up viscosity and first normal stress difference with increased flexibility and also a delayed response in flow reversal. Later, Keshtkar et al. (2010) also began a quantitative analysis of the transient fiber orientation. Experimentally, they found fibers with increased flexibility orientated more slowly than rigid fibers. In this work, they used rheological data to obtain orientation material parameters for an orientation and a stress model based on the GENERIC framework of Rajabian et al. (2005). This model, applicable for non-dilute suspensions, was constructed to supply a mesoscopic level of information pertaining to the microstructure fiber evolution and the resulting stresses within the suspension. This model has the advantage of supplying consistency between the flow dynamics equations and thermodynamics. Simulation results showed that the viscosity could be fitted reasonably well, but obtained relatively poor performance in fitting the normal stress difference. On comparison between the model's predicted transient orientation and experimentally measured values, they found that the model parameters obtained from the rheology only qualitatively represented the transient orientation.

The conventional way of handling fiber orientation stems from short fiber theory wherein the orientation of a rigid fiber can be described as a vector that is parallel to the fiber, denoted in Fig. 4.1 as **p**. For a given orientation distribution function ψ, wherein ψ

describes the probability of finding a fiber of specific orientation within a differential volume of space, the second moment of ψ may be evaluated in the following way to form an orientation tensor (**A**).

$$\mathbf{A}(t) = \int \mathbf{pp}\,\psi(\mathbf{p},t)d\mathbf{p} \tag{4.2}$$

The orientation tensor provides a convenient means of describing the orientation of a population of fibers. For example, if the fibers are all oriented in the 1-direction (i.e. the flow direction), the orientation tensor will have an A_{11} component of 1.0, and 0 for all other components. Likewise, an initial 3-direction orientation would have an orientation tensor whose A_{33} component is 1.0, and 0 for all other components. Consequently, fibers randomly oriented in the 1-3 plane will have components $A_{11} = A_{33} = 0.5$, with 0 for all other components.

Originally, Jeffery (1922) derived an expression describing the motion of an ellipsoidal particle in a flow field. In a continuum sense, Jeffery's model is:

$$\frac{D\mathbf{A}}{Dt} = \mathbf{W}\cdot\mathbf{A} - \mathbf{A}\cdot\mathbf{W} + \xi(\mathbf{D}\cdot\mathbf{A} + \mathbf{A}\cdot\mathbf{D} - 2\mathbf{D}:\mathbf{A}_4) \tag{4.3}$$

wherein $\mathbf{W} = [(\nabla \mathrm{v})^t - \nabla \mathrm{v}]/2$ is the vorticity tensor, $\mathbf{D} = [(\nabla \mathrm{v})^t + \nabla \mathrm{v}]/2$ is the rate of strain tensor, and ξ is a shape factor defined in terms of the particles aspect ratio as $\xi = (a_r^2 - 1)/(a_r^2 + 1)$. In this context, the velocity gradient is defined as $\nabla \mathrm{v} = \partial \mathrm{v_j}/\partial \mathrm{x_i}$. The fourth order orientation tensor is defined as the fourth moment of the orientation distribution function as given in Eq. 4.4.

$$\mathbf{A}_4(t) = \int \mathbf{pppp}\,\psi(\mathbf{p},t)d\mathbf{p} \tag{4.4}$$

$\mathbf{A_4}$ requires a closure approximation to decouple this fourth order tensor in terms of the second order orientation tensor **A**. Common forms of this closure approximation are expressed through linear, quadratic, hybrid, and higher order polynomial closures such as the invariant-based optimal fitting (IBOF) approximation (Chung and Kwon 2001). It was also realized that as the aspect ratio of the ellipsoid became larger, the period of orbital dynamics became much longer. If the aspect ratio was forced to be infinitely large, as has been used to approximate the aspect ratio of fibers, ξ approached unity and the period of rotation became infinite and allowed this particle to, within all practical purposes, fully orient with the flow field. In retrospect, it can be seen that Jeffery's model provides a way of describing the motion of a rigid, massless, fiber in an infinitely dilute suspension. All dynamics are purely hydrodynamic (no fiber interactions), but this model provided a starting point for exploring more realistic dynamics.

Folgar and Tucker (1984) hypothesized in non-dilute suspensions that fiber interactions could be captured by an isotropic rotary diffusion term which is added to Jeffery's model as shown in Eq. 4.5:

$$\frac{D\mathbf{A}}{Dt} = \mathbf{W}\cdot\mathbf{A} - \mathbf{A}\cdot\mathbf{W} + \xi(\mathbf{D}\cdot\mathbf{A} + \mathbf{A}\cdot\mathbf{D} - 2\mathbf{D}:\mathbf{A}_4) + 2C_I\dot{\gamma}(\mathbf{I} - 3\mathbf{A}) \tag{4.5}$$

where C_I is the isotropic rotary diffusion coefficient and **I** is the identity tensor, and $\dot{\gamma} = (2\mathbf{D}:\mathbf{D})^{1/2}$ is the scalar magnitude of **D**. Much research has been conducted with Eq. 4.5, but this model in many cases over predicts the rate of fiber orientation and, in general, was found to describe the orientation of short fibers only qualitatively well, such as shown in the works of Bay (1991) and Eberle et al. (2010). In a later paper, Eq. 4.5 was modified to incorporate a method that allowed for the slowing of the orientation dynamics and was referred to as the reduced strain closure (RSC) model (Wang et al. 2008). A Simpler effort has been proposed in the past by Huynh et al. (2001) by incorporating a slip coefficient (α) to be multiplied by the right hand side of Eq. 4.5 to form,

$$\frac{D\mathbf{A}}{Dt} = \alpha\left(\mathbf{W}\cdot\mathbf{A} - \mathbf{A}\cdot\mathbf{W} + \xi(\mathbf{D}\cdot\mathbf{A} + \mathbf{A}\cdot\mathbf{D} - 2\mathbf{D}:\mathbf{A}_4) + 2C_I\dot{\gamma}(\mathbf{I} - 3\mathbf{A})\right) \tag{4.6}$$

In Eq. 4.6, α is a number between 0 and 1, and attempts to reduce the rate of fiber orientation. Adding the slip coefficient to the Folgar-Tucker equation results in a loss of material objectivity, for example see the work of Wang et al. (2009), but the behavior of the model is still valid in the case of simple shear flow, as recognized by Eberle et al. (2010). Additionally, an anisotropic rotary diffusion (ARD) form of the Folgar-Tucker equation exists, but will not be discussed in this research, and instead the reader is referred to the work of Phelps and Tucker (2009).

The first continuum model that accounts for the orientation evolution of semi-flexible fibers is one proposed by Strautins and Latz (2007) and is referred to here as the Bead-Rod model. In this model, a semi-flexible fiber is modeled as two connected "rods" of orientation **p** and **q**, each of length l_B, that may flex about a central pivot point, as shown in Fig. 4.2. The semi-flexible fiber has a resistance to bending and is accounted for by a resistance potential that exists between both rods. When the fiber is perfectly straight no restorative force exists within the fiber. However, if the fiber is placed in a flow that may induce fiber curvature, the fiber bends in response to the drag flow on the "beads."

To model the orientation changes of such fibers, Strautins and Latz (2007) developed the kinematic equations for the bead and rod fiber in Fig. 4.2. Several assumptions are made. First, this model applies for fibers that are only semi-flexible for which $\mathbf{p} \approx -\mathbf{q}$. The exact extent to this restriction, however, is not fully described. Secondly, similar to Jeffrey's equation, the model fiber is to be in an infinitely dilute suspension where only hydrodynamic effects may exist and does not allow for interactions between different fibers. The model describes the evolution of 3 moments of the **p** and **q** vectors in the following manner,

$$\mathbf{A}(t) = \int\int \mathbf{pp}\ \psi(\mathbf{p},\mathbf{q},t)d\mathbf{p}d\mathbf{q} \tag{4.7}$$

$$\mathbf{B}(t) = \int\int \mathbf{pq}\ \psi(\mathbf{p},\mathbf{q},t)d\mathbf{p}d\mathbf{q} \tag{4.8}$$

$$\mathbf{C}(t) = \int\int \mathbf{p}\ \psi(\mathbf{p},\mathbf{q},t)d\mathbf{p}d\mathbf{q} \tag{4.9}$$

Eq. 4.7 is similar to what exists in rigid rod theory (Eq. 4.2) and describes the second moment of any one of the rods with respect to the orientation distribution function. Another orientation tensor describes the mixed product of both rod vectors with the orientation distribution function, Eq. 4.8. Lastly, the first moment of the distribution function, using either rod's orientation vector, Eq. 4.9 is also formed. It is important to note that this vector does not always vanish in the case of the Bead-Rod model as it does for purely rigid rod model. The equations describing the evolution of these moments are given in Eqs. 4.10-4.13.

$$\begin{aligned}\frac{D\mathbf{A}}{Dt} &= \left(\mathbf{W}\cdot\mathbf{A}-\mathbf{A}\cdot\mathbf{W}\right)+\left(\mathbf{D}\cdot\mathbf{A}+\mathbf{A}\cdot\mathbf{D}-2\mathbf{D}:\mathbf{A}_4\right)\\ &\quad ...+\frac{l_B}{2}[\mathbf{Cm}+\mathbf{mC}-2(\mathbf{m}\cdot\mathbf{C})\mathbf{A}]-2k\left(\mathbf{B}-\mathbf{A}\ \mathrm{tr}(\mathbf{B})\right)\end{aligned} \tag{4.10}$$

$$\begin{aligned}\frac{D\mathbf{B}}{Dt} &= \left(\mathbf{W}\cdot\mathbf{B}-\mathbf{B}\cdot\mathbf{W}\right)+\left(\mathbf{D}\cdot\mathbf{B}+\mathbf{B}\cdot\mathbf{D}-\left(2\mathbf{D}:\mathbf{A}\right)\mathbf{B}\right)\\ &\quad ...+\frac{l_B}{2}[\mathbf{Cm}+\mathbf{mC}-2(\mathbf{m}\cdot\mathbf{C})\mathbf{B}]-2k\left(\mathbf{A}-\mathbf{B}\ \mathrm{tr}(\mathbf{B})\right)\end{aligned} \tag{4.11}$$

$$\frac{D\mathbf{C}}{Dt} = \nabla\boldsymbol{v}^t\cdot\mathbf{C}-(\mathbf{A}:\nabla\boldsymbol{v}^t)\mathbf{C}+\frac{l_B}{2}[\mathbf{m}-\mathbf{C}\left(\mathbf{m}\cdot\mathbf{C}\right)]-k\,\mathbf{C}[1-\mathrm{tr}(\mathbf{B})] \tag{4.12}$$

$$\mathbf{m} = \sum_{i=1}^{3}\sum_{j=1}^{3}\sum_{k=1}^{3}\frac{\partial^2 v_{\mathrm{i}}}{\partial x_{\mathrm{j}}\partial x_{\mathrm{k}}}A_{\mathrm{jk}}\,\mathbf{e}_{\mathrm{i}} \tag{4.13}$$

Within these equations, *tr*() represents the trace of a specified tensor, k is the resistive bending potential coefficient. Physically, as the value of k increases, the Bead-Rod model behaves more like a rigid fiber, and in the limit as k approaches infinity, reproduces Jeffery's model (Eq. 4.3) for high aspect ratio particles. Conversely, as k approaches 0, the model fiber behaves more flexibly. In these equations flexibility is induced only by hydrodynamic effects, as quantified by the second order spatial derivatives of the velocity term that exists in Eq. 4.13. Within Eq. 4.13, $\mathbf{m}$ is a vector formed by the summation over the indices ijk, and $\boldsymbol{e}_{\mathrm{i}}$ are the vector component dyads.

To predict the stress response of a fiber suspension, a stress tensor is also needed (in combination with an orientation model). Most of the work pertaining to the understanding of stress theory for fiber suspensions can be traced back to Ericksen (1960), Batchelor (1971), Goddard (1978), Dinh and Armstrong (1984), Shaqfeh and Fredrickson (1990), and Gibson and Toll (1999). In general, researchers often look for a form of a stress equation such that the total stress ($\boldsymbol{\sigma}$) on the suspension is a linear combination of stresses contributed by the suspending medium and the stresses contributed by the particles, as in Eq. 4.14:

$$\boldsymbol{\sigma} = -P\mathbf{I}+\boldsymbol{\tau}_{\mathrm{Matrix}}+\boldsymbol{\tau}_{\mathrm{Particles}} \tag{4.14}$$

In Eq. 4.14, P is the isotropic pressure, $\boldsymbol{\tau}_{\text{Matrix}}$ is the stress contribution from the matrix. Equivalently, $\boldsymbol{\tau}_{\text{Matrix}}$ may be replaced with $\boldsymbol{\tau}_{\text{Matrix}} = 2\eta_{\text{m}}\,\mathbf{D}$. The most general form for the stresses on the suspension is:

$$\boldsymbol{\sigma} = -P\mathbf{I} + 2\eta_m\mathbf{D} + 2\eta_m\phi\left\{a\mathbf{A}_4 : \mathbf{D} + b\left(\mathbf{D}\cdot\mathbf{A} + \mathbf{A}\cdot\mathbf{D}\right) + c\mathbf{D} + fAD_r\right\} \qquad (4.15)$$

wherein, a, b, c and f are geometric shape factors, and D_r is the rotary diffusivity due to Brownian motion. For high aspect ratio particles, such as fibers, $b = 0$. For glass fibers (long and short), Brownian motion is negligible and D_r may considered to be negligible. This reduces Eq. 4.15 to the stress form suggested by Lipscomb (1988) for high aspect ratio particles as shown in Eq. 4.16.

$$\boldsymbol{\sigma} = -P\mathbf{I} + 2\eta_m\left(\mathbf{D} + c\phi\mathbf{D} + N\mathbf{A}_4 : \mathbf{D}\right) \qquad (4.16)$$

In Eq. 4.16, N is a function of the fiber concentration and aspect ratio and c is a parameter attributed to a stress enhancement caused by the presence of a volume fraction of fibers. For completeness, in the case where $c = 0$, the stress theory of both Ericksen (1960) and Hand (1962) is presented. We will, however, retain the slightly more general stress form written in Eq. 4.16 for this research. Much work has gone into analytically determining the values of c and N in the dilute through semi-dilute regimes, see for example the work of Lipscomb (1988). No theory, however, exists for fiber systems that are concentrated and some authors have chosen not to use analytical expressions for c and N, but rather have chosen to use them as a fitting parameter, such as in the work of Eberle et al. (2009). Additionally, strictly speaking, no stress theory to date considers fibers that are flexible. Lastly, the fourth order orientation tensor appears in Eq. 4.16 and may be accompanied by the use of a closure approximation.

Combining this stress expression with the Folgar-Tucker orientation model previously discussed has yielded varying degrees of success depending on the concentration level. For example, in the work of Eberle et al. (2010), rheological measurements for concentrated short fiber suspensions were modeled using the Folgar-Tucker model and the stress tensor in Eq. 4.16. Their results yielded shear stress and normal stress difference overshoots that could not be fit in either the magnitude or peak breadth. This performance is due to a general lack of understanding of concentrated fiber interactions, especially when fiber flexibility is a non-negligible variable. No other studies, known to us, exist in which the transient rheology of concentrated fiber suspensions (short or long) are studied to obtain orientation modeling parameters. Lastly, none of these works include effects of flexibility for concentrated long fiber suspensions.

In this research, we use a sliding plate rheometer to explore the behavior of long glass fibers in simple shear flow. The purpose of this paper is to determine if Bead-Rod theory, when coupled with a stress tensor that accounts for flexibility, can be used to fit the rheological response of long glass fiber suspensions. We will use rigid fiber theory (Folgar-Tucker model coupled with the Libscomb stress model) as a basis for performance comparison. Lastly, we wish to assess the performance of the parameters (obtained form the rheological fits) in their ability to predict the transient fiber orientation, with the hopes of later using these parameters to predict fiber orientation in more complex flows such as found in injection molding.

4.3 Theory

In this section, we discuss modifications made to extend the Bead-Rod theory to non-dilute suspensions. Next, we derive an appropriate stress contribution due to the semi-flexible nature of the Bead-Rod model. Lastly, we suggest empirical modifications, to the stress theory, that are needed to better predict the stress response of long fiber suspensions.

4.3.1 Bead-Rod Modifications

As derived, the Bead-Rod model is applicable for dilute suspensions. Consequently, in an attempt to extend this model for the purpose of exploring non-dilute suspensions, such as those of interest in this research, we considered that the isotropic rotary diffusion term, suggested by Folgar and Tucker (1984), be added to the Bead-Rod model. A derivation of this extension is provided in 4.9 Appendix I. The Bead-Rod model, now applicable for non-dilute suspensions, is given in Eqs. 4.17-4.19.

$$\frac{D\mathbf{A}}{Dt} = \alpha\left[\left(\mathbf{W}\cdot\mathbf{A}-\mathbf{A}\cdot\mathbf{W}\right)+\left(\mathbf{D}\cdot\mathbf{A}+\mathbf{A}\cdot\mathbf{D}-2\mathbf{D}:\mathbf{A}_4\right)-6C_I\dot{\gamma}\left(\mathbf{A}-\frac{1}{3}\mathbf{I}\right)\right.$$
$$\left.\ldots+\frac{l_B}{2}\left[\mathbf{Cm}+\mathbf{mC}-2(\mathbf{m}\cdot\mathbf{C})\mathbf{A}\right]-2k\left(\mathbf{B}-\mathbf{A}\ \mathrm{tr}(\mathbf{B})\right)\right] \tag{4.17}$$

$$\frac{D\mathbf{B}}{Dt} = \alpha\left[\left(\mathbf{W}\cdot\mathbf{B}-\mathbf{B}\cdot\mathbf{W}\right)+\left(\mathbf{D}\cdot\mathbf{B}+\mathbf{B}\cdot\mathbf{D}-\left(2\mathbf{D}:\mathbf{A}\right)\mathbf{B}\right)-4C_I\dot{\gamma}\mathbf{B}\right.$$
$$\left.\ldots+\frac{l_B}{2}\left[\mathbf{Cm}+\mathbf{mC}-2(\mathbf{m}\cdot\mathbf{C})\mathbf{B}\right]-2k\left(\mathbf{A}-\mathbf{B}\ \mathrm{tr}(\mathbf{B})\right)\right] \tag{4.18}$$

$$\frac{D\mathbf{C}}{Dt} = \alpha\left[\nabla\boldsymbol{v}^t\cdot\mathbf{C}-(\mathbf{A}:\nabla\boldsymbol{v}^t)\mathbf{C}+\frac{l_B}{2}\left[\mathbf{m}-\mathbf{C}\left(\mathbf{m}\cdot\mathbf{C}\right)\right]-k\mathbf{C}\left[1-\mathrm{tr}(\mathbf{B})\right]-2C_I\dot{\gamma}\mathbf{C}\right] \tag{4.19}$$

$$\mathbf{m} = \sum_{i=1}^{3}\sum_{j=1}^{3}\sum_{k=1}^{3}\left[\left(\frac{\partial^2 v_{\mathrm{i}}}{\partial x_{\mathrm{j}}\partial x_{\mathrm{k}}}+K_{ijk}\right)A_{\mathrm{jk}}\,\mathbf{e}_{\mathrm{i}}\right] \tag{4.20}$$

Each term containing C_I in Eqs. 4.17-4.19 is the associated isotropic rotary diffusion term as it applies to the Bead-Rod model. Additionally, α has been added to each of the above equations, and retains the identical meaning as it does when used with the Folgar-Tucker model, Eq. 4.6. In this form of the Bead-Rod model, flexibility may be induced by a combination of rotary diffusion and by hydrodynamic effects. Additionally, we propose a term K_{ijk} be added to Eq. 4.13 to allow for bending that may be caused by additional interactions that exist in non-dilute suspensions, but will not be explored in this work (K_{ijk} = 0).

4.3.2 Bending Stress Addition

A bending stress may be derived, see 4.10 Appendix II, from the bending potential function within the Bead-Rod model and is added to Eq. 4.16. This enhancement in suspension stress is caused by an average non-zero bending angle of the fibers with a restorative potential coefficient, k. In this case of the Bead-Rod model, the total stress of the suspension becomes:

$$\boldsymbol{\sigma}_{\mathrm{BR}} = \boldsymbol{\sigma} + c_3 \eta_m k \frac{3\phi a_r}{2} \left(\mathbf{B} - \mathbf{A}\, tr(\mathbf{B}) \right) \tag{4.21}$$

In Eq. 4.21, c_3 is a parameter that is suggested for non-dilute fiber suspensions, wherein fiber-fiber interactions exist. For the purpose of this research, however, we will restrict ourselves to the theoretical value of $c_3 = 1$. Additionally, Eq. 4.21 can be written in terms of a tensor derived from the second moment of the end-to-end vector of the Bead-Rod fiber. In this manner, Eq. 4.21 becomes Eq. 4 2:

$$\boldsymbol{\sigma}_{\mathrm{BR}} = \boldsymbol{\sigma} + c_3 \eta_m k \frac{3\phi a_r}{2} \frac{tr(\mathbf{r})}{2 l_B^{\,2}} \left(\mathbf{A} - \mathbf{R} \right) \tag{4.22}$$

where the tenor $\mathbf{r}$ is formed by taking the second moment of the end-to-end vector with respect to ψ, and $\mathbf{R}$ is a normalized dimensionless form of $\mathbf{r}$, as defined in Eqs. 4.23-4.25:

$$\mathbf{r} \equiv \int\int l_B^{\,2} (\mathbf{p} - \mathbf{q})(\mathbf{p} - \mathbf{q})\ \psi(\mathbf{p},\mathbf{q},t) d\mathbf{p} d\mathbf{q} \tag{4.23}$$

$$\mathbf{r} = 2 l_B^{\,2} (\mathbf{A} - \mathbf{B}) \tag{4.24}$$

$$\mathbf{R} \equiv \frac{\mathbf{r}}{tr(\mathbf{r})} = \frac{\mathbf{A} - \mathbf{B}}{1 - tr(\mathbf{B})} \tag{4.25}$$

As can be seen in Eq. 4.22, when $\mathbf{R} = \mathbf{A}$ the bending stress term drops out and the original stress equation for a rigid fiber is regained. This occurs in the absence of bending when the flexible fiber is perfectly straight or behaves like a rigid rod. On the other hand, when the fiber does exhibit bending, the end-to-end distance quantified by $tr(\mathbf{r})$ decreases (ie. increased bending) and the magnitude of the stress increases proportionally. Like $\mathbf{A}$, the $tr(\mathbf{R}) = tr(\mathbf{A}) = 1$ and $\mathbf{R}$ is symmetric. For semi-flexible fibers (small bending angles) the values of the components of the two tensors will always be similar.

4.3.3 Empirical Modifications to the Stress Tensor

In this research we considered empirical modifications to the stress theory. Specifically, we propose empirically modifying the Lipscomb model by weighting each term by a function rather than a constant, as shown in the following equations:

$$\boldsymbol{\sigma}_{\mathrm{mod}} = -P\mathbf{I} + 2\eta_m \left(\mathbf{D} + f_1 \phi \mathbf{D} + f_2 \mathbf{A}_4 : \mathbf{D} \right) \tag{4.26}$$

$$f_1 = \begin{cases} \dfrac{c_1}{\dot{\gamma}_{\min}^{\,b}} & \text{for} \quad \dot{\gamma} \le \dot{\gamma}_{\min} \\ \dfrac{c_1}{\dot{\gamma}^{\,b}} & \text{for} \quad \dot{\gamma} > \dot{\gamma}_{\min} \end{cases} \tag{4.27}$$

$$f_2 = c_2\, I_{\mathbf{A}} II_{\mathbf{A}} III_{\mathbf{A}} \tag{4.28}$$

where,

$$I_{\mathbf{A}} = tr(\mathbf{A}) = 1 \tag{4.29}$$

$$II_{\mathbf{A}} = \frac{1}{2}\left[tr(\mathbf{A})^2 - tr(\mathbf{AA})\right] \tag{4.30}$$

$$III_{\mathbf{A}} = \det(\mathbf{A}) \tag{4.31}$$

In this form, f_1 still represents a hydrodynamic enhancement in the stress, due to a presence of a volume fraction of fibers, but now may also represent a steady state stress enhancement due to contacts between fibers. In practice, this term is used to fit experimentally observed shear thinning in excess of that produced with just the matrix. As can be seen by Eq. 4.26, the weighting function f_1 is largest at low $\dot{\gamma}$ and decreases with increasing $\dot{\gamma}$, and allows for shear thinning in excess of that resulting from the matrix, which can be observed experimentally. In this function, b is a fitted exponent that quantifies how the value of f_1 changes with $\dot{\gamma}$, and c_1 is a linear fitting parameter. One obtains Lipscomb's form of this term by setting $b = 0$. To prohibit f_1 from becoming infinite at very low rates of strains, a restraint is enforced below a minimum $\dot{\gamma}$ ($\dot{\gamma}_{\min}$) such that f_1 becomes constant. For example, $\dot{\gamma}_{\min}$ can simply be equated to the lowest $\dot{\gamma}$ employed in the measurements. Similarly, the last term in Eq. 4.26 is also weighted by a function (f_2) whose value, Eq. 4.28, is the product of the invariants of **A**, as defined in Eqs. 4.29-4.31, and is scaled by a fitting parameter c_2. The purpose of this term is to aid in capturing stress overshoots experimentally observed, which would otherwise be very difficult to describe with its original form, ie. Eq. 4.16. The invariants were chosen as weighting functions because they represent scalar quantities that are dependent solely on the orientation state of the system and additionally are not affected by the choice of coordinate system. It is believed that other functions involving the invariants of **A** may also be of use. However Eq. 4.28 represents a simple choice for the purpose of exploring such an empirical modification. Again, f_1 and f_2 are examples of empirical adaptations believed needed to more accurately match the experimentally measured rheological responses of our long fiber suspensions. Lastly, the Bead-Rod stress tensor will be modified in the same way and yields the following form:

$$\boldsymbol{\sigma}_{\text{BR-mod}} = -P\mathbf{I} + 2\eta_m\left(\mathbf{D} + f_1\phi\mathbf{D} + f_2\mathbf{A}_4 : \mathbf{D}\right) + c_3\eta_m k\frac{3\phi a_r}{2}\frac{tr(\mathbf{r})}{2l_B^{\,2}}\left(\mathbf{A} - \mathbf{R}\right) \tag{4.32}$$

4.4 Experimental and Computational Methods

4.4.1 Materials and Preparation

Long glass fiber (LGF) reinforced polypropylene material was provided by SABIC Innovative Plastics and had an initial concentration of 30 wt.% ($\phi = 0.145$). The initial fiber length of 13 mm was reduced significantly during the extrusion process, and it was found via digital imaging that the materials had an average fiber length (L_N) of 3.22 mm. The average diameter of the fibers is d = 14.5 μm. The extrudate was collected and pelletized into long strands to be compression molded for rheological testing. An additional concentration of 10 wt.% ($\phi = 0.048$) material was prepared in the same manner. In all cases, the glass fiber systems used in this research possessed a ϕ such that, using the theory of Doi and Edwards (1988), the suspensions were classified as concentrated, $\phi \geq a_r^{-1}$.

Long glass fiber samples were prepared having 3 different prescribed initial fiber orientations. These samples were initially oriented either in the flow direction (x_1 direction), the neutral direction (x_3-direction), or random in the plane (x_1-x_3 plane), and will be referred to as D1, D3 and DX samples, respectively, as shown by the coordinate system in Fig. 4.3. All samples were prepared and experimented with at 180°C. See the work of Ortman et al. (2011) for more details concerning sample preparation.

4.4.2 Measurement of Fiber Orientations

Fiber orientation of the sheared samples was measured using a micrographic technique proposed by Hine et al. (1996). A digital imaging program was written to analyze the cross-sectional ellipses to determine the values of the orientation tensor. Results shown in this research depict the average of 3 independent samples. Within each polished sample, at least 1,000 fibers for each 10 wt.% sample and 3,000 fibers for each 30 wt.% sample were analyzed over the polished sample dimensions. Again, a more detailed discussion has been presented in Ortman et al. (2011).

4.4.3 Physical Property Values

This section discusses our choice for handling the physical property values of l_B, k and η_m. Two model variables, both l_B and k, are present in the Bead-Rod model and are related to physical characteristics of the fibers. First, l_B is defined as the half length of a fiber. In the case of our samples, a population of fiber lengths exists. Hence, to describe the population of fibers with one l_B value, we have chosen to use the number average l_B associated with our fiber length distribution. Hence, this length scale simply becomes $l_B = L_N / 2$, or l_B = 1.61 mm. Like wise, we need to associate a single k value to the population of fibers. To do this, we choose to calculate the number average k value over the fiber length distribution, where n_i is the number of fibers associated with each k_i, in the following manner,

$$k = \frac{\sum_i n_i k_i}{\sum_i n_i} \tag{4.33}$$

As a reminder, k is the bending potential (energy) coefficient associated with the internal rigidity of a fiber, and to be consistent with Strautins and Latz (2007), is weighted inversely proportional to the coefficient of drag of a fluid on a sphere (C_d) and l_B^2. In physical terms, we have chosen to associate this term with the bending potential of a beam under small deflection, and weight it accordingly. In this manner each k_i is a function of E_Y, d, η_m, and the l_B of each fiber in the population. In these terms, k_i becomes,

$$k_i = \left(\frac{E_Y}{64\ \eta_m} \right) \frac{d^3}{l_{B\,i}^{\ 3}} \tag{4.34}$$

For glass fibers E_Y = 80 GPa and η_m = 560 Pa s, then after using Eq. 4.34 in combination with our fiber length distribution, k = 218 s^{-1}. As k approaches infinity it becomes stiffer, and as it approaches 0 it becomes perfectly flexible. Our value will demonstrate itself to be only semi-flexible within our rheological experiments.

Lastly, for the purpose of the stress tensors used in this research, the experimentally measured matrix viscosity will be calculated at each shear rate and inputted for η_m within the stress equations (Eqs. 4.26 and 4.32). This eliminates the need to fit a generalized Newtonian model to the matrix viscosity.

4.4.4 Parameter Fitting and Numerical Methods

The major goal of this work is to obtain a unique set of rheological model parameters for a given material (ie. fiber length, concentration, matrix properties) and then and assess the accuracy of the model in being able to predict the transient fiber orientation. Although being able to model the rheology is important, the most important aspect is to predict the evolution of fiber orientation and then eventually translate this information into more complex flow situations. To obtain these model parameters, we choose to best fit our models to the DX samples (i.e. samples with an initial random fiber orientation) for both the 10 wt.% and 30 wt.% materials.

The method for obtaining the parameters is outlined in Fig. 4.4. The initial orientation for our samples is measured and numerically specified for each simulation. The orientation and stress model parameters are initially guessed. Next, the orientation equations are solved and the stress equation is calculated and numerically compared to rheological data. The difference between the calculated stress and the rheologically measured stress, or residual difference, is squared and summed. Next, stress parameters are minimized to find a local minimum. Once accomplished, orientation model parameters are then again revisited to try to obtain even lower residual differences. This process is continued several times until the closest global minimum is obtained. This process is computed manually as such a nonlinear and multivariable minimization is

often very difficult. A commercial solver (Mathematica) was used to solve the initial value, differential orientation equations.

4.4.5 Closure Approximations

A closure approximation was used to decouple the fourth order orientation tensor $\mathbf{A}_4$ in terms of the second order orientation tensor $\mathbf{A}$. In this research, we used the 5th degree polynomial IBOF closure approximation both in the Folgar-Tucker model and in the Bead-Rod model, Eq. 4.17. The reader is referred to work of Chung and Kwon (2001) for a description of the IBOF closure approximation. It will be stated, for completion, that during the derivation of the Bead-Rod model higher mixed moments of both **p** and **q** naturally arose. These moments too required closure, and Strautins and Latz (2007) listed criteria that should be met to provide such closures. In the end, a closure relationship similar to the quadratic closure, see for example Advani and Tucker (1990), was used within Eqs. 4.18-4.19. We will follow their approach and use Eqs. 4.18-4.19 as written in this text.

4.4.6 Initial Conditions

Samples were prepared with various initial fiber orientations (DX, D3, and D1) and this initial orientation was measured using the method discussed in Section 4.4.2. For a given initial arrangement, the initial orientations only differed slightly between samples with different fiber concentrations. This difference is within experimental error. Hence, for each initial fiber arrangement (DX, D3, and D1), the same initial orientation conditions were used for both 10 wt.% and 30 wt.% samples. Additionally, because we are interested in a two-dimensional (2D) simulation of the fiber orientation, the orientation components in the neutral direction will be set to 0 (ie. $A_{i3} = 0$, and $A_{3i} = 0$). The initial measured orientation for each fiber arrangement is listed below.

$$\underline{\text{DX}}\quad \mathbf{A}(0) = \begin{pmatrix} 0.565 & 0.037 & 0 \\ 0.037 & 0.038 & 0 \\ 0 & 0 & 0.397 \end{pmatrix}, \quad \underline{\text{D3}}\quad \mathbf{A}(0) = \begin{pmatrix} 0.093 & 0.065 & 0 \\ 0.065 & 0.080 & 0 \\ 0 & 0 & 0.827 \end{pmatrix}, \quad \underline{\text{D1}}\quad \mathbf{A}(0) = \begin{pmatrix} 0.863 & 0.025 & 0 \\ 0.025 & 0.043 & 0 \\ 0 & 0 & 0.094 \end{pmatrix} \tag{4.35}$$

For the Bead-Rod Model, other initial conditions are needed for Eqs. 4.18-4.19. As of now, fiber curvature cannot be measured, so we have chosen to assume that the fibers are initially straight before each experiment, hence, $\mathbf{B}(0) = -\mathbf{A}(0)$, and $\mathbf{C}(0) = \mathbf{0}$.

4.5 Simulation Results and Discussion

In this section, we discuss the performance of the stress models' ability to match the transient rheology obtained with the sliding plate rheometer. A discussion of the rheological behavior itself, however, has already been provided by Ortman et al. (2011) and for brevity will not be reproduced here. We will also analyze the ability of the models to predict fiber orientation.

4.5.1 30 wt.% Materials

Parameters for all the materials were determined using the transient viscosity data obtained for the DX samples (at each concentration), and are listed in Table 4.1. For the semi-flexible fiber predictions, a combination of the Bead-Rod model (Eqs. 4.17-4.20) and its corresponding stress model Eq. 4.32 was used and will be referred to as the BR-$\sigma_{BR\text{-}mod}$ combination. For the rigid fiber predictions, a combination of the Folgar-Tucker model (Eq. 4.6) and the corresponding stress tensor (Eq. 4.26) was used and will be referred to as the FT- σ_{mod} combination. It was found that for both the Bead-Rod model and the Folgar-Tucker model, $C_I > 0$ and $\alpha < 1$ were required to best fit the transient viscosity (η^+).

As can be seen in Fig. 4.5, the BR-$\sigma_{BR\text{-}mod}$ combination does a better job at fitting the transient viscosity for the 30% DX samples at all shear rates than does FT-σ_{mod}. Specifically, the BR-$\sigma_{BR\text{-}mod}$ combination provides a much better representation of the stress overshoot experimentally measured. One will also notice in Fig. 4.5 that when using the Folgar-Tucker and conventional Lipscomb stress tensor (Eq. 4.16) without modification (FT-σ), very poor performance is obtained comparably, especially in its ability to capture the stress overshoot. When the empirically modified stress is used (ie. FT-σ_{mod}), however, the model performs much better. According to fits using the BR-$\sigma_{BR\text{-}mod}$ combination, the magnitude of the bending stress accounts for several percent of the total stress contribution, Eq. 4.32, as is the case at 1.0 s^{-1}. Although not graphically shown, the k value in the Bead-Rod model corresponds only to a very slight degree of bending (reduction in the end-to-end distance << 1%) and increases linearly with shear rate. This bending is directly due to competing forces between the internal rigidity of the fiber and isotropic rotary diffusion. In the case of our glass fibers, isotropic rotary diffusion is much smaller than the internal rigidity of the fibers, and contributes a very small change to the degree of fiber bending. This bending, as stated before, however, was shown to alter the stress response by several percent. Another consequence to the rotary diffusion induced bending is that the Bead-Rod model requires larger C_I values to obtain similar behavior as the Folgar-Tucker model, even at sufficiently rigid k values. Consequently, when using the rotary diffusion term within the Bead-Rod model, this simply means a larger range of C_I values will be needed as compared to that used with the Folgar-Tucker model.

Now that all the model parameters have been determined for the 30 wt.% material (Table 4.1), it is of interest to see how the models' predictions of the orientation compare with experimentally measured values. As can be seen in Fig. 4.6, the overall performance of both models is encouraging. In the case of both orientation models, good accuracy in matching both the rise and steady state values of the A_{11} and A_{33} orientation components is met. Additionally, the Bead-Rod model offers slight improvement in capturing the transient A_{11} component values. It is seen, however, that the Bead-Rod model consistently over predicts the value of the A_{22} orientation component, where as the Folgar-Tucker model more accurately predicts this component. This result is due to the quadratic-like closure approximations used for the mixed orientation moments described in Eqs. 4.18-4.19. As can also be seen in Fig. 4.6, the transient orientation is only slightly dependent on shear rate and appears to be a strain governing phenomenon. A slight deviation from this might be seen at 4.0 s^{-1}, wherein a dip is shown in the rise of

the A_{11} (and A_{33}) component at approximately 35 strain units. Both the Folgar-Tucker and Bead-Rod model predict fiber orientation to be a function of strain.

At this point, it is of interest to evaluate the performance of the parameters determined using the DX samples as a unique set of material parameters for the purpose of predicting η^+ and orientation behavior of the D3 and D1 samples. Predictions for η^+ obtained for the D3 samples as are shown in Fig. 4.7. In this case again, the BR-$\sigma_{BR\text{-}mod}$ combination out performs FT-σ_{mod}. Specifically, at both 1.0 s^{-1} and 4.0 s^{-1}, the BR-$\sigma_{BR\text{-}mod}$ combination more accurately captures the overshoot and breadth of magnitude of the overshoots. The FT-σ_{mod} combination, on the other hand, suggests a much broader and smaller overshoot, which is experimentally indicative of the rheological results obtained at 0.4 s^{-1}. At 0.4 s^{-1}, the FT-σ_{mod} more accurately predicts the actual magnitude of the overshoot, but both models miss the viscosity values.

The orientation predictions of both models for the D3 sample sheared at 1.0 s^{-1} are shown in Fig. 4.8. Both models slightly over predict the transient A_{11} component and under predict the A_{33} component, but certainly qualitatively capture the behavior. This is statement is slightly more true for the case of the Folgar-Tucker model, which shows better orientation performance and provides results that are very close to those observed experimentally. Again, the A_{22} component is over predicted by the Bead-Rod model and is due to the quadratic nature of the closure approximations used for the mix moments in Eqs. 4.11-4.12, even though the IBOF approximation is used for $\mathbf{A}_4$, as discussed in Section 4.4.5.

Lastly, these parameters are used to predict the rheological response for the D1 samples, Fig. 4.9. Both models do a very poor job at capturing the overshoot magnitude of the viscosity response, but both do capture the intermediate viscosity region. Viscosity data past 80 strain units is a phenomenon not yet understood, and is not expected to be captured by any models presently discussed. A more complete discussion of this rheology is given by Ortman et al. (2011). Lastly, the Folgar-Tucker more accurately captures the orientation transition, as seen in Fig. 4.8.

4.5.2 10 wt.% Materials

The same procedure was performed for the samples with a concentration of 10 wt.% fiber. The results of the fitted parameters are indicative of suspensions characterized by less fiber-fiber interactions, as compared to the 30 wt. % material, and are listed in Table 4.1. Specifically, in both the BR-$\sigma_{BR\text{-}mod}$ and the FT-σ_{mod} combinations, lower C_I and c_2 values and higher α values are needed to fit the η^+ suggesting less fiber-fiber interaction. Concerning the Bead-Rod model, less bending is predicted results from the lower C_I value. Again, this suggests less fiber-fiber interactions occur at lower fiber loadings, which is expected. Also, lower c_1 values and higher b values are needed to match the viscosity for both models, which we believe suggests less inter-fiber frictional stresses, at steady state, as compared to the 30 wt. % materials. To elaborate, lower c_1 values reduce the stress contribution in Eq. 4.27, and larger b values increase the denominator of this term and thus again reduce the stress contribution more (especially at increased shear rates).

Looking at η^+ in Fig. 4.10, similar fit performance is obtained in the 10 wt.% DX samples as was gained with the 30 wt.% DX samples. Specifically, the BR-$\sigma_{BR\text{-}mod}$

performs better at predicting the rheological response at the two lowest shear rates, but both models over predict the overshoot magnitude at 4.0 s^{-1}. All model parameters are now specified and it is of interest to assess the performance of the models' orientation predictions. Referring to Fig. 4.11, one can see the Bead-Rod slightly over predicts the rate of orientation at 0.4 s^{-1} and 4.0 s^{-1}, whereas the Folgar-Tucker model captures this rise more accurately. Conversely, the Folgar-Tucker model slightly over predicts the magnitude of the A_{11} component at 120 strain units, whereas the Bead-Rod model more accurately captures this value. However, in all cases, the Folgar-Tucker model performs slightly better at predicting the A_{22} and A_{33} orientation components. Lastly, in Fig. 4.11, we again see that experimental orientation is again predominantly a function of deformation (strain), and does not vary much within the shear rates experimented in this research.

The performance of these parameters is now evaluated for the D3 samples, Fig. 4.12. As once can see, the Folgar Tucker model more accurately predicts the shape of the response, where as the Bead-Rod model over predicts the magnitude of the stress overshoot at each shear rate. Both models, however, due a poor job at accurately predicting the stress values at each shear rate, with the exception of the FT-σ_{mod} performance at 1.0 s^{-1}. The orientation predictions of both models for a D3 sample sheared at 1.0 s^{-1} are shown in Fig. 4.13. Both models slightly over predict the A_{11} component and under predict the A_{33} component values with strain, but still qualitatively capture the behavior.

Lastly, these parameters are used to predict the D1 stress response, Fig. 4.14. The predicted rheological response greatly under predicts the overshoot magnitude for both models explored. Additionally, both models also slightly under predict the steady state viscosity. Both models, however, capture the orientation dynamics, as visualized in Fig. 4.13, and in this case the Bead-Rod model predicts a slightly more accurate description of the A_{11} and A_{33} components.

4.6 Conclusions

In this research, we used a long glass fiber suspension to explore an orientation model and stress tensor designed to provide a first approximation for flexible fiber systems. Specifically, we have extended the Bead-Rod orientation model to non-dilute suspensions by including isotropic rotary diffusion and also derived an appropriate stress tensor term (based on this model) that accounts for the semi-flexibility of the fibers. Additionally, we showed the Lipscomb model, when coupled with the either orientation model explored, was unable to fit the transient stress data, and instead we have proposed empirical modifications to the Lipscomb model that more accurately fits this data. Specifically, in this research we explored empirical modifications to fiber stress theory that utilize functional weights instead of the more classical method of using constant weights.

A method for determining model parameters based on the rheology of fiber systems was demonstrated. Rheological fits showed the Bead-Rod model and associated stress theory, overall, provided a more accurate description of the stress response of the long glass fiber systems explored. Additionally, stresses due to fiber flexibility were predicted to account for small but non-negligible bending stresses. More flexible fiber

systems will be studied in the future, and it is believed that with increased flexibility the Bead-Rod model (and associated stress tensor) will be of increased value.

Lastly, the orientation predictions of both models produced encouraging results in almost all cases. The Bead-Rod model and associated stress tensor, overall, produced better rheological fits and A_{11} orientation component predictions. The Folgar-Tucker model, however, produced better orientation results for the A_{33} and A_{22} in almost all of the cases studied. Experimentally, the transient fiber orientation was seen to be predominately a function of strain, and only varied slightly with shear rate.

This study showed the performance of current orientation models, in simple shear flows, is very encouraging. Understanding the stress development of concentrated fiber suspensions, on the other hand, still has room for improvement. The stress response of long fiber samples was shown to be highly dependent on the initial fiber orientation. Current stress theory does not provide a complete description for such a class of fiber suspension. Results determined in this study will be used in the future to explore the orientation development of long glass fibers in an injection-molded processing flow.

4.7 Acknowledgments

The financial support for this work, from the National Science Foundation through Grant No. CMMI-0853537, is greatly appreciated. We would also like to thank SABIC for providing the materials used in this work. Additional gratitude is given to the Materials Science and Engineering department at Virginia Tech for providing polishing and microscopy facilities.

4.8 References

1. Advani, S.G., C.L. Tucker III, "Closure approximations for three-dimensional structure tensors," J. Rheol. **34**(3), 367-386 (1990).
2. Batchelor, G.K., "The stress generated in a non-dilute suspension of elongated particles by pure straining motion," J. Fluid Mech. **46**, 813-829 (1971).
3. Bay, R.S. "Fiber orientation in injection molded composites: A comparison of theory and experiment," Ph. D., University of Illinois Urbana-Champaign (1991).
4. Chung, D.H., T.H. Kwon, "Improved model of orthotropic closure approximation for flow induced fiber orientation," Polym. Compos. **22**(5), 636-649 (2001).
5. Dinh, S.M., R.C. Armstrong, "A rheological equation of state for semiconcentrated fiber suspensions," J. Rheol. **28**, 207-227 (1984).
6. Doi, M. and S.F. Edwards, "The Theory of Polymer Dynamics," Oxford University Press: New York (1988).
7. Eberle, A.P.R., D.G. Baird, P. Wapperom, G.M. Vélez-García, "Obtaining reliable transient rheological data on concentrated short fiber suspensions using a rotational rheometer," J. Rheo. **53**, 1049-1069 (2009).
8. Eberle, A.P.R., D.G. Baird, P. Wapperom, "Fiber orientation kinetics of a concentrated short glass fiber suspension in startup of simple shear flow," J. Non-Newtonian Fluid Mech. **165**(3), 110-119 (2010).
9. Ericksen, J.L., "Transversely isotropic fluids," Kolloid Z. **173**, 117-122 (1960).
10. Folgar, F.P., C.L. Tucker III, "Orientation behavior of fibers in concentrated

suspensions," J. Reinf. Plast. Compos. **3**, 98-119 (1984).
11. Gibson, A.G., S. Toll, "Mechanics of the squeeze flow of planar fibre suspensions," J. Non-Newtonian Fluid Mech. **82**, 1-24 (1999).
12. Goddard, J.D., "Tensile behavior of power-law fluids containing oriented slender fibers," J. Rheol. **22**, 615-622 (1978).
13. Hand, G.L., "A theory of anisotropic fluids," J. Fluid Mech. **13**, 33-46 (1962).
14. Hine, P.J., N. Davidson, R.A. Duckett, A.R. Clarke, I.M. Ward, "Hydrostatically extruded glass–fiber reinforced polyoxymethylene. I. The development of fiber and matrix orientation," Polym. Compos. **17**, 720–729 (1996).
15. Huynh, H.M., "Improved fiber orientation predictions for injection-molded composites" Master's Thesis, University of Illinois at Urbana-Champaign (2001).
16. Jeffery, G.B., "The motion of ellipsoidal particles immersed in a viscous fluid," Proc. R. Soc. A **102**, 161-179 (1922).
17. Joung, C.G., N. Phan-Thien, X.J. Fan, "Direct simulation of flexible fibers," J. Non-Newtonian Fluid Mech. **99**, 1-36 (2001).
18. Keshtkar, M., M.C. Heuzey, P.J. Carreau, "Rheological behavior of fiber-filled model suspensions: Effect of fiber flexibility," J. Rheo. **53**(3), 631-650 (2009).
19. Keshtkar, M., M.-C. Heuzey, P.J. Carreau, M. Rajabian, C. Dubois, "Rheological properties and microstructural evolution of semi-flexible fiber suspensions under shear flow," J. Rheo. **54**(2), 197-222 (2010).
20. Lipscomb, G.G., M.M. Denn, D.U. Hur, D.V. Boger, "The flow of fiber suspensions in complex geometries," J. Non-Newtonian Fluid Mech. **26**, 197-325 (1988).
21. Ortman, K.C., N. Agarwal, A.P.R. Eberle, D.G. Baird, P. Wapperom, A.J. Giacomin, "Transient shear flow behavior of concentrated long glass fiber suspensions in a sliding plate rheometer," J. Non-Newtonian Fluid Mech. **166**(16), 885-895 (2011).
22. Phelps, J., C.L. Tucker III, "An anisotropic rotary diffusion model for fiber orientation in short- and long-fiber thermoplastics," J. Non-Newtonian Fluid Mech. **156**, 165-176 (2009).
23. Rajabian, M., C. Dubois, M. Grmela, "Suspensions of semiflexible fibers in polymer fluids: rheology and thermodynamics," Rheol. Acta. **44**, 521-535 (2005).
24. Shaqfeh, E.S.G., G.H. Fredrickson, "The hydrodynamic stress in a suspension of rods" Phys. Fluids A **2**, 7-24 (1990).
25. Skjetne, P., R. Ross, D. Klingenberg, "Simulation of single fiber dynamics," J. Chem. Phys. **107**(6), 2108-2121 (1997).
26. Strautins, U. and A. Latz, "Flow-driven orientation dynamics of semiflexible fiber systems," Rheol. Acta. **46**, 1057-1064 (2007).
27. Switzer III, L.H. and D.J. Klingenberg, "Rheology of sheared flexible fiber suspensions via fiber-level simulations", J. Rheo. **47**(3), 759-778 (2003).
28. Wang, J., J. O'Gara, C.L. Tucker III, "An objective model for slow orientation kinetics in concentrated fiber suspensions: Theory and rheological evidence," J. Rheol. **52**(5), 1179-1200 (2008).
29. Yamamoto, S. and T. Matsuoka, "A method for dynamic simulation of rigid and flexible fiber in a flow field," J. Chem. Phys. **98**, 644-650 (1993).
30. Yamamoto, S. and T. Matsuoka, "Dynamic simulation of fiber suspensions in shear flow," J. Chem. Phys. **102**(5), 2254-2261 (1995).

30 wt.%	Folgar-Tucker	Bead-Rod
C_I	5.0×10^{-3}	5.3×10^{-2}
α	0.25	0.13
c_1	15	24
b	1.0	0.65
c_2	5.2×10^{5}	1.4×10^{5}

10 wt.%	Folgar-Tucker	Bead-Rod
C_I	3.5×10^{-3}	4.0×10^{-2}
α	0.32	0.27
c_1	1.5	5
b	2.2	1.4
c_2	3.1×10^{5}	1.1×10^{5}

Table 4.1: Model parameters determined from rheological fits for both the 30 wt.% and 10 wt.% materials.

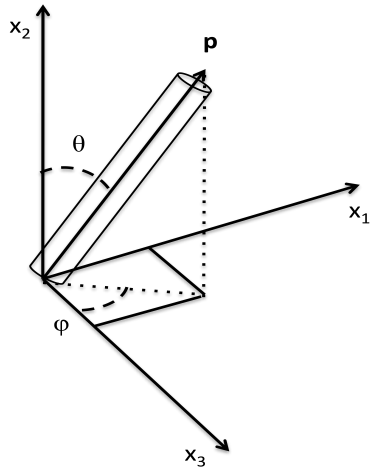

Figure 4.1: Rigid fiber with orientation vector **p**.

Figure 4.2: Sliding plate rheometer and defined coordinate system, Ortman et al. (2011).

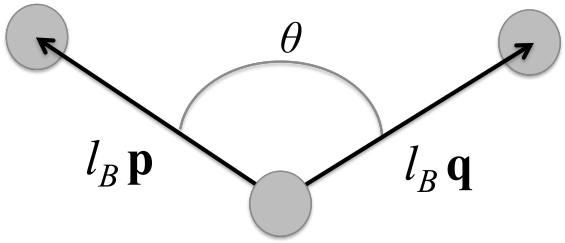

Figure 4.3: Semi-flexible (bead and rod) fiber model of Strautins and Latz (2007). Fiber is constructed by two connected orientation vectors **p** and **q**.

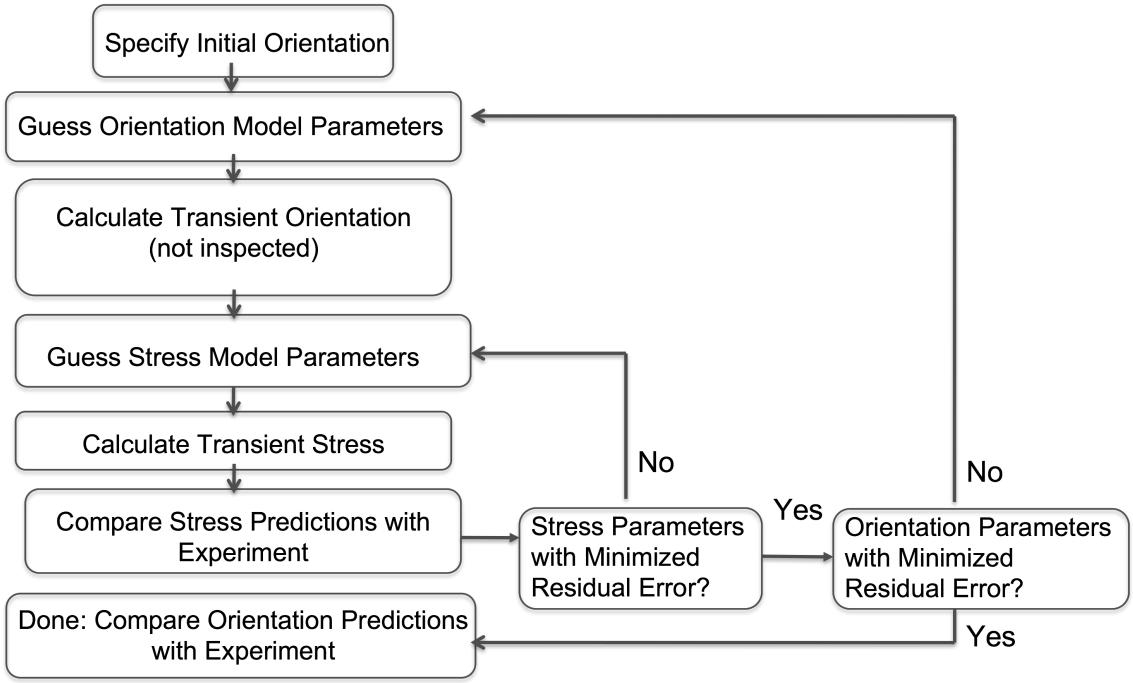

Figure 4.4: Method for determining material parameters from rheological data.

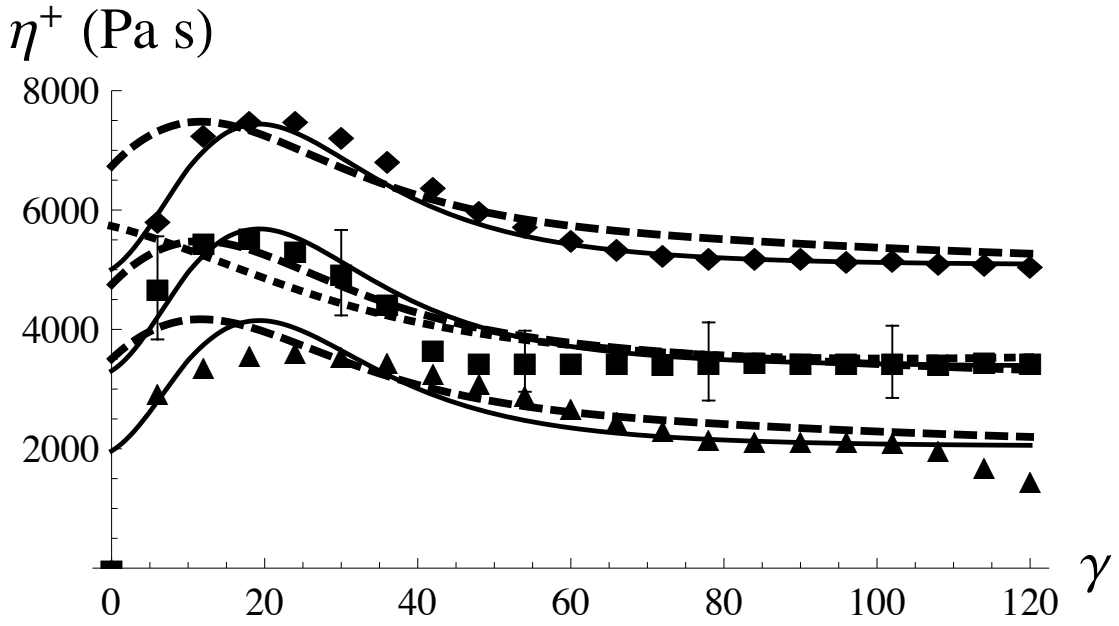

Figure 4.5: Viscosity vs. strain. Rheological data, semi-flexible (solid), and rigid model fits for 30 wt.% DX samples sheared at 0.4 s^{-1} (♦), 1.0 s^{-1} (■) and 4.0 s^{-1} (▲). Fit of Folgar-Tucker model and conventional Lipscomb stress tensor (dotted) for reference. Error bars denote the standard deviation.

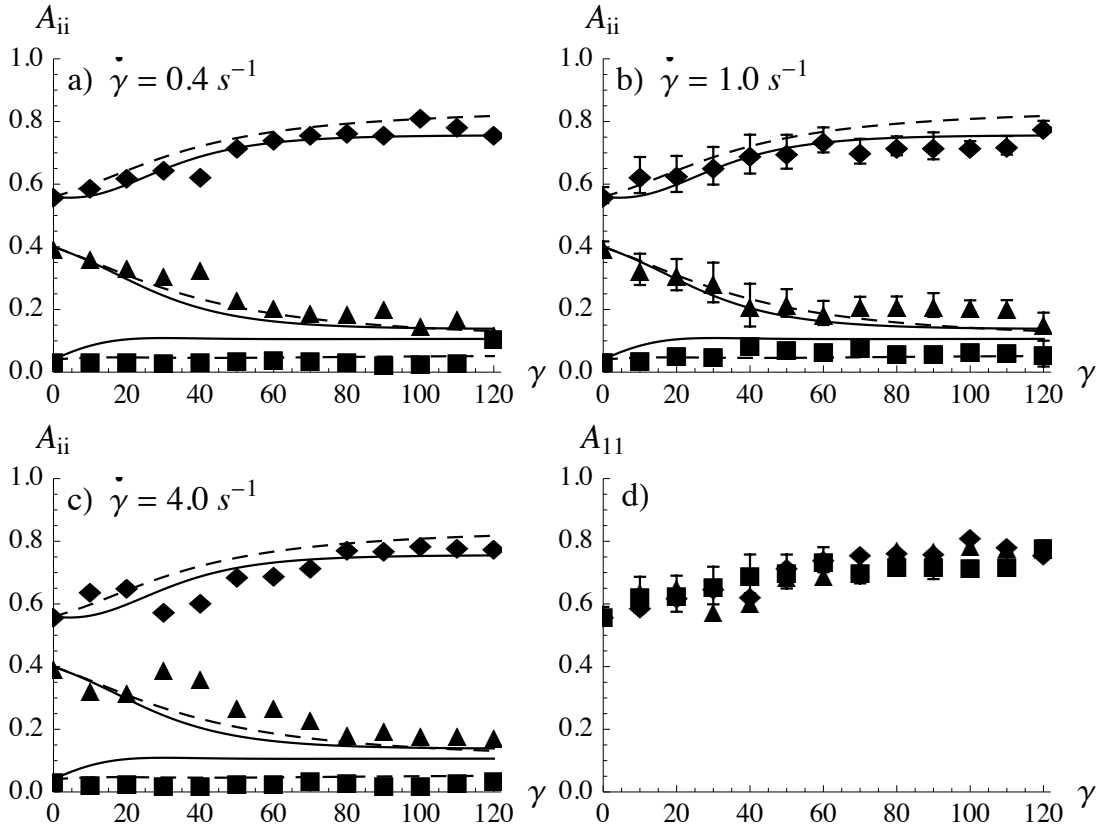

Figure 4.6: Comparison of orientation vs. strain predictions of the Bead-Rod (solid) and Folgar-Tucker (dashed) models with experimental data A_{11} (♦), A_{22} (■), and A_{33} (▲) components for 30 wt.% DX samples sheared at all shear rates, (a) 0.4 s^{-1}, (b), 1.0 s^{-1}, (c) 4.0 s^{-1}. (d) Comparison of experimental A_{11} vs. strain for 0.4 s^{-1} (♦), 1.0 s^{-1} (■) and 4.0 s^{-1} (▲). Error bars denote the standard deviation.

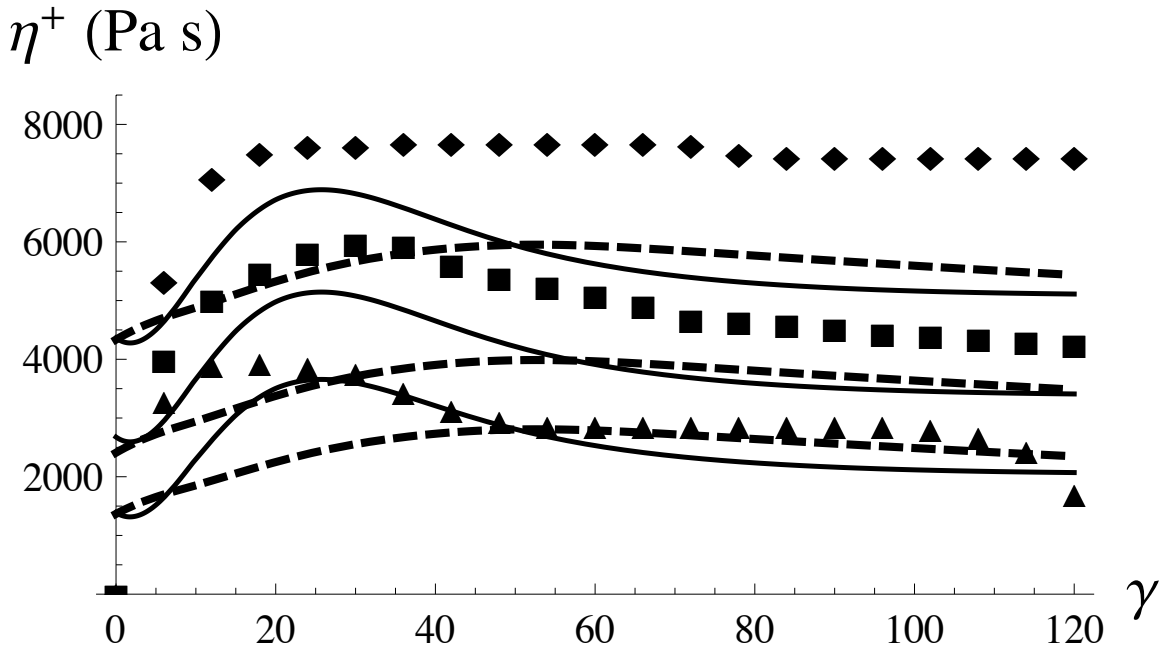

Figure 4.7: Viscosity vs. strain. Rheological data, semi-flexible (solid), and rigid model fits for 30 wt.% D3 samples sheared at 0.4 s^{-1} (♦), 1.0 s^{-1} (■) and 4.0 s^{-1} (▲).

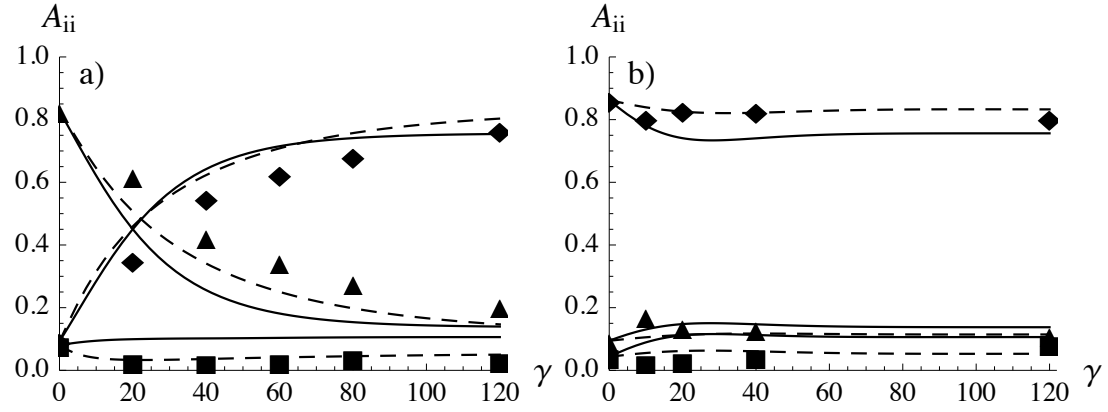

Figure 4.8: (a) Comparison of orientation vs. strain predictions of the Bead-Rod (solid) and Folgar-Tucker (dashed) models with experimental data A_{11} (♦), A_{22} (■), and A_{33} (▲) components for 30 wt.% D3 samples shear ate 1.0 s^{-1} and (b) 30 wt.% D1 samples at 1.0 s^{-1}.

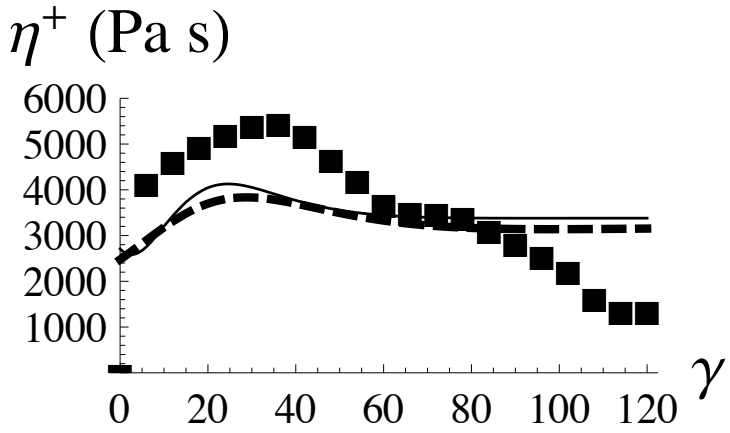

Figure 4.9: Viscosity vs. strain. Rheological data, semi-flexible (solid), and rigid (dashed) model fits for 30 wt.% D1 samples sheared at 1.0 s^{-1} (■).

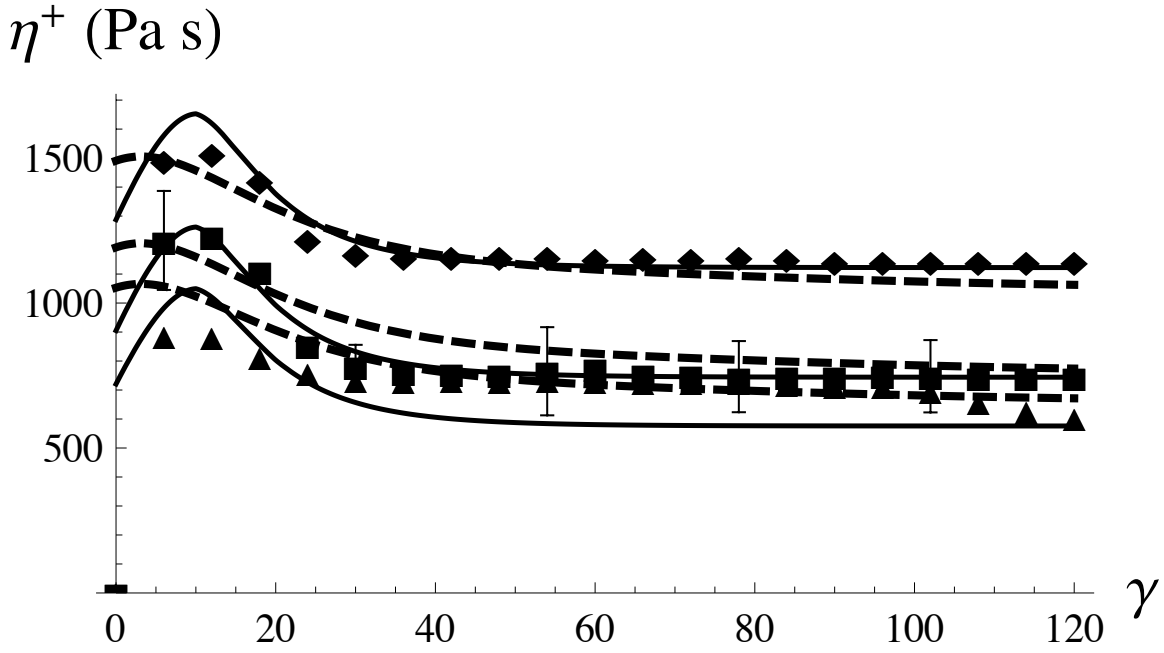

Figure 4.10: Viscosity vs. strain. Rheological data, semi-flexible (solid), and rigid model fits for 10 wt.% DX samples sheared at 0.4 s^{-1} (♦), 1.0 s^{-1} (■) and 4.0 s^{-1} (▲). Error bars denote the standard deviation.

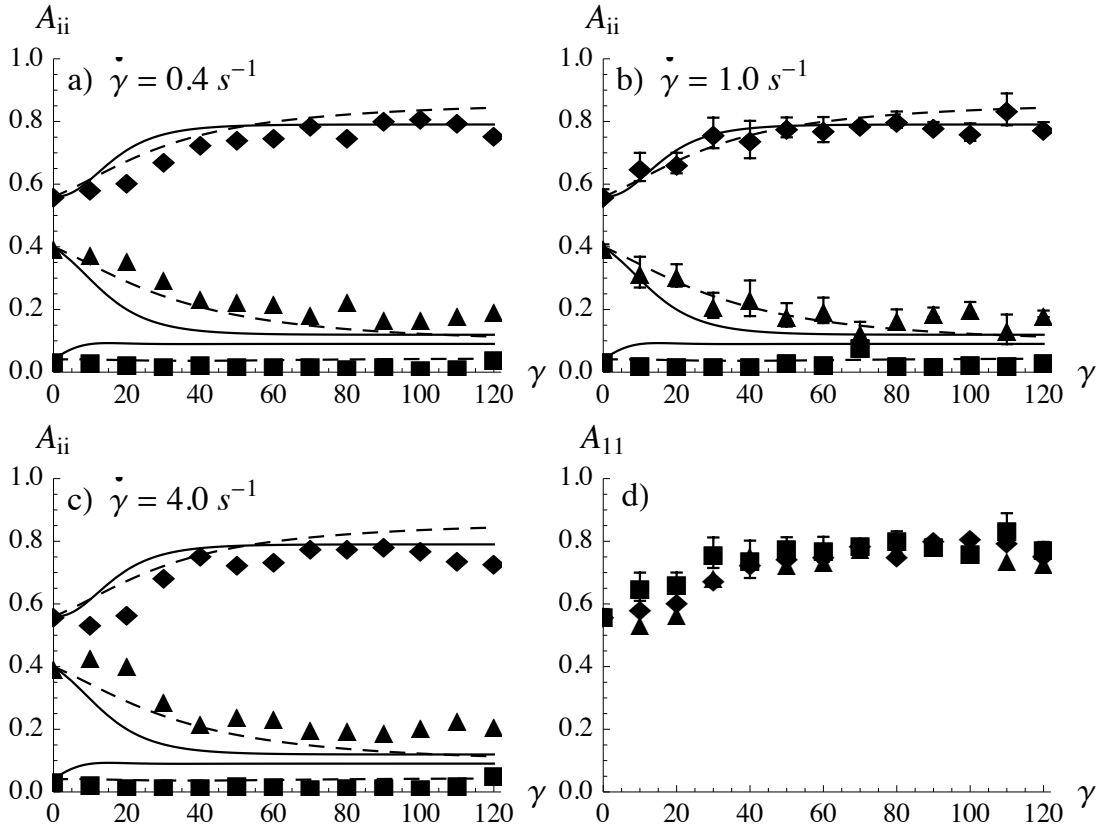

Figure 4.11: Comparison of orientation vs. strain predictions of the Bead-Rod (solid) and Folgar-Tucker (dashed) models with experimental data A_{11} (♦), A_{22} (■), and A_{33} (▲) components for 30 wt.% DX samples sheared at all shear rates, (a) 0.4 s^{-1}, (b), 1.0 s^{-1}, (c) 4.0 s^{-1}. (d) Comparison of experimental A_{11} vs. strain for 0.4 s^{-1} (♦), 1.0 s^{-1} (■) and 4.0 s^{-1} (▲). Error bars denote the standard deviation.

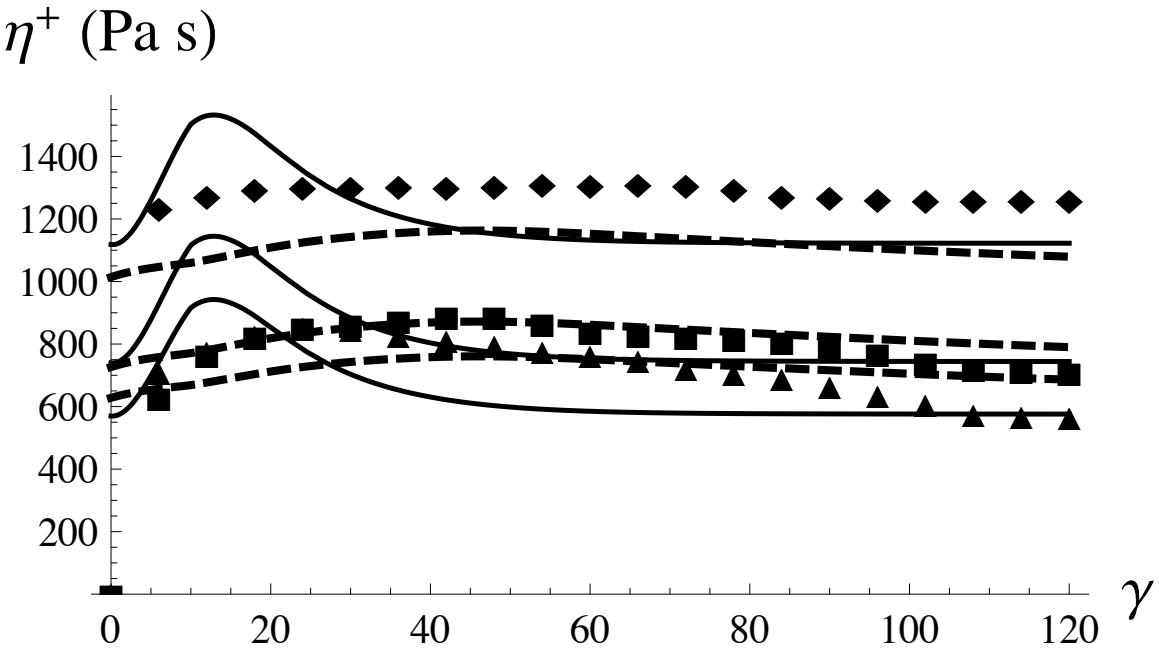

Figure 4.12: Viscosity vs. strain. Rheological data, semi-flexible (solid), and rigid model fits for 10 wt.% D3 samples sheared at 0.4 s^{-1} (♦), 1.0 s^{-1} (■) and 4.0 s^{-1} (▲).

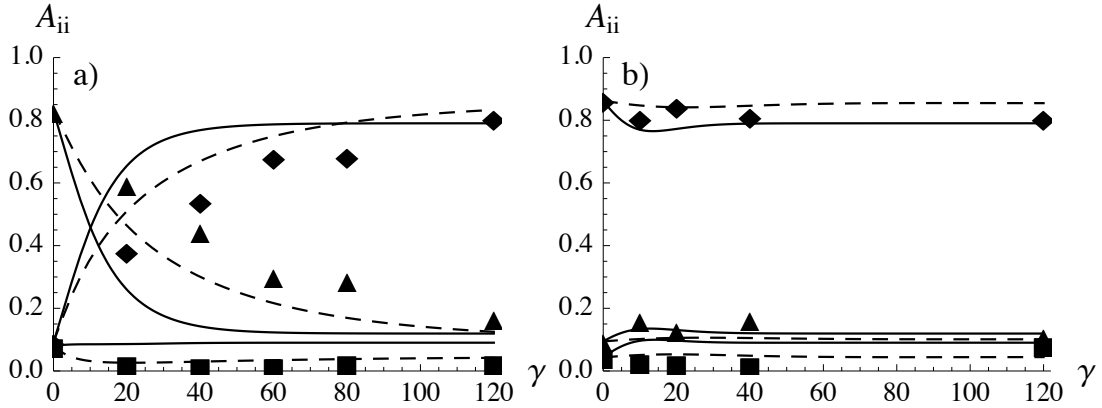

Figure 4.13: (a) Comparison of orientation vs. strain predictions of the Bead-Rod (solid) and Folgar-Tucker (dashed) models with experimental data A_{11} (♦), A_{22} (■), and A_{33} (▲) components for 10 wt.% D3 samples shear ate 1.0 s^{-1} and (b) 10 wt.% D1 samples at 1.0 s^{-1}.

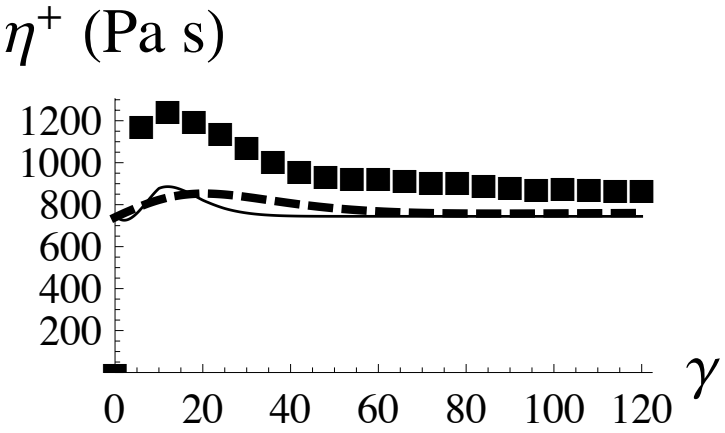

Figure 4.14: Viscosity vs. strain. Rheological data, semi-flexible (solid), and rigid (dashed) model fits for 10 wt.% D1 samples sheared at 1.0 s^{-1} (■).

4.9 Appendix I: Derivation of the Isotropic Rotary Diffusion Terms in the Bead-Rod Model

First, the isotropic rotary diffusion may be introduced into the orientation balance equation. For the Bead-Rod model, this term enters as a combination of diffusion from both rods, as written in Eq. 4.I.1, where D is the rotary diffusion coefficient.

$$D\left(\frac{\partial}{\partial \mathbf{p}^2}+\frac{\partial}{\partial \mathbf{q}^2}\right)\psi(\mathbf{p},\mathbf{q}) \tag{4.I.1}$$

The choice of Folgar and Tucker (1984) is to equate $D = C_I\dot{\gamma}$. We now wish to form the integral moments defined in Eqs. 4.7-4.9 with the rotary diffusion term. For Eq. 4.7 the rotary diffusion term, after some manipulation (see for example Phelps and Tucker (2009)), becomes Eq. 4.I.2.

$$\int\int C_I\dot{\gamma}\left[\left(\frac{\partial}{\partial \mathbf{p}^2}+\frac{\partial}{\partial \mathbf{q}^2}\right)\mathbf{pp}\right]\psi(\mathbf{p},\mathbf{q})d\mathbf{p}d\mathbf{q} \tag{4.I.2}$$

After expansion, the term simplifies to Eq. 4.I.3.

$$\int\int C_I\dot{\gamma}\left(\frac{\partial}{\partial \mathbf{p}^2}\mathbf{pp}\right)\psi(\mathbf{p},\mathbf{q})d\mathbf{p}d\mathbf{q} \tag{4.I.3}$$

This form is exactly the same as that of the Folgar-Tucker model (1984) and upon integration over all orientation space becomes Eq. 4.I.4, which was presented in Eq. 4.17.

$$-6C_I\dot{\gamma}\left(\mathbf{A}-\frac{1}{3}\mathbf{I}\right) \tag{4.I.4}$$

For Eq. 4.8 we are interested in the mixed moment of **p** and **q** in the following manner:

$$\int\int C_I \dot{\gamma}\left(\frac{\partial}{\partial \mathbf{p}^2}+\frac{\partial}{\partial \mathbf{q}^2}\right)\mathbf{pq}d\mathbf{p}d\mathbf{q} \tag{4.I.5}$$

$$=\int\int C_I \dot{\gamma}\frac{\partial}{\partial \mathbf{p}^2}(\mathbf{pq})d\mathbf{p}d\mathbf{q}+\int\int C_I \dot{\gamma}\frac{\partial}{\partial \mathbf{q}^2}(\mathbf{pq})d\mathbf{p}d\mathbf{q} \tag{4.I.6}$$

After expanding the first term (and carrying the second term), this terms becomes:

$$=\int\int C_I \dot{\gamma}\frac{\partial}{\partial \mathbf{p}}\left(\frac{\partial \mathbf{p}}{\partial \mathbf{p}}\mathbf{q}+\mathbf{p}\frac{\partial \mathbf{q}}{\partial \mathbf{p}}\right)d\mathbf{p}d\mathbf{q}+... \tag{4.I.7}$$

The derivative in Eq. 4.I.7 involving the change of **q** with **p** is 0, and simplifies to become:

$$=\int\int C_I \dot{\gamma}\frac{\partial}{\partial \mathbf{p}}\left(\frac{\partial \mathbf{p}}{\partial \mathbf{p}}\mathbf{q}\right)d\mathbf{p}d\mathbf{q}+.... \tag{4.I.8}$$

$$=\int\int C_I \dot{\gamma}\frac{\partial}{\partial \mathbf{p}}\left[(\mathbf{I}-\mathbf{pp})\mathbf{q}\right]d\mathbf{p}d\mathbf{q}+... \tag{4.I.9}$$

Written in component form, the integrand of Eq. 4.I.9 now becomes:

$$=C_I \dot{\gamma}\frac{\partial}{\partial p_l}\left[\left(I_{ij}-p_i p_j\right)q_k\right]+... \tag{4.I.10}$$

After differentiation and simplification, the term becomes:

$$=C_I \dot{\gamma}\left(-\frac{\partial p_j}{\partial p_l}p_j q_k-p_i\frac{\partial p_j}{\partial p_l}q_k\right)+... \tag{4.I.11}$$

$$=C_I \dot{\gamma}\left(-p_j q_k-p_i q_k\right)+... \tag{4.I.12}$$

The same result obtained in Eq. 4.I.12 occurs with the $\frac{\partial(\mathbf{pq})}{\partial \mathbf{q}^2}$ term being carried from Eq. 4.I.6. Therefore, another round of Eq. 4.I.12 is obtained and upon addition becomes Eq. 4.I.13.

$$=-4C_I \dot{\gamma} p_j q_k \tag{4.I.13}$$

Upon integration this term becomes Eq. 4.I.14, which was presented in Eq. 4.18.

$$=\int\int -4C_I \dot{\gamma} p_j q_k d\mathbf{p}d\mathbf{q}=-4C_I \dot{\gamma}\mathbf{B} \tag{4.I.14}$$

Lastly, for Eq. 4.9 we are interested in the single moment of either **p** or **q** (identical solutions will be obtained either way). Let us choose **p** for this discussion, hence the moment of interest becomes Eq. 4.I.15.

$$\int\int C_I \dot{\gamma}\left(\frac{\partial}{\partial \mathbf{p}^2}+\frac{\partial}{\partial \mathbf{q}^2}\right)\mathbf{p}d\mathbf{p}d\mathbf{q} \tag{4.I.15}$$

Upon the first round of differentiation, noting the independence of **q** on **p**, this term becomes:

$$=\int\int C_I \dot{\gamma}\frac{\partial}{\partial \mathbf{p}}(\mathbf{I}-\mathbf{pp})d\mathbf{p}d\mathbf{q} \tag{4.I.16}$$

The integrand of Eq. 4.I.16 is therefore:

$$=C_I \dot{\gamma}\frac{\partial}{\partial p_l}\left(I_{ij}-p_i p_j\right) \tag{4.I.17}$$

The derivative of the identity tensor zeros out and using the chain rule of differentiation, 4.I.17 becomes 4.I.18.

$$=C_I \dot{\gamma}\left(-\frac{\partial p_j}{\partial p_l}p_j - p_i\frac{\partial p_j}{\partial p_l}\right) \tag{4.I.18}$$

Simplification of Eq. 4.I.18 yields 4.I.19.

$$=-2C_I \dot{\gamma} p_j \tag{4.I.19}$$

Lastly, upon integration this term becomes Eq. 4.I.20, which was presented in Eq. 4.19.

$$=\int\int -2C_I \dot{\gamma} p_j d\mathbf{p}d\mathbf{q} = -2C_I \dot{\gamma}\mathbf{C} \tag{4.I.20}$$

4.10 Appendix II: Derivation of the Bending Stress Term for the Bead-Rod Model

We start with the restorative potential function, U(**p**,**q**), for the Bead-Rod model, see Strautins and Latz (2007).

$$U(\mathbf{p},\mathbf{q}) = \tilde{k}(\mathbf{p}.\mathbf{q}+1) \tag{4.II.1}$$

The force on **p**, due to the internal restorative potential therefore is:

$$\mathbf{F}_p = -\frac{\partial U(\mathbf{p},\mathbf{q})}{\partial(l_B\mathbf{p})} = -\frac{\tilde{k}}{l_B}(\mathbf{I}-\mathbf{pp})\ .\mathbf{q} \tag{4.II.2}$$

where the derivative of the potential function is taken on the surface of a sphere. In Eq. 4.II.2, $\tilde{k}$ is the bending potential coefficient and its relationship to *k* (as seen in Eq. the Bead-Rod model) will soon be apparent. We will soon need the force on the **q** rod as well, but this term simply results in another round of Eq. 4.II.2. One may notice that

when **p** = -**q**, the term becomes 0 and no restorative force is exists within the fiber. Using Kramer's stress expression, and also accounting for the stress of the **q** rod, we are lead to an expression for the stress tensor due to bending. The contribution of the **q** rod is exactly the same as the **p** rod (on the average) and may be accounted for by taking twice the product of Eq. 4.II.2 as in:

$$\boldsymbol{\sigma}_{\text{bend}} = -2\left(n\frac{\tilde{k}}{l_B}\int\int \mathbf{F}_p(l_B\mathbf{p})d\mathbf{p}d\mathbf{q} \right) \tag{4.II.3}$$

where n is the number of fibers per unit volume. Inserting Eq. 4.II.2 into Eq. 4.II.3 and after some simplification, we are left with two integrals to consider in Eq. 4.II.6.

$$\boldsymbol{\sigma}_{\text{bend}} = 2n\tilde{k}\int\int (\mathbf{I}-\mathbf{pp}).\,\mathbf{qp}d\mathbf{p}d\mathbf{q} \tag{4.II.4}$$

$$\boldsymbol{\sigma}_{\text{bend}} = 2n\tilde{k}\int\int (\,\mathbf{qp}-\mathbf{pp}.\,\mathbf{qp})d\mathbf{p}d\mathbf{q} \tag{4.II.5}$$

$$\boldsymbol{\sigma}_{\text{bend}} = 2n\tilde{k}\left(\int\int \mathbf{qp}d\mathbf{p}d\mathbf{q} - \int\int (\mathbf{pp}.\,\mathbf{qp})d\mathbf{p}d\mathbf{q}\right) \tag{4.II.6}$$

At this point, we recognize the first integral as the definition of **B**, but the second integral is unknown at this point. In general, this integral requires a closure approximation to be written in terms of **A** and **B**. Such an integral also shows up in the derivation of the Bead-Rod model, see Section 4.4.5 for a discussion, and will be handled in the manner suggested by Strautins and Latz (2007) by using a quadratic like closure for the mixed moments.

$$\int\int (\mathbf{pp}.\,\mathbf{qp})d\mathbf{p}d\mathbf{q} = \int\int (\mathbf{ppp}.\,\mathbf{q})d\mathbf{p}d\mathbf{q} \approx \int\int (\mathbf{pp})d\mathbf{p}d\mathbf{q}\int\int (\mathbf{p}.\,\mathbf{q})d\mathbf{p}d\mathbf{q} \tag{4.II.7}$$

After identifying the first integral as the definition of **A**, the second integral is found to be the $tr(\mathbf{B})$. Hence, the bending stress contribution becomes,

$$\boldsymbol{\sigma}_{\text{bend}} = 2n\tilde{k}\left(\mathbf{B}-\mathbf{A}tr(\mathbf{B})\right) \tag{4.II.8}$$

After inserting definitions for k (Eq. II.9), using the theory of Doi and Edwards (1988) to quantify n (Eq. 4.II.11), and algebraic simplification, we are then left with the stress equation presented in Eq. 4.21 (with $c_3 = 1$).

$$k = \frac{2\tilde{k}}{C_d l_B^{\,2}} \tag{4.II.9}$$

$$C_d = 3\pi\eta_m d \tag{4.II.10}$$

$$n = \frac{4\phi a_r^{\,4}}{\pi(2l_B)^3} \tag{4.II.11}$$

$$\boldsymbol{\sigma}_{\text{bend}} = \eta_m k\frac{3\phi a_r}{2}\left(\mathbf{B}-\mathbf{A}tr(\mathbf{B})\right) \tag{4.II.12}$$

Chapter 5

Predicting the Orientation of Long Glass Fibers in a Center-Gated Disk Using Model Parameters Determined From Simple Shear Rheology

Preface

This chapter assesses the performance of the Bead-Rod and Folgar-Tucker model, in their ability to predict fiber orientation in an injection molded center-gated disk, when using parameters determined from a rheological study using a sliding plate. This chapter is organized as a manuscript for publication.

Predicting the Orientation of Long Glass Fibers in a Center-Gated Disk Using Model Parameters Determined From Simple Shear Rheology

Kevin Ortman, Donald Baird
Chemical Engineering, Virginia Tech, Blacksburg, VA 24061

Peter Wapperom
Mathematics, Virginia Tech, Blacksburg, VA 24061

Alex Aning
Material Science and Engineering, Virginia Tech, Blacksburg, VA 24061

5.1 Abstract

The properties of long glass fiber reinforced parts, manufactured by means of injection molding, are highly dependent on the fiber orientation generated during mold filling. In this research, the orientation of long glass fibers generated during the filling of a center-gated mold geometry was simulated using a decoupled approach in which the velocity field was calculated for the matrix material. The orientation of the fibers was then calculated using a theory for short fibers, referred to as the Folgar-Tucker model, and a theory for semi-flexible fibers referred to as the Bead-Rod model. Model parameters used in the simulations were determined from independent rheological measurements using a sliding plate rheometer to generate the startup of simple shear flow. The predicted orientation of the fibers was compared with experimentally measured values obtained from center-gated injection molded parts. The Folgar-Tucker model provided slightly better orientation predictions up to 20% of the fill radius, but above 20% the Bead-Rod model predicted slightly better values of the orientation in the radial direction, A_{rr}, and orientation values in the circumferential direction, $A_{\theta\theta}$. The Folgar-Tucker model, however, provided better values of the orientation perpendicular to the flow direction, A_{zz}, over the center-gated disk. Additionally, it was found that both models only qualitatively represented the orientation above 60% of the fill radius (especially near the wall), and this was believed to be due to frontal flow effects not yet accounted for. It is expected that as the flexibility of the fibers increases, that the Bead-Rod model will provide better predictions of fiber orientation.

5.2 Introduction

The term "long fiber" is used in this context to describe fibers that are able to bend or flex during flow and thus during processing. This bending and flexing, therefore, could affect both the material's microstructure and properties. Subsequently, the term "flexibility" will be used to describe the fiber's ability to bend in the presence of flow. Specifically, a fiber exhibiting a larger degree of flexibility is easier to bend within a specified flow field. Switzer and Klingenberg (2003) quantified the effective stiffness (S^{eff}) of a fiber in a viscous medium by proposing a dimensionless group that contains both the viscosity of the matrix, the fiber aspect ratio ($a_r = L/d$, where L is the fiber length and d is the diameter) and the Young's modulus (E_Y) of the fiber [1]:

$$S^{eff} = \frac{E_Y \pi}{64 \eta_m \dot{\gamma} a_r^4} \tag{5.1}$$

In Eq. 5.1, η_m is the matrix viscosity and $\dot{\gamma}$ is the shear rate. From this expression, the stiffness of a fiber can be seen to decrease (increased flexibility) with aspect ratio for a given material (ie. fixed Young's modulus). Glass fibers less than 1 mm in length are sometimes considered to be "short" (and hence rigid) while fibers of length greater than 1 mm are considered to be "long" (and hence flexible), as suggested in a review from Crosby (1991) [2].

The conventional way of handling fiber orientation stems from short fiber theory wherein the orientation of a rigid fiber can be described as a vector that is parallel to the fiber, denoted in Fig. 5.1 as **p**. For a given orientation distribution function ψ, wherein ψ describes the probability of finding a fiber of specific orientation within a differential volume of space, the second moment of ψ may be evaluated in the following way to form an orientation tensor (**A**), Eq. 5.2.

$$\mathbf{A}(t) = \int \mathbf{pp}\psi(\mathbf{p},t)d\mathbf{p} \tag{5.2}$$

The orientation tensor provides a convenient means of describing the orientation of a population of fibers. For example, if the fibers are all oriented in the 1-direction (i.e. the flow direction), the orientation tensor will have an A_{11} component of 1.0, and 0 for all other components. Likewise, an initial 3-direction orientation would have an orientation tensor whose A_{33} component is 1.0, and 0 for all other components. Consequently, fibers randomly oriented in the 1-3 plane will have components $A_{11} = A_{33} = 0.5$, with 0 for all other components.

For short fiber suspension, the evolution of **A** in a flow is typically given by Jeffery's model with a modification by Folgar and Tucker (1984). In this model, Folgar and Tucker (1984) hypothesized, in non-dilute suspensions, that fiber interactions could be captured by an isotropic rotary diffusion term, as shown in Eq. 5.3, [3,4]:

$$\frac{D\mathbf{A}}{Dt} = \mathbf{W}\cdot\mathbf{A} - \mathbf{A}\cdot\mathbf{W} + \xi(\mathbf{D}\cdot\mathbf{A} + \mathbf{A}\cdot\mathbf{D} - 2\mathbf{D}:\mathbf{A}_4) + 2C_I\dot{\gamma}(\mathbf{I} - 3\mathbf{A}) \tag{5.3}$$

wherein $\mathbf{W} = [(\nabla \mathrm{v})^t - \nabla \mathrm{v}]/2$ is the vorticity tensor, $\mathbf{D} = [(\nabla \mathrm{v})^t + \nabla \mathrm{v}]/2$ is the rate of strain tensor, and ξ is a shape factor defined in terms of the particles aspect ratio as $\xi = (a_r^2 - 1)/(a_r^2 + 1)$. In this context, the velocity gradient is defined as $\nabla \mathrm{v} = \partial \mathrm{v_j}/\partial \mathrm{x_i}$. In Eq. 5.3, C_I is the isotropic rotary diffusion coefficient and **I** is the identity tensor, and $\dot{\gamma} = (2\mathbf{D}:\mathbf{D})^{1/2}$ is the scalar magnitude of **D**. Also, a fourth order orientation tensor exists in this model and is defined as the fourth moment of the orientation distribution function as given in Eq. 5.4.

$$\mathbf{A}_4(t) = \int \mathbf{pppp}\psi(\mathbf{p},t)d\mathbf{p} \tag{5.4}$$

$\mathbf{A_4}$ requires a closure approximation to decouple this fourth order tensor in terms of the second order orientation tensor **A**. Common forms of this closure approximation are

expressed through linear, quadratic, hybrid, and higher order polynomial closures such as the invariant-based optimal fitting (IBOF) approximation, as proposed by Chung and Kwon (2001) [5].

Much research has been conducted with Eq. 5.3, and has had success in describing the orientation of short fibers only qualitatively well, such as shown in the works of Bay (1992) [6,7]. In a later paper, Eq. 5.3 was modified to incorporate a method that allowed for the slowing of the orientation dynamics and was referred to as the reduced strain closure (RSC) model by Wang et al. (2008) [8]. A simpler effort has been attempted in the past by Huynh et al. (2001) by incorporating a slip coefficient (α) to be multiplied by the right hand side of Eq. 5.3 to form Eq. 5.5 [9].

$$\frac{D\mathbf{A}}{Dt} = \alpha\left(\mathbf{W}\cdot\mathbf{A} - \mathbf{A}\cdot\mathbf{W} + \xi(\mathbf{D}\cdot\mathbf{A} + \mathbf{A}\cdot\mathbf{D} - 2\mathbf{D}:\mathbf{A}_4) + 2C_I\dot{\gamma}(\mathbf{I} - 3\mathbf{A})\right) \tag{5.5}$$

In Eq. 5.5, α is a number between 0 and 1, and attempts to reduce the rate of fiber orientation. Adding the slip coefficient to the Folgar-Tucker equation results in a loss of material objectivity, but has been proven useful in predicting the orientation within Hele-Shaw flows, for example see Bay and Tucker (1992) and Wang et al. (2008), [6,7,8]. Additionally, an anisotropic rotary diffusion (ARD) form of the Folgar-Tucker equation exists, but will not be discussed in this research, and instead the reader is referred to the work of Phelps and Tucker (2009) [10].

Although short fiber theory has been useful in predicting fiber orientation, a better understanding of long glass fiber orientation might be obtained through a model that accounts for semi-flexible fibers. The first continuum model that accounts for the orientation evolution of semi-flexible fibers is one proposed by Strautins and Latz (2007) and is referred to here as the Bead-Rod model [11]. In this model, a semi-flexible fiber is modeled as two connected "rods" of orientation **p** and **q**, each of length l_B, that may flex about a central pivot point, as shown in Fig. 5.2. The semi-flexible fiber has a resistance to bending and is accounted for by a resistance potential that exists between both rods. When the fiber is perfectly straight no restorative force exists within the fiber. However, if the fiber is placed in a flow that may induce fiber curvature, the fiber bends in response to the drag flow on the "beads."

To model the orientation changes of such fibers, Strautins and Latz (2007) developed the kinematic equations for the bead and rod fiber in Fig. 5.2. This model has been modified from its original form to account for the isotropic rotary diffusion term suggested by Folgar and Tucker (1984) [3], and is referred to here as the Bead-Rod model. The model describes the evolution of 3 moments of the **p** and **q** vectors in the following manner,

$$\mathbf{A}(t) = \int\int \mathbf{pp}\ \psi(\mathbf{p},\mathbf{q},t)d\mathbf{p}d\mathbf{q} \tag{5.6}$$

$$\mathbf{B}(t) = \int\int \mathbf{pq}\ \psi(\mathbf{p},\mathbf{q},t)d\mathbf{p}d\mathbf{q} \tag{5.7}$$

$$\mathbf{C}(t) = \int\int \mathbf{p}\ \psi(\mathbf{p},\mathbf{q},t)d\mathbf{p}d\mathbf{q} \tag{5.8}$$

Eq. 5.6 is similar to what exists in rigid rod theory and describes the second moment of any one of the rods with respect to the orientation distribution function. Another orientation tensor describes the mixed product of both rod vectors with the orientation distribution function, Eq. 5.7. Lastly, the first moment of the distribution function, using either rod's orientation vector, Eq. 5.8 is also formed. The Bead-Rod model, originally for dilute suspensions, was extended to non-dilutes suspensions by Ortman et al. (2011) who considered the isotropic rotary diffusion term [12]. The modified model that describes how a given flow field affects the orientation functions is given in the following Eqs. 5.9-5.12.

$$\frac{D\mathbf{A}}{Dt} = \alpha\Big[\big(\mathbf{W}\cdot\mathbf{A}-\mathbf{A}\cdot\mathbf{W}\big)+\big(\mathbf{D}\cdot\mathbf{A}+\mathbf{A}\cdot\mathbf{D}-2\mathbf{D}:\mathbf{A}_4\big)-6C_I\,\dot{\gamma}\Big(\mathbf{A}-\frac{1}{3}\mathbf{I}\Big) \\ \ldots+\frac{l_B}{2}[\mathbf{Cm}+\mathbf{mC}-2(\mathbf{m}\cdot\mathbf{C})\mathbf{A}]-2k\big(\mathbf{B}-\mathbf{A}\ \mathrm{tr}(\mathbf{B})\big)\Big] \tag{5.9}$$

$$\frac{D\mathbf{B}}{Dt} = \alpha\Big[\big(\mathbf{W}\cdot\mathbf{B}-\mathbf{B}\cdot\mathbf{W}\big)+\big(\mathbf{D}\cdot\mathbf{B}+\mathbf{B}\cdot\mathbf{D}-(2\mathbf{D}:\mathbf{A})\mathbf{B}\big)-4C_I\,\dot{\gamma}\mathbf{B} \\ \ldots+\frac{l_B}{2}[\mathbf{Cm}+\mathbf{mC}-2(\mathbf{m}\cdot\mathbf{C})\mathbf{B}]-2k\big(\mathbf{A}-\mathbf{B}\ \mathrm{tr}(\mathbf{B})\big)\Big] \tag{5.10}$$

$$\frac{D\mathbf{C}}{Dt} = \alpha\Big[\nabla\boldsymbol{v}^t\cdot\mathbf{C}-(\mathbf{A}:\nabla\boldsymbol{v}^t)\mathbf{C}+\frac{l_B}{2}[\mathbf{m}-\mathbf{C}(\mathbf{m}\cdot\mathbf{C})]-k\,\mathbf{C}[1-\mathrm{tr}(\mathbf{B})]-2C_I\,\dot{\gamma}\mathbf{C}\Big] \tag{5.11}$$

$$\mathbf{m} = \sum_{i=1}^{3}\sum_{j=1}^{3}\sum_{k=1}^{3}\frac{\partial^2 v_{\mathrm{i}}}{\partial x_{\mathrm{j}}\partial x_{\mathrm{k}}}A_{\mathrm{jk}}\,\mathbf{e}_{\mathrm{i}} \tag{5.12}$$

Within these equations, *tr*() represents the trace of a specified tensor, k is the resistive bending potential coefficient Within Eq. 5.12, $\mathbf{m}$ is a vector formed by the summation over the indices ijk, and $\boldsymbol{e}_{\mathrm{i}}$ are the vector component dyads. Each term containing C_I in Eqs. 5.9-5.11 is the associated isotropic rotary diffusion term as it applies to the Bead-Rod model. Additionally, α has been added to each of the above equations, and retains the identical meaning as it does when used with the Folgar-Tucker model, Eq. 5.5. In this form of the Bead-Rod model, flexibility may be induced by a combination of rotary diffusion and by hydrodynamic effects.

In this research, we assess the performance of the Bead-Rod and Folgar-Tucker orientation models in their abilities to predict the orientation within an injection molded center-gated disk, when using parameters obtained from a previous rheological study using a sliding plate [12]. This is done to validate a previously proposed method in which modeling parameters are based on rheological data, using newly modified and augmented stress theory, and are independent from the process being simulated.

5.3 Experimental and Computational Methods

5.3.1 Materials and Preparation of CGD Parts

A center-gated disk mold with internal radius of 2.97 mm, outer radius of 52 mm, and thickness of 2.05 mm was used to create the injection molded samples, Fig 5.3. An injection molding machine (Arburg Allrounder, Model 221-55-250) was used to generate short shot parts for which each final part had a radius of 45 mm. This corresponds to approximately 90% fill of the total mold. Short shots were purposely generated to avoid frontal wall effects and packing. Long glass fiber reinforced polypropylene material was provided by SABIC Innovative Plastics and had an initial concentration of 30 wt.%, wherein the volume fraction of fibers (ϕ) ϕ = 0.145. The initial fiber length of 13 mm was reduced significantly during the extrusion process, and it was found via digital imaging that the materials had an average fiber length (L_N) of 3.22 mm. The average diameter of the fibers is d = 14.5 μm. As a note, the glass fiber system used in this research possessed a ϕ such that, using the theory of Doi and Edwards (1988), the suspension was classified as concentrated, $\phi \geq a_r^{-1}$ [13]. The resin was dried overnight at 80 ^{o}C, and was injection molded with an extruder homogenous temperature profile of 250 ^{o}C, except for the solids conveying zone which was controlled at 240 ^{o}C, and pressure of approximately 20 MPa. The mold temperature was held at 60 ^{o}C. Each part was made in approximately 2 s, corresponding to a volumetric flow rate of 6.52 cm^3/s. The part was cooled for 60 s before ejecting.

5.3.2 Simulation Approximations

The 2-dimensional (2-D) simulations conducted in this research were accomplished by uncoupling the orientation dynamics from the stress tensor, as has been done in the works of Bay and Tucker (1992), Wang et al (2008) and Phelps and Tucker (2009), and Velez et al. [6,7,8,10,14]. Furthermore, the Hele-Shaw approximation was used to obtain a velocity field for the case of an isothermal, incompressible Newtonian fluid. A non-isothermal consideration was not taken in this research due to the very short times that exist for conduction to take place between the melt and the mold walls, during the mold fill process, and because of the offset of this cooling with viscous dissipation. The viscous dissipation effect by itself is also not expected to increase the melt temperature significantly, and was estimated to be less than 1 ^{o}C. Using these approximations, the velocity field within the center-gated disk is written in Eq. 5.13, [15].

$$v_r = \frac{1}{r}\frac{3Q}{8\pi h}\left(1-\frac{z^2}{h^2}\right) \tag{5.13}$$

In Eq. 5.13, Q is the volumetric flow of the fluid, h is the half height of the center-gated disk thickness, and v_r and v_z represent the radial and gap-wise component velocities fields, respectively. Using the orientation models discussed above, provided initial conditions, the orientation of the fibers can be solved with Eq. 5.13.

Lastly, a closure relation was used to approximate the fourth order orientation tensor $\mathbf{A}_4$ in terms of the second order orientation tensor $\mathbf{A}$. In this research, we used the

5th degree polynomial IBOF closure approximation both in the Folgar-Tucker model and in the Bead-Rod model, Eq. 5.9. The reader is referred to work of Chung and Kwon (2001) for a description of the IBOF closure approximation. It will be stated, for completion, that during the derivation of the Bead-Rod model higher mixed moments of both **p** and **q** naturally arose in Eqs. 5.10-5.11. See the work of Strautins and Latz (2007) for a more detailed discussion. These moments too required closure, and Strautins and Latz (2007) listed criteria that should be met to provide such closures. In the end, a closure relationship similar to the quadratic closure, see for example Advani and Tucker (1990) [16], was used within Eqs. 5.10-5.11. We will follow their approach and use Eqs. 5.10-5.11 as written in this text.

5.3.3 Model Parameters

All model parameters used within this research were determined from a rheological study in which orientation and stress model parameters were selected to best fit the rheological response of the material, using a sliding plate rheometer. In this related research, the Bead-Rod model was coupled with an empirically modified form of the Lipscomb (1988) stress tensor that was also augmented to account for the semi-flexibility of the fibers [12,17]. This empirically modified form of the Lipscomb model (without the addition of the stress due to flexibility) was also used with the Folgar-Tucker model, and it was shown that the conventional form of the Lipscomb model was unable to accurately reproduce the transient stress response of the materials being studied. Orientation and stress model parameters were determined by best fitting these coupled orientation and stress equations to the measured stress data. This current work directly assesses the chosen method for determining model parameters and also compares the accuracy of an orientation model based on flexibility (Bead-Rod) versus one based on rigid fibers (Folgar-Tucker). The model parameters determined from the previous study are listed in Table 5.1 for reference.

5.3.4 Measurement of Fiber Orientations

Fiber orientation of the injection molded samples was measured using a micrographic technique proposed by Hine et al. (1996) [18]. Specifically, fibers were analyzed along the radial dimension of the flow. For each radial location, 3 independent samples were cut in the *r-z* plane, see Fig. 5.3, to inspect the intersecting fibers along the full thickness of each part. A polished sample length of 5.5 mm was imaged using an optical microscope along this full part thickness. The significance of this sampling dimension will be the subject of a future publication, however for the time being, it is important that the sampling dimension be larger than L_N. Therefore, each sample taken was 5.5 mm x 2.05 mm. A digital imaging program was written to analyze the cross-sectional ellipses to determine the values of the orientation tensor. This data was then separated into 12 "bins" along the thickness to provide a profile of the orientation throughout the thickness. Each bin corresponds to a dimension approximately equal to *d*, and is consistent with the approach used by Bay and Tucker et al. (1992) [6,7].

5.3.5 Initial Conditions

Fiber orientation at the gate (r = 2.97 mm) of the disk was experimentally measured, using the method described in Section 5.3.4, and was used as initial conditions for the orientation models. For the Bead-Rod Model, other initial conditions are needed for Eqs. 5.10-5.11. As of now, fiber curvature cannot be measured, so we have chosen to assume that the fibers are initially straight before each experiment, and hence, $\mathbf{B}(0) = -\mathbf{A}(0)$, and $\mathbf{C}(0) = \mathbf{0}$. The initial gate orientation, and its experimental variation, is displayed in Fig 5.4a.

5.3.6 Numerical Methods

A Mathematica code was written to solve the initial value system of equations. The measured gate orientation was interpolated to form a spanning function over the part thickness at the gate. An orientation profile of 31 points (2 points per experimentally analyzed bin) was simulated and interpolated along the thickness of the part to numerically represent the orientation at various radial positions. Changes in this orientation were calculated by integrating along the fluid streamlines using the velocity field (Eq. 5.13) in combination with the Bead-Rod and Folgar-Tucker orientation models.

5.4 Simulation Results and Discussion

Injection molded samples were simulated in 10% increments from the gate. At 10% of the fill radius, only small changes in the orientation profile were found, as compared to that measured at the gate, Fig. 5.4b. Both model solutions show very similar, but accurate, results. In fact, the only differences that exist between the two predictions occur at the wall, wherein the Folgar tucker model slightly captures the A_{rr} orientation values better at z/h = +/- 1. Also, the Folgar-Tucker model more accurately captures the A_{zz} component of the orientation tensor as compared to the Bead-Rod model, and is due to the quadratic nature of the closure approximations used in Eq. 5.10-5.11. Lastly, although not shown for brevity, the Bead-Rod predicts the largest degree of bending near the walls and corresponds to a 2% reduction in the end-to-end distance (degree of bending). This bending slightly reduces the A_{rr} component near the walls and slightly increases the A_{zz} component instead. This bending cannot be experimentally verified, however, it suggests that the glass fibers used in this research behave in a semi-flexible manner. Near 20% of the fill, a similar trend is seen, Fig 5.4c. The Folgar-Tucker model predicts slightly better $A_{\theta\theta}$ components, but in this case over predicts the orientation at both walls. Again, both models are very similar and do a good job at capturing the profile. The Folgar-Tucker model more accurately predicts the A_{zz} component.

At 30% and 40% of the fill, both models again accurately predict the orientation profile, Fig. 5.4d and Fig. 5.5a. The Folgar-Tucker model over predicts the orientation at the wall, but more accurately predicts the A_{zz} profile. The Bead-Rod model provides just a slightly more accurate description of the A_{rr} and $A_{\theta\theta}$ components. Again, (though not shown for brevity) the Bead-Rod model predicts the largest degree of bending near the

walls, but the magnitude of this bending is predicted to decrease with increased radial fill position.

Between 50% - 70% of the fill radius, the models do a good job capturing the core of the center gated disk (approximately between z/h = +/- 0.5) but begin to show notable deviations from experiment at the walls, Fig 5.5b-d. This is hypothesized to be due to a combination of thermal cooling of the flow and frontal flow effects that become more significant at higher radial positions. Neither of these effects is accounted for in our current simulation. In each case, the Folgar-Tucker model more accurately predicts the A_{zz} component.

Lastly, from 80%-100% of the sample fill, large deviation between the predictions and experimental values exist above z/h = +/- 0.5, Fig 5.6a-c. The core region is still captured relatively well, but the presence of the frontal flow is believed to now effect regions near the wall increasing in a manner that experimentally seems to be driving the orientation to a planar random state. Simulations of these suggested effects are expected to yield better performance near the disk front.

5.5 Conclusions

The purpose of this paper was to assess the performance of the Bead-Rod and Folgar-Tucker orientation models, when using parameters determined from a rheological study (for both models), by comparing the predicted orientations with experimentally measured values obtained from injection molded parts. Encouraging results were gained using both orientation models, using the method described in this research, up to about 60% of the filled disk radius. Specifically, the Folgar-Tucker provided noticeably better orientation predictions only up to 20% of the fill radius, but above 20% but the Bead-Rod model predicted slightly better A_{rr} and $A_{\theta\theta}$ orientation values. The Folgar-Tucker model, however, provided better A_{zz} predictions over the center-gated disk. Lastly, it was found that both models only qualitatively represented the orientation above 60% of the fill radius, and this was believed to be due to frontal flow effects not yet accounted for. Using rheologically consistent parameters, with the method proposed in a previous study, was shown to be a fundamental and useful method for predicting orientation. Studying the effects of frontal flow is still needed to better predict orientation. It is expected that as the flexibility of the fibers increases, that the Bead-Rod model will provide better predictions of fiber orientation.

5.6 Acknowledgments

The financial support for this work, from the National Science Foundation through Grant No. CMMI-0853537, is greatly appreciated. We would also like to thank SABIC for providing the materials used in this work. Additional gratitude is given to the Materials Science and Engineering department at Virginia Tech for providing polishing and microscopy facilities.

5.7 References

1. Switzer LH III, Klingenberg DJ. Rheology of sheared flexible fiber suspensions via fiber-level simulations. J. Rheol. 2003;47:759-778.

2. Crossby JM. Long-fiber molding materials. In: Carlson LA editor. Thermoplastic Composite Materials. Amsterdam: Elsevier, 1991, p. 139-168.
3. Jeffery GB. The motion of ellipsoidal particles immersed in a viscous fluid. Proc. R. Soc. A. 1992:102;161-179.
4. Folgar FP, Tucker III CL. Orientation behavior of fibers in concentrated suspensions. J. Reinf. Plast. Compos. 1984;3:98-119.
5. Chung DH, Kwon TH. Improved model of orthotropic closure approximation for flow induced fiber orientation. Polym. Compos. 2001;22:636-649.
6. Bay RS, Tucker III CL. Fiber orientation in simple injection moldings. Part I. Theory and numerical methods. Poly. Compos. 1992;13:317-331.
7. Bay RS, Tucker III C.L. Fiber orientation in simple injection moldings. Part II. Theory and numerical methods. Poly. Compos. 1992;13:332-341.
8. Wang J, O'Gara J, Tucker III CL. An objective model for slow orientation kinetics in concentrated fiber suspensions: Theory and rheological evidence. J. Rheol 2008;52:1179-1200.
9. Huynh HM. Improved fiber orientation predictions for injection-molded composites. Master's Thesis. University of Illinois at Urbana-Champaign, 2001.
10. Phelps J, Tucker III CL. An anisotropic rotary diffusion model for fiber orientation in short- and long-fiber thermoplastics. J. Non-Newtonian Fluid Mech. 2009;156 :165-176.
11. Strautins U, Latz A. Flow-driven orientation dynamics of semiflexible fiber systems. Rheol. Acta. 2007;46:1057-1064.
12. Ortman KC. Assessing an Orientation Model and Stress Tensor for Semi-Flexible Glass Fibers in Polypropylene Using a Sliding Plate Rheometer: for the Use of Simulating Processes. Ph.D. Thesis. Virginia Tech Polytechnic Institute and State University, 2011.
13. Doi M, Edwards SF. The Theory of Polymer Dynamics. Oxford University Press. New York. 1988.
14. Velez-Garcia GM, Mazahir SM, Wapperom P, Baird DG. Simulation of Injection Molding Using a Model with Delayed Fiber Orientation. Intern. Polym Proc. 26;3:331-339.
15. Baird DG, Collias D. Polymer Processing: Principles and Design. New York: John Wiley & Sons, 1995.
16. Advani SG, Tucker III CL. Closure approximations for three-dimensional structure tensors. J. Rheology 1990;34:367-386.
17. Lipscomb GG, Denn MM, Hur DU, Boger DV. The flow of fiber suspensions in complex geometries. J. Non-Newtonian Fluid Mech. 1988;26:297-325.
18. Hine PJ, Davidson N, Duckett RA, Clarke AR, Ward IM. Hydrostatically extruded glass–fiber reinforced polyoxymethylene. I. The development of fiber and matrix orientation. Polym. Compos. 1996;17:720–729.

30 wt.%	Folgar-Tucker	Bead-Rod
C_I	5.0×10^{-3}	5.3×10^{-2}
α	0.25	0.13
c_1	15	24
b	1.0	0.65
c_2	5.2×10^{5}	1.4×10^{5}

Table 5.1: Model parameters determined obtained from rheological fits.

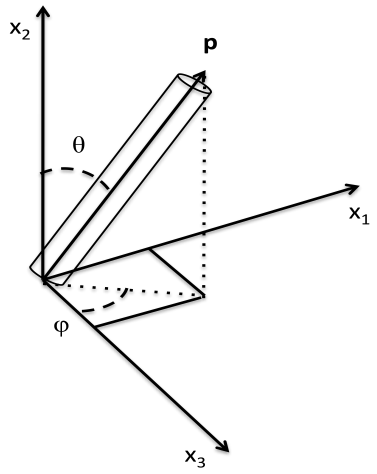

Figure 5.1: Rigid fiber with orientation vector **p**.

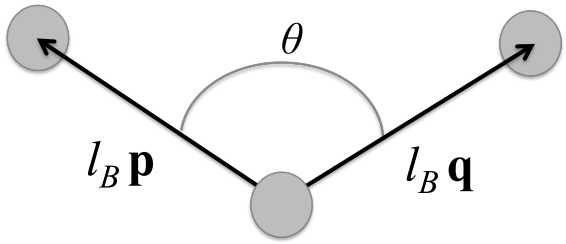

Figure 5.2: Semi-flexible (bead and rod) fiber model of Strautins and Latz (2007). Fiber is constructed by two connected orientation vectors **p** and **q**.

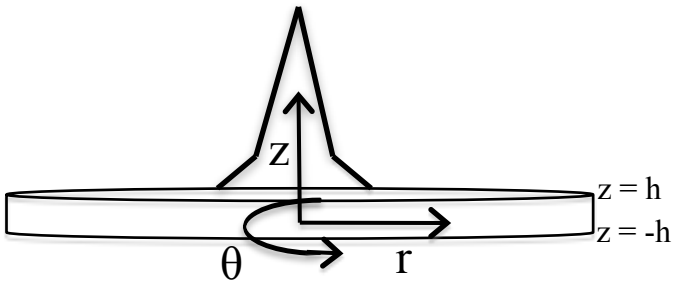

Figure 5.3: Center-gated disk and coordinate system.

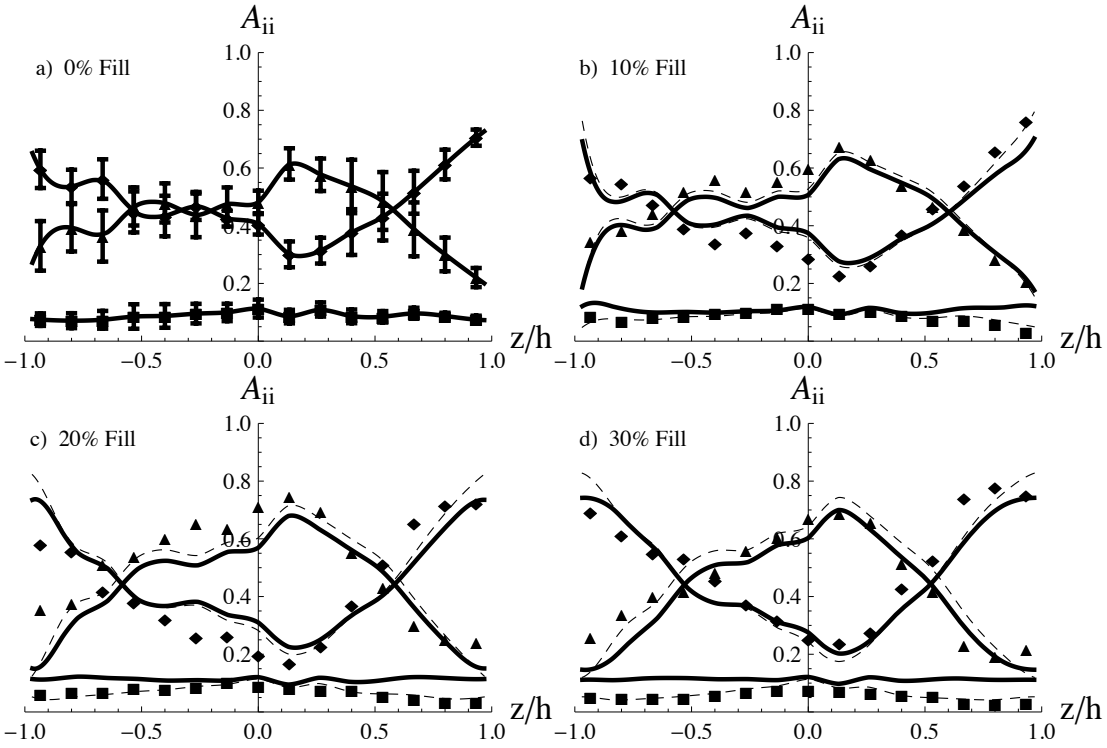

Figure 5.4: Comparison of orientation vs. part thickness of the Bead-Rod (solid) and Folgar-Tucker (dashed) models with experimental data A_{rr} (♦), A_{zz} (■), and $A_{\theta\theta}$ (▲) components at various radial fill positions (a) 0%, (b) 10%, (c) 20%, (d) 30%. Error bars denote the standard deviation.

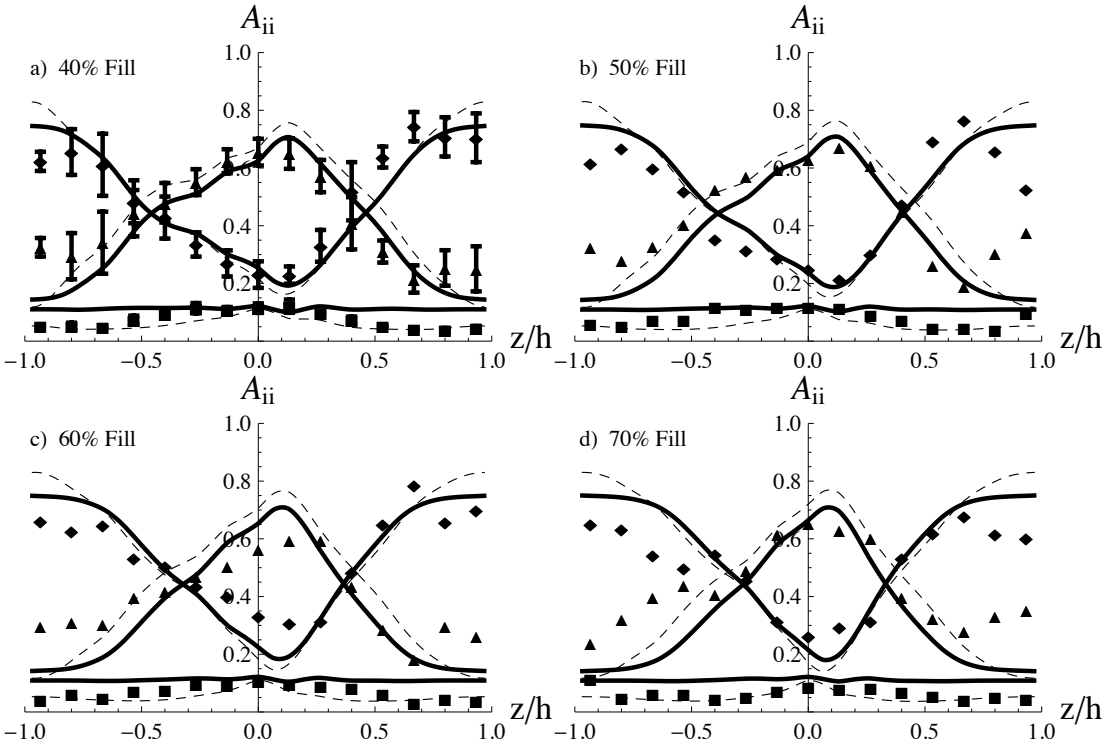

Figure 5.5: Comparison of orientation vs. part thickness of the Bead-Rod (solid) and Folgar-Tucker (dashed) models with experimental data A_{rr} (♦), A_{zz} (■), and $A_{\theta\theta}$ (▲) components at various radial fill positions (a) 40%, (b) 50%, (c) 60%, (d) 70%. Error bars denote the standard deviation.

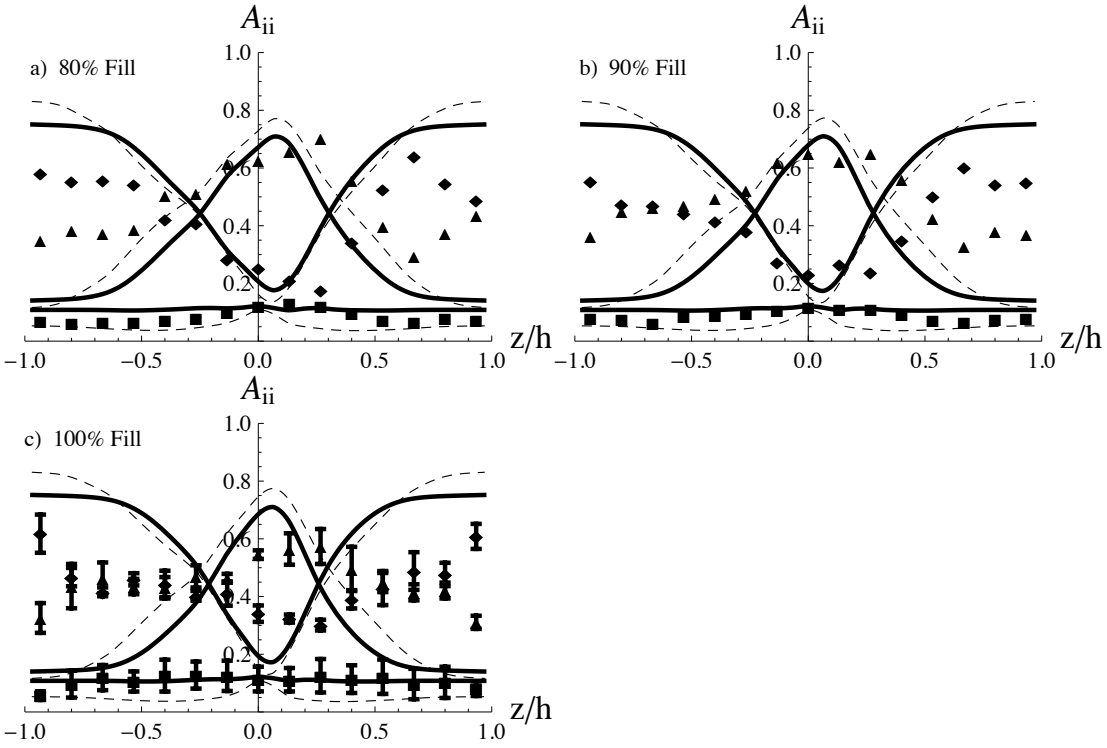

Figure 5.6: Comparison of orientation vs. part thickness of the Bead-Rod (solid) and Folgar-Tucker (dashed) models with experimental data A_{rr} (♦), A_{zz} (■), and $A_{\theta\theta}$ (▲) components at various radial fill positions (a) 80%, (b) 90%, (c) 100%. Error bars denote the standard deviation.

Chapter 6

Conclusions and Recommendations for Future Work

Chapter 6 Conclusions and Recommendation for Future Work

6.1 Conclusions from this Research

Within this research, a sliding plate rheometer was shown to be a viable means of obtaining the transient viscosity at the startup of shear flow for concentrated short and long glass fiber suspensions. Additionally, the sliding plate rheometer was shown to confirm the short glass fiber results obtained by Eberle et al. (2009), who suggested that the inhomogeneous shear field generated in a conventional parallel disk rheometer may lead to enhanced stress transients, both in terms of the magnitude of the overshoot and the time to reach steady state. Using the sliding plate rheometer, the transient rheology at the startup of shear flow was measured for concentrated long glass fiber suspensions with different initial orientations. These experiments showed that initial fiber orientation and concentration greatly affected the rheological behavior.

Using data obtained from sliding plate experiments, an orientation model and stress tensor combination, designed to provide a first approximation for flexible fiber systems, was assessed and compared to the more conventional orientation model, called the Folgar-Tucker model, which is based on rigid fiber theory. To accomplish this, we extended the semi-flexible orientation model, called the Bead-Rod model, to non-dilute suspensions by including isotropic rotary diffusion and also derived an appropriate stress tensor term (based on this model) that accounts for the semi-flexibility of the fibers, for the purpose of obtaining model parameters from stress growth data. In this work we showed the conventional Lipscomb (1988) stress tensor, when coupled with the Folgar-Tucker model, was unable to fit the transient stress data, and instead we have proposed empirical modifications to the Lipscomb model that more accurately fits this data. Specifically, in this research we explored empirical modifications to fiber stress theory that utilize functional weights instead of the more classical method of using constant weights. Rheological fits showed the Bead-Rod model and proposed stress theory, overall, provided a more accurate description of the stress response of the long glass fiber systems explored (as compared to the Folgar-Tucker model), but still has room for improvement. Additionally, stresses due to fiber flexibility were predicted to account for small but non-negligible bending stresses.

A method for determining model parameters, based on the rheology of fiber systems, was demonstrated using the proposed and modified stress theory created within this research. Using these model parameters, orientation predictions were compared to experimentally measured values within a simple shear flow. Both the Folgar-Tucker model and Bead-Rod models produced encouraging orientation predictions in almost all cases. The Bead-Rod model and associated stress tensor, overall, produced better A_{11} orientation component predictions. The Folgar-Tucker model, however, produced better orientation results for the A_{33} and A_{22} in almost all of the cases studied. Experimentally, the transient fiber orientation was seen to be predominately a function of strain, and only varied slightly with shear rate. More flexible fiber systems will be studied in the future, and it is believed that with increased flexibility the Bead-Rod model (and associated stress tensor) will be of increased value.

Lastly, we assessed the performance of the Bead-Rod and Folgar-Tucker orientation models for the case of an injection molded center-gated disk, when using the parameters determined from our rheological study (for both models), by comparing the

predicted orientations with experimentally measured values obtained from injection molded parts. Encouraging results were gained using both orientation models, using the method described in this research, up to about 60% of the filled disk radius. Specifically, the Folgar-Tucker provided noticeably better orientation predictions only up to 20% of the fill radius, but above 20% but the Bead-Rod model predicted slightly better A_{rr} and $A_{\theta\theta}$ orientation values. The Folgar-Tucker model, however, provided better A_{zz} predictions over the center-gated disk. Lastly, it was found that both models only qualitatively represented the orientation above 60% of the fill radius, and this was believed to be due to frontal flow effects not yet accounted for. Using rheologically consistent parameters, with the method proposed within this research, was shown to be a fundamental and useful method for predicting orientation. Studying the effects of frontal flow is still needed to better predict orientation. It is expected that as the flexibility of the fibers increases, that the Bead-Rod model will provide better predictions of fiber orientation.

6.2 Rheological Recommendations

The sliding plate rheometer has demonstrated itself to be a useful tool in both measuring the transient stress of long fibers and exploring the transient orientation, in a simple shear flow. The limitations of the sliding plate, however, restrict the length of fiber that may be measured before wall interactions become significant. Therefore, in order to gain a more meaningful understanding of the effect of flexibility, both on its rheological response and on its transient orientation, fibers of various diameter and/or moduli should be explored. To elaborate, fiber flexibility is known to be very sensitive to aspect ratio (as high as a 4^{th} order dependence, see for example Eq. 3.1) and can be a useful parameter in understanding the effects of flexibility, but one is limited in the fiber length that can be used due to wall effects in the rheometer. Hence, fibers with various diameters may be explored without increasing wall effects. The modulus of a fiber material also affects the degree of flexibility (linear dependence on flexibility), and hence different materials (with different moduli) may also be explored.

Additionally, it would be very beneficial to measure normal stress differences created by the suspension. Specifically, the first normal stress difference function provides yet another perspective into the understanding of the suspension stress response and its associated transient fiber orientation. The current set-up of our sliding plate does not measure such stresses. However, it may be possible to mount another transducer close in proximity to the presently existing shear stress transducer in order to obtained such measurements. Additionally, it would be very beneficial to explore higher shear rates. This work was mechanically restricted to an order of magnitude range in shear rate, but future work should consider an experimental set-up that exceeds this limitation.

Flow reversal is another simple shear experiment that is often of interest with fiber suspensions. In this test, a sample is sheared in one direction and then, after some amount of deformation, is sheared in the opposite direction. Such experiments have been conducted on concentrated short fiber systems (ie. Eberle et al.), and have been known to yield interesting behaviors such as delayed stress growth and normal stress difference undershoots. Such experiments can be conducted in the sliding plate, but in order to gain the most information from these experiments a normal stress transducer should be

installed to see if long/flexible fiber systems behave similarly. Such experiments may be of future benefit.

Like simple shear flow, extensional flow is another fundamental flow field that should be explored. In this work, all rheological data and model parameters came from simple shear rheology, but it is of equal importance to understand these characteristics from perspective of a rheometric extensional flow. Another way of stating this is, it is recommended that one determine if the model parameters gained from simple shear flow are consistent with those obtainable with an extensional flow. If so, the manner in which we are conducting our current complex flow simulations, wherein one set of model parameters is used over the entire flow field, is correct. However, if a more consistent set of parameters is found from extensional rheology, one may have to account for the parameter dependence on flow in a complex molding geometry (where both shear and extension may exist). As a note, it is plausible that the parameters (in our current explored materials) will not be very different, as compared to those determined from simple shear, and evidence of this can be realized by noticing the orientation predictions for the injection molded center-gated disks, obtained within this research, performed quite well in the core region of the disk (high extension) while using the simple shear model parameters. Regardless, this should be verified. The easiest way to begin studying the extensional effects on long fiber suspensions is to study biaxial extension, or squeeze rheology. This method avoids the problem of necking in fiber composite elongational experiments. The caveat, however, is one must obtain well lubricated walls to avoid shear.

6.3 Model Recommendations

It was shown in this research that orientation models such as the Bead-Rod model (for non-dilute suspension) and the Folgar-Tucker model were capable of predicting the transient orientation of long fibers in simple shear flow. The stress tensors developed and used in this research, however, have much room for improvement. This is most likely due to complex fiber-fiber interactions, in concentrated suspensions, which are not well understood. This research showed that, when using concentrated long glass fiber suspensions, conventional stress theory was incapable of fitting the rheological data measured. Modifications and adaptations to conventional stress theory were proposed and used in this research. These modifications resulted in much better performance, but improvement is still needed. For example, when parameters were determined using initially planar random fibers, good fits were obtained but, in general, failed to accurately predict the rheological response of the same suspensions with different initial fiber orientations. A stress term that realistically represents fiber-fiber interactions is highly desired and recommended to provide a confident link between the rheological response and the evolution of fiber orientation and configuration.

The fiber materials studied in this research were found to be only semi-flexible, but for the purpose of exploring more flexible systems, an appropriate orientation model will be needed. It is believed that the Bead-Rod model will be of future use in exploring such flexible materials, but in the case where fibers become extremely flexible, a more robust model may be needed. If such a model does become desired, a more flexible Bead-Rod orientation model may be derived by considering more connecting beads and

rods. However, one must keep in mind that as the number of beads and rods increases, so does the number of equations that must be solved.

6.4 Simulation Recommendations

Encouraging orientation predictions, for an injection molded center-gated disk, were obtained within this research when using a stress-decoupled, Hele-Shaw, isothermal simulation. It was seen, however, that the orientation predictions began to fail near the wall regions of the disk at increased radial position. This is believed to suggest, that studying the frontal flow effects are very important in accurately predicting orientation throughout the whole part, especially at increased distance from the gate. Currently, we do not consider the presence of frontal flow.

Additionally, a stress-coupled simulation should be explored, as opposed the stress-decouple simulations performed in this research. It was shown in this research, that the stress response of a fiber suspension can be very sensitive to the fiber orientation. Therefore, a coupled simulation that provides consistency between the equations of change, stress tensor, and orientation equations may yield better orientation prediction accuracy. However, this type of simulation is not necessarily recommended until a better understanding of the stress tensor is first developed.

Appendix A: Rheological Data

CODE: SB-wt%-Initial Direction-Shear Rate
(ex. SB-30wt%-Random-1.0s^{-1} = SB30%DXSR1p0)

Transient Sliding Plate Rheology Data:

SB30%D1SR0p4		SB30%D1SR1p0		SB30%D1SR4p0	
Strain	Visc. (Pa s)	Strain	Visc. (Pa s)	Strain	Visc. (Pa s)
0	0	0	0	0	0
2	1040	2	3410	2	2330
4	1140	4	3830	4	2960
6	1210	6	4170	6	3010
8	1260	8	4350	8	3040
10	1280	10	4500	10	3060
12	1300	12	4640	12	3060
14	1320	14	4780	14	3030
16	1320	16	4890	16	2990
18	1320	18	4980	18	2940
20	1320	20	5060	20	2880
22	1300	22	5160	22	2820
24	1280	24	5240	24	2730
26	1260	26	5310	26	2640
28	1260	28	5370	28	2550
30	1240	30	5420	30	2450
32	1230	32	5450	32	2370
34	1220	34	5480	34	2330
36	1220	36	5470	36	2310
38	1220	38	5450	38	2260
40	1220	40	5340	40	2190
42	1220	42	5220	42	2120
44	1220	44	5080	44	2040
46	1220	46	4920	46	1930
48	1220	48	4700	48	1820
50	1220	50	4520	50	1710
52	1220	52	4320	52	1590
54	1220	54	4220	54	1460
56	1220	56	4060	56	1320
58	1220	58	3890	58	1180
60	1220	60	3710	60	1050
62	1220	62	3580	62	908
64	1220	64	3530	64	771
66	1220	66	3530	66	656
68	1220	68	3530	68	591
70	1220	70	3510	70	578
72	1220	72	3500	72	578
74	1220	74	3490	74	578
76	1220	76	3470	76	578
78	1220	78	3430	78	578
80	1220	80	3360	80	578

82	1220	82	3270	82	578
84	1220	84	3150	84	578
86	1220	86	3020	86	578
88	1220	88	2910	88	578
90	1220	90	2840	90	578
92	1220	92	2750	92	578
94	1220	94	2650	94	578
96	1220	96	2560	96	578
98	1220	98	2490	98	578
100	1220	100	2380	100	578
102	1220	102	2230	102	578
104	1220	104	2070	104	578
106	1220	106	1860	106	578
108	1220	108	1660	108	578
110	1220	110	1490	110	578
112	1220	112	1400	112	578
114	1220	114	1370	114	578
116	1220	116	1360	116	578
118	1220	118	1360	118	578
120	1220	120	1360	120	578

SB10%D1SR0p4		SB10%D1SR1p0		SB10%D1SR4p0	
Strain	Visc. (Pa s)	Strain	Visc. (Pa s)	Strain	Visc. (Pa s)
0	0	0	0	0	0
2	1160	2	947	2	873
4	1210	4	1110	4	930
6	1240	6	1180	6	921
8	1260	8	1230	8	896
10	1270	10	1250	10	870
12	1280	12	1250	12	841
14	1290	14	1250	14	809
16	1290	16	1230	16	781
18	1300	18	1210	18	760
20	1300	20	1190	20	734
22	1310	22	1170	22	711
24	1310	24	1150	24	689
26	1310	26	1130	26	674
28	1310	28	1100	28	660
30	1310	30	1080	30	646
32	1310	32	1070	32	629
34	1310	34	1050	34	608
36	1310	36	1020	36	596
38	1310	38	1000	38	583
40	1310	40	985	40	576
42	1310	42	970	42	568
44	1310	44	960	44	562
46	1310	46	953	46	562
48	1310	48	944	48	559
50	1310	50	941	50	558
52	1310	52	938	52	558

54	1320	54	935	54	558
56	1320	56	936	56	558
58	1320	58	934	58	558
60	1310	60	934	60	557
62	1310	62	929	62	558
64	1310	64	927	64	556
66	1320	66	925	66	557
68	1310	68	924	68	558
70	1310	70	921	70	554
72	1310	72	917	72	554
74	1310	74	916	74	554
76	1310	76	916	76	554
78	1300	78	914	78	555
80	1300	80	909	80	556
82	1290	82	908	82	557
84	1280	84	904	84	556
86	1280	86	899	86	553
88	1280	88	894	88	553
90	1270	90	893	90	551
92	1270	92	890	92	549
94	1270	94	885	94	550
96	1270	96	885	96	549
98	1270	98	887	98	549
100	1270	100	890	100	546
102	1270	102	888	102	546
104	1260	104	888	104	546
106	1260	106	885	106	543
108	1260	108	882	108	543
110	1260	110	881	110	544
112	1260	112	880	112	543
114	1260	114	879	114	541
116	1270	116	877	116	542
118	1270	118	877	118	542
120	1260	120	877	120	547

SB30%D3SR0p4		SB30%D3SR1p0		SB30%D3SR4p0	
Strain	Visc. (Pa s)	Strain	Visc. (Pa s)	Strain	
0	0	0	0	0	0
2	2850	2	2710	2	2230
4	4180	4	3430	4	2890
6	5360	6	4010	6	3300
8	6100	8	4400	8	3600
10	6760	10	4730	10	3800
12	7120	12	5030	12	3930
14	7350	14	5220	14	3990
16	7500	16	5360	16	3990
18	7530	18	5480	18	3960
20	7600	20	5610	20	3970
22	7650	22	5740	22	3950
24	7650	24	5830	24	3900

26	7650	26	5910	26	3870
28	7650	28	5970	28	3840
30	7650	30	5990	30	3790
32	7650	32	6000	32	3680
34	7670	34	6000	34	3560
36	7700	36	5960	36	3460
38	7700	38	5830	38	3360
40	7700	40	5710	40	3270
42	7700	42	5620	42	3160
44	7700	44	5530	44	3040
46	7700	46	5450	46	2990
48	7700	48	5410	48	2970
50	7700	50	5370	50	2930
52	7700	52	5310	52	2900
54	7700	54	5260	54	2890
56	7700	56	5180	56	2890
58	7700	58	5130	58	2890
60	7700	60	5090	60	2890
62	7700	62	5030	62	2890
64	7700	64	4980	64	2890
66	7700	66	4930	66	2890
68	7700	68	4850	68	2890
70	7700	70	4740	70	2890
72	7680	72	4690	72	2890
74	7650	74	4670	74	2890
76	7590	76	4660	76	2890
78	7520	78	4650	78	2890
80	7500	80	4640	80	2890
82	7480	82	4630	82	2890
84	7460	84	4600	84	2890
86	7460	86	4590	86	2890
88	7460	88	4550	88	2890
90	7460	90	4530	90	2890
92	7460	92	4510	92	2890
94	7460	94	4480	94	2890
96	7460	96	4450	96	2890
98	7460	98	4440	98	2890
100	7460	100	4430	100	2890
102	7460	102	4430	102	2840
104	7460	104	4420	104	2790
106	7460	106	4400	106	2750
108	7460	108	4370	108	2690
110	7460	110	4360	110	2610
112	7460	112	4350	112	2540
114	7460	114	4320	114	2450
116	7460	116	4300	116	2300
118	7460	118	4280	118	2060
120	7460	120	4270	120	1730
SB10%D3SR0p4		SB10%D3SR1p0		SB10%D3SR4p0	

Strain	Visc. (Pa s)	Strain	Visc. (Pa s)	Strain	
0	0	0	0	0	0
2	1160	2	491	2	615
4	1210	4	594	4	682
6	1240	6	632	6	714
8	1260	8	688	8	739
10	1270	10	723	10	761
12	1280	12	769	12	781
14	1290	14	797	14	799
16	1290	16	817	16	816
18	1300	18	827	18	832
20	1300	20	836	20	844
22	1310	22	845	22	852
24	1310	24	854	24	858
26	1310	26	861	26	860
28	1310	28	863	28	860
30	1310	30	866	30	854
32	1310	32	871	32	849
34	1310	34	876	34	841
36	1310	36	879	36	831
38	1310	38	881	38	825
40	1310	40	888	40	822
42	1310	42	890	42	818
44	1310	44	892	44	812
46	1310	46	891	46	807
48	1310	48	889	48	801
50	1310	50	883	50	794
52	1310	52	876	52	787
54	1320	54	868	54	783
56	1320	56	858	56	779
58	1320	58	848	58	773
60	1310	60	843	60	769
62	1310	62	840	62	762
64	1310	64	837	64	757
66	1320	66	833	66	752
68	1310	68	831	68	745
70	1310	70	831	70	739
72	1310	72	828	72	728
74	1310	74	824	74	720
76	1310	76	822	76	718
78	1300	78	819	78	713
80	1300	80	817	80	707
82	1290	82	813	82	699
84	1280	84	810	84	695
86	1280	86	807	86	688
88	1280	88	802	88	681
90	1270	90	795	90	671
92	1270	92	788	92	661
94	1270	94	781	94	652

96	1270	96	773	96	642
98	1270	98	763	98	631
100	1270	100	753	100	621
102	1270	102	745	102	611
104	1260	104	738	104	602
106	1260	106	731	106	591
108	1260	108	725	108	580
110	1260	110	721	110	576
112	1260	112	721	112	573
114	1260	114	718	114	572
116	1270	116	714	116	572
118	1270	118	712	118	570
120	1260	120	711	120	570
SB30%DXSR0p4		SB30%DXSR1p0		SB30%DXSR4p0	
Strain	Visc. (Pa s)	Strain	Visc. (Pa s)	Strain	Visc. (Pa s)
0	0	0	0	0	0
2	4370	2	3230	2	2100
4	5330	4	3950	4	2730
6	5840	6	4700	6	2960
8	6520	8	5080	8	3130
10	7140	10	5350	10	3290
12	7280	12	5470	12	3400
14	7420	14	5540	14	3480
16	7490	16	5580	16	3550
18	7520	18	5560	18	3590
20	7530	20	5540	20	3620
22	7530	22	5440	22	3630
24	7510	24	5330	24	3650
26	7430	26	5200	26	3640
28	7350	28	5070	28	3620
30	7250	30	4950	30	3590
32	7130	32	4820	32	3560
34	6990	34	4670	34	3530
36	6840	36	4460	36	3480
38	6710	38	4190	38	3430
40	6570	40	3930	40	3360
42	6400	42	3680	42	3300
44	6240	44	3540	44	3250
46	6110	46	3490	46	3200
48	6000	48	3470	48	3140
50	5920	50	3460	50	3070
52	5850	52	3460	52	3010
54	5760	54	3470	54	2920
56	5670	56	3470	56	2840
58	5590	58	3470	58	2780
60	5520	60	3470	60	2700
62	5480	62	3470	62	2620
64	5420	64	3460	64	2570
66	5370	66	3460	66	2500

68	5330	68	3460	68	2460
70	5290	70	3450	70	2400
72	5280	72	3450	72	2350
74	5260	74	3460	74	2290
76	5240	76	3460	76	2230
78	5230	78	3460	78	2200
80	5230	80	3470	80	2180
82	5210	82	3470	82	2160
84	5220	84	3490	84	2150
86	5230	86	3480	86	2160
88	5230	88	3470	88	2150
90	5220	90	3460	90	2150
92	5210	92	3460	92	2160
94	5200	94	3470	94	2160
96	5180	96	3460	96	2160
98	5170	98	3460	98	2170
100	5190	100	3460	100	2170
102	5190	102	3460	102	2140
104	5160	104	3450	104	2100
106	5140	106	3460	106	2060
108	5140	108	3450	108	2000
110	5120	110	3470	110	1900
112	5120	112	3480	112	1810
114	5110	114	3480	114	1720
116	5100	116	3470	116	1600
118	5100	118	3470	118	1530
120	5100	120	3470	120	1490

SB30%DXSR0p4		SB30%DXSR1p0		SB30%DXSR4p0	
Strain	Visc. (Pa s)	Strain	Visc. (Pa s)	Strain	Visc. (Pa s)
0	0	0	0	0	0
2	896	2	1100	2	814
4	1420	4	1170	4	866
6	1490	6	1220	6	891
8	1510	8	1250	8	909
10	1520	10	1250	10	904
12	1520	12	1230	12	886
14	1500	14	1200	14	862
16	1480	16	1180	16	842
18	1430	18	1110	18	817
20	1360	20	987	20	794
22	1300	22	904	22	777
24	1220	24	856	24	763
26	1190	26	814	26	749
28	1180	28	790	28	738
30	1170	30	782	30	737
32	1170	32	776	32	736
34	1170	34	768	34	736
36	1160	36	761	36	736
38	1160	38	764	38	734

40	1160	40	768	40	736
42	1160	42	759	42	739
44	1170	44	750	44	738
46	1160	46	749	46	738
48	1160	48	757	48	737
50	1160	50	765	50	736
52	1160	52	765	52	737
54	1160	54	765	54	737
56	1160	56	765	56	736
58	1160	58	772	58	738
60	1160	60	776	60	736
62	1160	62	772	62	736
64	1160	64	767	64	735
66	1160	66	757	66	733
68	1160	68	752	68	732
70	1160	70	753	70	732
72	1160	72	752	72	732
74	1150	74	752	74	733
76	1150	76	748	76	733
78	1160	78	746	78	732
80	1160	80	749	80	731
82	1160	82	752	82	728
84	1160	84	749	84	724
86	1160	86	747	86	722
88	1150	88	747	88	721
90	1150	90	750	90	719
92	1150	92	757	92	718
94	1150	94	756	94	718
96	1150	96	751	96	717
98	1150	98	754	98	717
100	1150	100	752	100	711
102	1150	102	748	102	701
104	1150	104	745	104	687
106	1150	106	743	106	675
108	1150	108	745	108	663
110	1150	110	748	110	651
112	1150	112	749	112	640
114	1150	114	746	114	633
116	1150	116	744	116	621
118	1150	118	745	118	614
120	1150	120	745	120	607

Appendix B: Sliding Plate Orientation Data

CODE: SB-wt%-Initial Direction-Shear Rate
(ex. SB-30wt%-Random-1.0s^{-1} = SB30%DXSR1p0)

Transient Orientation Data

SB30%DXSR0p4

Strain	A11	A12	A22	A33
0	0.5649	0.0481	0.0377	0.3974
10	0.5944	0.0488	0.0381	0.3674
20	0.6240	0.0495	0.0386	0.3375
30	0.6522	0.0494	0.0345	0.3134
40	0.6284	0.0557	0.0399	0.3318
50	0.7221	0.0529	0.0421	0.2358
60	0.7461	0.0521	0.0443	0.2096
70	0.7628	0.0521	0.0430	0.1944
80	0.7685	0.0472	0.0395	0.1921
90	0.7637	0.0378	0.0293	0.2070
100	0.8158	0.0345	0.0307	0.1536
110	0.7887	0.0369	0.0348	0.1765
120	0.7632	0.0301	0.1110	0.1257

SB30%DXSR1p0

Strain	A11	A12	A22	A33
0	0.5649	0.0481	0.0377	0.3974
10	0.6291	0.0486	0.0428	0.3281
20	0.6326	0.0601	0.0561	0.3113
30	0.6587	0.0576	0.0550	0.2863
40	0.6958	0.0818	0.0902	0.2140
50	0.7035	0.0717	0.0756	0.2209
60	0.7412	0.0678	0.0697	0.1891
70	0.7051	0.0742	0.0818	0.2131
80	0.7223	0.0648	0.0634	0.2143
90	0.7223	0.0593	0.0634	0.2143
100	0.7210	0.0669	0.0689	0.2101
110	0.7239	0.0640	0.0685	0.2076
120	0.7833	0.0610	0.0592	0.1575

SB30%DXSR4p0

Strain	A11	A12	A22	A33
0	0.5649	0.0481	0.0377	0.3974
10	0.5380	0.0401	0.0288	0.4332
20	0.5711	0.0320	0.0199	0.4091
30	0.6892	0.0292	0.0193	0.2916
40	0.7583	0.0248	0.0189	0.2229
50	0.7303	0.0284	0.0248	0.2449
60	0.7406	0.0251	0.0206	0.2389
70	0.7802	0.0226	0.0154	0.2044
80	0.7807	0.0237	0.0184	0.2009
90	0.7890	0.0243	0.0182	0.1928
100	0.7749	0.0226	0.0147	0.2104

110	0.7425	0.0303	0.0250	0.2326
120	0.7332	0.0226	0.0552	0.2116

SB10%DXSR0p4

Strain	A11	A12	A22	A33
0	0.5649	0.0481	0.0377	0.3974
10	0.5873	0.0475	0.0339	0.3787
20	0.6099	0.0470	0.0302	0.3600
30	0.6776	0.0372	0.0212	0.3012
40	0.7313	0.0377	0.0286	0.2401
50	0.7478	0.0326	0.0226	0.2297
60	0.7544	0.0305	0.0231	0.2226
70	0.7910	0.0258	0.0216	0.1873
80	0.7542	0.0238	0.0173	0.2286
90	0.8080	0.0230	0.0212	0.1708
100	0.8138	0.0189	0.0130	0.1732
110	0.7997	0.0214	0.0160	0.1844
120	0.7598	0.0199	0.0432	0.1970

SB10%DXSR1p0

Strain	A11	A12	A22	A33
0	0.5649	0.0481	0.0377	0.3974
10	0.6549	0.0382	0.0259	0.3192
20	0.6674	0.0329	0.0238	0.3088
30	0.7635	0.0280	0.0232	0.2133
40	0.7424	0.0304	0.0218	0.2358
50	0.7812	0.0435	0.0359	0.1829
60	0.7742	0.0359	0.0285	0.1973
70	0.7912	0.0193	0.0817	0.1271
80	0.8057	0.0273	0.0241	0.1702
90	0.7860	0.0285	0.0229	0.1911
100	0.7660	0.0326	0.0297	0.2043
110	0.8387	0.0272	0.0247	0.1366
120	0.7790	0.0385	0.0349	0.1861

SB10%DXSR4p0

Strain	A11	A12	A22	A33
0	0.5649	0.0481	0.0377	0.3974
10	0.6437	0.0394	0.0295	0.3269
20	0.6582	0.0423	0.0313	0.3207
30	0.5810	0.0405	0.0255	0.3935
40	0.6078	0.0396	0.0252	0.3671
50	0.6934	0.0425	0.0316	0.2750
60	0.6956	0.0368	0.0301	0.2744
70	0.7214	0.0528	0.0423	0.2364
80	0.7786	0.0421	0.0348	0.1866
90	0.7756	0.0309	0.0248	0.1996
100	0.7908	0.0317	0.0244	0.1849
110	0.7830	0.0399	0.0330	0.1841
120	0.7827	0.0434	0.0398	0.1776

SB30%D3SR1p0

Strain	A11	A12	A22	A33

0	0.0928	0.0645	0.0797	0.8275
20	0.3529	0.0400	0.0261	0.6209
40	0.5507	0.0358	0.0231	0.4261
60	0.6264	0.0367	0.0271	0.3465
80	0.6833	0.0468	0.0394	0.2773
120	0.7671	0.0326	0.0289	0.2040

SB10%D3SR1p0

Strain	A11	A12	A22	A33
0	0.0928	0.0645	0.0797	0.8275
20	0.3833	0.0352	0.0216	0.5951
40	0.5403	0.0262	0.0145	0.4452
60	0.6813	0.0247	0.0163	0.3024
80	0.6864	0.0289	0.0245	0.2892
120	0.8079	0.0285	0.0247	0.1673

SB30%D1SR1p0

Strain	A11	A12	A22	A33
0	0.8628	0.0254	0.0430	0.0943
10	0.8049	0.0317	0.0218	0.1732
20	0.8301	0.0319	0.0306	0.1393
40	0.8273	0.0391	0.0412	0.1315
120	0.8053	0.0762	0.0825	0.1121

SB10%D1SR1p0

Strain	A11	A12	A22	A33
0	0.8628	0.0254	0.0430	0.0943
10	0.8074	0.0335	0.0293	0.1633
20	0.8444	0.0304	0.0250	0.1307
40	0.8145	0.0237	0.0194	0.1660
120	0.8053	0.0762	0.0825	0.1121

Appendix C: Injection Molding (Center-Gated Disk) Orientation Data

Center Gate Disk Orientation Data

0% Fill				
yaxis	A11	A12	A22	A33
-0.9333	0.5953	0.0002	0.0746	0.3301
-0.8000	0.5361	0.0039	0.0710	0.3929
-0.6667	0.5617	0.0329	0.0740	0.3642
-0.5333	0.4478	0.0265	0.0854	0.4668
-0.4000	0.4336	0.0343	0.0874	0.4790
-0.2667	0.4686	0.0437	0.0954	0.4360
-0.1333	0.4247	0.0531	0.0994	0.4759
0.0000	0.4063	0.0693	0.1128	0.4809
0.1333	0.3008	0.0066	0.0851	0.6141
0.2667	0.3137	-0.0082	0.1098	0.5765
0.4000	0.3780	-0.0549	0.0859	0.5361
0.5333	0.4299	-0.0511	0.0844	0.4857
0.6667	0.5159	-0.0572	0.0966	0.3874
0.8000	0.6121	-0.0671	0.0874	0.3005
0.9333	0.7051	-0.0560	0.0746	0.2204
10% Fill				
yaxis	A11	A12	A22	A33
-0.9333	0.5678	-0.0012	0.0866	0.3456
-0.8000	0.5465	0.0130	0.0683	0.3852
-0.6667	0.4739	0.0161	0.0835	0.4426
-0.5333	0.3924	0.0282	0.0873	0.5203
-0.4000	0.3408	0.0279	0.0969	0.5623
-0.2667	0.3771	0.0606	0.1019	0.5210
-0.1333	0.3307	0.0506	0.1139	0.5554
0.0000	0.2865	0.0344	0.1141	0.5994
0.1333	0.2292	-0.0197	0.0961	0.6748
0.2667	0.2648	-0.0314	0.1036	0.6316
0.4000	0.3689	-0.0596	0.0896	0.5416
0.5333	0.4607	-0.0456	0.0734	0.4659
0.6667	0.5395	-0.0360	0.0718	0.3887
0.8000	0.6580	-0.0429	0.0587	0.2833
0.9333	0.7623	-0.0151	0.0311	0.2066
20% Fill				
yaxis	A11	A12	A22	A33
-0.9333	0.5802	0.0006	0.0624	0.3574
-0.8000	0.5558	-0.0233	0.0675	0.3767
-0.6667	0.4176	-0.0048	0.0695	0.5130
-0.5333	0.3797	0.0120	0.0807	0.5396
-0.4000	0.3217	0.0124	0.0779	0.6004
-0.2667	0.2606	0.0185	0.0860	0.6534
-0.1333	0.2612	0.0198	0.1032	0.6356
0.0000	0.1982	-0.0059	0.0906	0.7112
0.1333	0.1699	-0.0367	0.0835	0.7466

0.2667	0.2295	-0.0581	0.0765	0.6940
0.4000	0.3708	-0.0628	0.0750	0.5542
0.5333	0.5105	-0.0370	0.0559	0.4336
0.6667	0.6550	-0.0062	0.0452	0.2998
0.8000	0.7150	0.0009	0.0340	0.2510
0.9333	0.7240	0.0203	0.0341	0.2419

30% Fill

yaxis	A11	A12	A22	A33
-0.9333	0.6917	0.0112	0.0506	0.2577
-0.8000	0.6135	-0.0079	0.0462	0.3404
-0.6667	0.5495	0.0139	0.0491	0.4014
-0.5333	0.5318	0.0121	0.0487	0.4195
-0.4000	0.4568	0.0243	0.0582	0.4850
-0.2667	0.3718	0.0212	0.0669	0.5613
-0.1333	0.3189	0.0450	0.0742	0.6070
0.0000	0.2517	0.0101	0.0764	0.6719
0.1333	0.2386	-0.0070	0.0727	0.6888
0.2667	0.2776	-0.0284	0.0659	0.6565
0.4000	0.4272	-0.0216	0.0572	0.5156
0.5333	0.5275	-0.0142	0.0548	0.4176
0.6667	0.7404	-0.0056	0.0291	0.2305
0.8000	0.7800	0.0002	0.0259	0.1941
0.9333	0.7526	0.0167	0.0311	0.2163

40% Fill

yaxis	A11	A12	A22	A33
-0.9333	0.6230	0.0197	0.0517	0.3253
-0.8000	0.6554	-0.0037	0.0501	0.2945
-0.6667	0.6111	0.0127	0.0477	0.3411
-0.5333	0.4831	0.0319	0.0735	0.4434
-0.4000	0.4283	0.0337	0.0922	0.4796
-0.2667	0.3348	0.0177	0.1141	0.5511
-0.1333	0.2694	0.0298	0.1070	0.6236
0.0000	0.2306	0.0295	0.1144	0.6550
0.1333	0.2288	0.0213	0.1212	0.6500
0.2667	0.3303	0.0122	0.0977	0.5721
0.4000	0.5194	-0.0040	0.0722	0.4085
0.5333	0.6381	-0.0074	0.0514	0.3105
0.6667	0.7433	-0.0146	0.0414	0.2154
0.8000	0.7080	-0.0133	0.0384	0.2537
0.9333	0.7048	-0.0184	0.0446	0.2506

50% Fill

yaxis	A11	A12	A22	A33
-0.9333	0.6163	-0.0066	0.0577	0.3260
-0.8000	0.6677	-0.0086	0.0514	0.2809
-0.6667	0.5975	0.0233	0.0723	0.3302
-0.5333	0.5202	0.0103	0.0742	0.4056
-0.4000	0.3532	0.0395	0.1192	0.5276
-0.2667	0.3162	0.0240	0.1115	0.5723
-0.1333	0.2861	0.0268	0.1185	0.5954

0.0000	0.2490	0.0334	0.1191	0.6318
0.1333	0.2136	0.0122	0.1147	0.6718
0.2667	0.3026	0.0353	0.0886	0.6088
0.4000	0.4755	0.0243	0.0740	0.4505
0.5333	0.6926	0.0238	0.0438	0.2636
0.6667	0.7651	0.0092	0.0433	0.1915
0.8000	0.6580	0.0217	0.0362	0.3058
0.9333	0.5250	0.0041	0.0983	0.3767

60% Fill

yaxis	A11	A12	A22	A33
-0.9333	0.6622	0.0107	0.0401	0.2976
-0.8000	0.6276	0.0001	0.0619	0.3105
-0.6667	0.6464	0.0048	0.0488	0.3049
-0.5333	0.5322	0.0090	0.0705	0.3973
-0.4000	0.5037	0.0228	0.0768	0.4196
-0.2667	0.4365	0.0370	0.0944	0.4691
-0.1333	0.4023	0.0362	0.0931	0.5046
0.0000	0.3309	0.0519	0.1061	0.5629
0.1333	0.3064	0.0376	0.0971	0.5964
0.2667	0.3151	0.0352	0.0909	0.5941
0.4000	0.4825	0.0351	0.0816	0.4359
0.5333	0.6518	0.0211	0.0605	0.2878
0.6667	0.7866	0.0189	0.0313	0.1821
0.8000	0.6559	0.0297	0.0456	0.2984
0.9333	0.7002	0.0223	0.0371	0.2626

70% Fill

yaxis	A11	A12	A22	A33
-0.9333	0.6508	-0.0395	0.1126	0.2366
-0.8000	0.6336	0.0197	0.0465	0.3200
-0.6667	0.5425	0.0084	0.0600	0.3976
-0.5333	0.4975	0.0318	0.0630	0.4395
-0.4000	0.5456	0.0402	0.0449	0.4095
-0.2667	0.4568	0.0520	0.0512	0.4920
-0.1333	0.3134	0.0530	0.0716	0.6150
0.0000	0.2615	0.0452	0.0849	0.6536
0.1333	0.2928	0.0312	0.0781	0.6291
0.2667	0.3136	0.0090	0.0827	0.6038
0.4000	0.5316	-0.0140	0.0700	0.3984
0.5333	0.6199	-0.0090	0.0556	0.3245
0.6667	0.6779	-0.0241	0.0421	0.2800
0.8000	0.6163	0.0132	0.0519	0.3318
0.9333	0.6026	0.0271	0.0452	0.3522

80% Fill

yaxis	A11	A12	A22	A33
-0.9333	0.5808	0.0048	0.0686	0.3506
-0.8000	0.5542	0.0063	0.0617	0.3841
-0.6667	0.5583	0.0059	0.0671	0.3746
-0.5333	0.5448	0.0204	0.0662	0.3890
-0.4000	0.4210	0.0386	0.0735	0.5054

-0.2667	0.4090	0.0641	0.0778	0.5132
-0.1333	0.2823	0.0556	0.1011	0.6166
0.0000	0.2522	0.0599	0.1224	0.6253
0.1333	0.2118	0.0405	0.1313	0.6569
0.2667	0.1764	0.0190	0.1194	0.7042
0.4000	0.3433	0.0051	0.0979	0.5589
0.5333	0.5266	-0.0146	0.0735	0.3999
0.6667	0.6400	0.0003	0.0651	0.2949
0.8000	0.5470	0.0101	0.0777	0.3752
0.9333	0.4888	0.0194	0.0734	0.4378
90% Fill				
yaxis	A11	A12	A22	A33
-0.9333	0.5539	-0.0037	0.0808	0.3653
-0.8000	0.4736	0.0171	0.0746	0.4517
-0.6667	0.4722	0.0200	0.0630	0.4648
-0.5333	0.4420	0.0194	0.0854	0.4726
-0.4000	0.4157	0.0309	0.0890	0.4953
-0.2667	0.3794	0.0560	0.0966	0.5240
-0.1333	0.2745	0.0343	0.1065	0.6190
0.0000	0.2306	0.0262	0.1190	0.6504
0.1333	0.2660	0.0039	0.1121	0.6219
0.2667	0.2376	-0.0229	0.1114	0.6511
0.4000	0.3481	-0.0403	0.0922	0.5597
0.5333	0.5008	-0.0244	0.0717	0.4274
0.6667	0.6037	-0.0205	0.0665	0.3298
0.8000	0.5441	-0.0198	0.0764	0.3795
0.9333	0.5504	-0.0125	0.0781	0.3716
100% Fill				
yaxis	A11	A12	A22	A33
-0.9333	0.6178	0.0086	0.0565	0.3257
-0.8000	0.4673	0.0481	0.0965	0.4362
-0.6667	0.4163	0.0290	0.1190	0.4647
-0.5333	0.4598	0.0012	0.1056	0.4346
-0.4000	0.4413	-0.0006	0.1259	0.4328
-0.2667	0.4024	0.0363	0.1278	0.4698
-0.1333	0.4104	0.0060	0.1252	0.4644
0.0000	0.3407	-0.0147	0.1141	0.5452
0.1333	0.3236	-0.0186	0.1117	0.5647
0.2667	0.3010	-0.0388	0.1255	0.5735
0.4000	0.3905	-0.0492	0.1139	0.4957
0.5333	0.4294	-0.0873	0.1221	0.4486
0.6667	0.4884	-0.0520	0.0969	0.4147
0.8000	0.4765	-0.0121	0.1026	0.4208
0.9333	0.6084	0.0167	0.0809	0.3107